Residual Stress Analysis within Structures using Incremental hole Drilling

Taha Negem

Technical University of Delft

TU Delft

Residual Stress Analysis within Structures using Incremental hole Drilling

by

Taha Negem

Master Thesis Report
at the Aerospace Structures & Materials Department (TUDelft)

Student number: 1551760
Research duration: July, 2017 – September, 2018
TUDelft supervisor: Ir. Jos Sinke

This report is confidential and cannot be made public.

TU Delft

Abstract

Various technological advances in this era have been been profound, as the current market requires the constant advancement of applications and services; in particular in the material science and technology sector. The main driving force for these advancements is the requirement to make lighter materials without sacrificing the structural integrity and safety. This is needed to cut down on operational costs and increase profits. Lighter materials were found in the use of composite structures since the constituents are lighter, have tailored properties, better fatigue and corrosion resistance. But new materials mean new challenges arise that are required to be studied, among them is the issue of creating residual stresses in the structure. These stresses could result in detrimental consequences during the part's service life.

Residual stresses are built-up stresses within structures or materials in the absence of external forces or thermal gradients. Measuring residual stresses is performed through various methods, classified upon their working principle and the level of damage introduced to the structure. Non-destructive methods which imply that no damage is induced to the structure at all, destructive methods which induce high damage to the structure rendering it unusable anymore thus unrepairable parts, in addition, semi-destructive methods induces minimal damage to the part that is repaired afterwards. The working principle of interest is based on removal of material that results in the deformation of the surrounding material. Monitoring these micro deformations and using stress-strain relations is done to determine the residual stresses. Hole drilling, a semi-destructive method was used to measure the residual stresses within Fiber Metal Laminates (FMLs); in particular GLARE.

The theory and experimental procedure of hole-drilling are described in detail in a standardized test (E837) by the American Society of Testing and Materials (ASTM). Using ASTM- E837 standard, a mathematical code was built in ANSYS to simulate GLARE laminates with residual stresses introduced to numerically obtain a relation between the induced stresses and relieved strains. The code includes the structure, orientation, mechanical and micro-thermal properties of the constituents. A matrix of coefficients is found relating the strains to stresses. These matrices are used in conjugation with experimental strains released from drilling the GLARE laminates in steps, leading to the computation of residual stresses. Verification and validation of the simulation models and the final results is performed.

Results verification of the numerical simulation show a close agreement with theoretical papers such as ASTM E837 for isotropic laminates and past research made by Schajer G. and L. Yang for orthotropic laminates. The maximum error found was 7 % for the coefficients found in both cases. Afterwards, the model was upgraded to be capable of measuring the coefficients for FMLs specially GLARE. This upgrade takes into consideration the fact that bending forces are created due to drilling in steps and the orthotropic nature of the GLARE laminates. Using the coefficients matrices found from this model, residual stresses are computed then verified with theoretical results computed using Classical Laminate Theory. Unfortunately the comparison between the theoretical and experimental results show an irregular and high error rate. The reason behind this error was concluded to be due to that the approach of using incremental hole drilling to measure residual stress within orthotropic laminates is not valid. Since, the method is built on the basis of applying stress upon the hole boundaries which is not feasible for orthotropic materials due to the complexity of relating the orthotropic strain response around a hole to the far field applied stresses. In addition, the relieved strains were measured using strain gauges at the surface, therefore, the deeper the measurement location, the lower the sensitivity of the gauges. In conclusion, incremental hole drilling requires more time and research to be applicable for measurement of residual stresses within advanced materials such as FMLs.

Taha Negem
Delft, September 2018

Acknowledgments

This thesis has developed out of the effort of many researchers and support staff, at Aerospace Structures and Materials department at the technical university of Aerospace Engineering in Delft. The research objective was to establish and describe a method for measuring residual stresses within structures post manufacturing at any given time or place.

Foremost, I would like to express my sincere gratitude to my thesis supervisor ir. Jos Sinke, for the opportunity to work on this project in order to develop my skills both personally and professionally. With his valuable experience he provided me guidance and monitored me during the project to gain better understanding of the manufacturing mechanics and tools. In addition, I would deeply thank Dr. Morteza Abouhamzeh for the continuous feedback and support throughout the project, whom insights paved the way for the content of this project.

I would also like to thank the staff at the laboratory DASML; In particular, Johan Boender, Cees Paalvast, Misja Huizinga and ing. Berthil Grashof for the support and help for computing the experimental work of my thesis. In addition, my earnest thanks for the researchers at the department of Manufacturing and Materials Engineering at Coventry University, United Kingdom: specifically Dr. Niall Smyth for providing data required to finalize this thesis.

Finally, this project would not have been possible without the vast support and love of my wife and family, I would like to thank them for the encouragement, devotion and continuous backing to follow my dreams and ambitions.

Contents

List of Figures

List of Tables

List of Acronyms

ESPI	Electronic Speckle Pattern Interferometry
HD	Hole Drilling
IHD	Incremental Hole Drilling
DHD	Deep Hole Drilling
NDT	Non-Destructive Testing
CLT	Classical Laminate theory
GLARE	GLass Fibre Reinforced Aluminum Laminates
CNC	Computer Numerically Controlled
DIC	Digital Image Correlation
LC	Long Cycle
SC	Short Cycle
SEB	Stress applied at Edge Boundary
SHB	Stress applied at Hole Boundary
CTE	Coefficient of Thermal Expansion
ASTM	American Society for Testing and Materials
FEM	Finite Element Model
FEA	Finite Element Analysis
MBN	Magnetic Brakhausen Noise
CMM	Coordinate Measuring Machine
EDM	Electric Discharge Machine
FML	Fiber Metal Laminate
ANSYS	Analysis System
APDL	ANSYS Parametric Design Language
HAZ	Heat Affected Zone
PRISM	Panchromatic Remote-Sensing Instrument for Stereo Mapping

List of Symbols

α	Thermal expansion coefficient of the plies in the material directions.
α_P	Regularization factor for P stresses.
α_Q	Regularization factor for Q stresses.
α_T	Regularization factor for T stresses.
γ_i	Shear strains in the i^{ith} direction
δ	In-plane displacement
$\delta\ T$	The temperature difference between the consolidation and service environment
ϵ	Released strain for uniform stress approach
ϵ_i	Normal strains in the i^{ith} direction
ϵ_j	Released strain after hole step J is drilled
θ	Angle between the reference strain gauge and material x-axis
ν	Poisson's ratio
ν_{ij}	Poisson's ratio
σ_{peak}	Peak stresses
σ_{nom}	Nominal stresses
σ_i	Normal stresses applied in the i^{ith} direction
σ_{max}	Maximum principle stress
σ_{min}	Minimum principle stress
σ_x	Uniform normal stress in x-direction
$(\sigma_x)_j$	Normal stress in x-direction within drill step J
σ_y	Uniform normal stress in y-direction
$(\sigma_y)_j$	Normal stress in y-direction within drill step J
τ_i	Shear stresses applied in the i^{ith} direction
τ_{xy}	Uniform shear stress in x-y direction
$(\tau_{xy})_j$	X-Y shear stress within drill step J
ω	Phase map provided using the different intensities of several imaging
$\bar{a}$	Calibration constant for isotropic stresses
$\bar{a}_{ij}$	Calibration matrix for isotropic stresses
A	Material dependent calibration constant for isotropic stresses
A_{ij}	Extensional stiffness matrix with (i & j) indices representing the standard material directions
B_{ij}	Coupling stiffness matrix with (i & j) indices representing the standard material directions
B	Material dependent calibration constant for shear stresses
$\bar{b}$	Calibration constant for shear stresses
$\bar{b}_{ij}$	Calibration matrix for shear stresses
C_{ij}	Elastic modulus that represent the stress-strain relation in general form
c_{ij}	Calibration matrix for orthotropic materials with (i) index for hole depth & (j) index for the stress depth level
D	Diameter of the gauge circle
D_{ij}	Bending stiffness matrix with (i & j) indices representing the standard material directions
D_0	Diameter of the drilled hole

E	Young's modulus
G_{ij}	Shear modulus with (i & j) material directions
h	Hole Depth
I	Pixel Intensities measured using the PRISM equipment
i	Number of hole depth up to this point
j	Stress level for hole depth drill steps
K_t	Stress intensity factor
M	Moment resultants applied to the laminate
N	Normal resultants applied to the laminate
n	Number of plies in a Laminate.
P	Uniform isotropic stress
P	Pressure applied inside the autoclave
P_j	Isotropic stress within drill step J
p	Uniform isotropic strain
p_j	Isotropic strain after drill step J
Q	Uniform 45° shear stress
Q_j	45° shear stress within drill step J
q	Uniform 45° shear strain
q_j	45° shear strain within drill step J
Q_{ij}	Stiffness matrix presenting the stress-strain relation with (i & j) indices representing the material directions
T	Consolidation Temperature of the autoclave
T	Uniform x-y shear stress
T_j	X-Y shear stress within drill step J
t	Uniform x-y shear strain
t	Thickness of the plies
t_j	X-Y shear strain within drill step J
V	Vacuum pressure
W	Width of a finite plate
z	Distance from midplane to any given point within the laminate structure

1 Introduction

In this chapter, residual stresses in structures, their effect, and the significance of their measurement in various sectors are discussed, and a brief description of practical measurement methods in measuring residual stresses is provided. The chapter concludes with an overview of the thesis strategy and structure.

1.1. Residual Stresses in Structures

Residual stresses are built up stresses within structures or materials in the absence of external forces or thermal gradients. Residual stresses are classified based on their effective scale, such as macro and micro scale stresses. Macro size stresses occur at a large scale, on the scale of a component size, and are also known as body stresses [17]. Stresses that occur at a grain scale, or within a grain by dislocations or deficiencies in a crystal are known as micro-scale stresses as well as textural stresses [3].

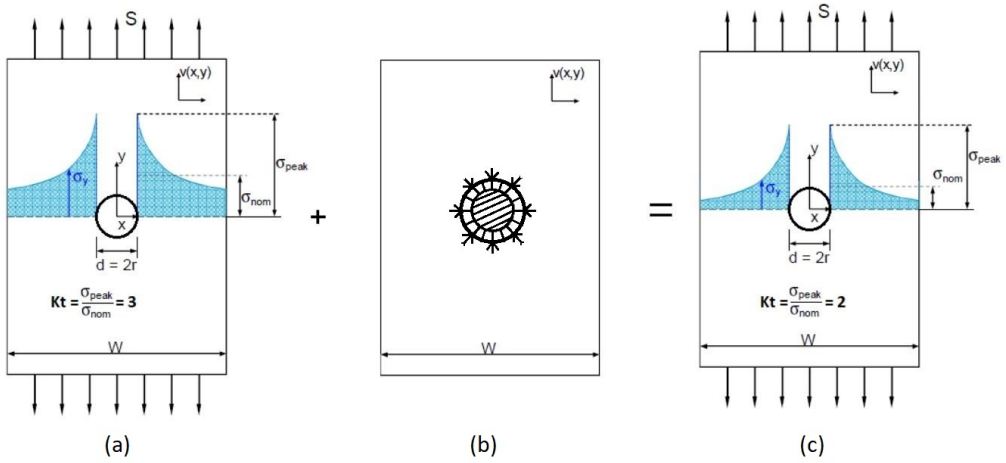

Figure 1.1: Stress intensity factor K_t before and after introducing compressive stresses.

In the current era of commercial aerospace industry, safety and comfort have become the driving catalysts behind modern innovations. Aviation safety implies that the risks associated with aeronautical activities or indirect actions that impacts the aircraft operation are assessed and minimized to an acceptable level. Most technology sectors apply similar requirements, with a few changes in the perspective of safety assessment. In this respect, determining residual stresses prior to a product service life has become a necessity to improve the overall efficiency of a functioning system. In the absence of external loads, the stress state within the material are in an equilibrium, consequently, inaccurate estimations regarding the magnitude of residual stresses prior to service life could have detrimental consequences for the product life span by amplifying the exerted force magnitude, causing earlier failures than expected. In contrast, proper evaluation of the component's inner stress state could

result in favorable conditions that prolong the life cycle of the component as presented in Figure 1.1. Where, case (*a*) illustrates the stress concentrations at a hole in an infinite plate under uni-axial loading. Introducing compressive stresses in case (*b*) around the hole that act in the opposite direction of the external force exerted on the component mitigates the effective magnitude of the force applied and lowers the stress concentrations at the hole, as illustrated in case (*c*). Thus, prolonging the life cycle of the component.

Figure 1.2: The Aloha flight 243 damage after an explosive decompression and structural failure during cruise flight [14].

In past years in the aerospace field, safety factors were implemented to minimize detrimental effects of unknown variables, which included residual stresses. This approach sometimes resulted in over-designing of the structure, which is not a problem but is inefficient. In addition, the likelihood of series of events that lead to disastrous outcomes was sometimes underestimated due to the lack of maintenance reassessment and overreliance on the safety factor, which was insufficient in some cases. Examples of such cases are:

1. The Aloha aircraft (1.2) that crashed in 1988, leading to the loss of a flight attendant and injury of 65 passengers, where negligence during aircraft maintenance and premature fatigue cracking were the main causes of the accident [12].

2. The Silver Bridge (1.3), which collapsed in 1967, leading to 46 fatalities due to stress corrosion cracking, magnified and accelerated by the existence of residual stresses from manufacturing [5].

3. The loss of a nuclear power plant due to stress corrosion cracking of steam generator tubes within the reactor [10].

Figure 1.3: The Silver Bridge, which collapsed due to stress corrosion and engineering shortcomings [13].

In addition to safety, the high waste of produced components due to early replacements relates to one of the driving forces of the industry: costs and expenses of users. The practices of disregarding healthy components, increasing maintenance inspections, and replacing primary structures directly impact customers' traveling costs.

Airliners profit margins are also dramatically affected, which is reflected in their ability to provide a satisfactory flight experience for their customers. For example, due to the current economic status, airliners are decreasing the available seat pitch for each passenger to increase the amount of passengers on-board of an aircraft, thus boosting their profit margin.

In the modern era of technology, innovative new designs and materials are presented daily, arising from the need for high strength, lightweight, and economical products. The implementation of new materials in the aerospace industry creates new challenges that need to be addressed in order to ensure their safe and economical use. These new designs and products are first applied in secondary or tertiary loaded structures to minimize risks, and are monitored continuously for their performance. The experiences and data obtained result in a more efficient design for further adequate application.

A new product undergoes a series of tests to determine its actual limitations, leading to a final design that satisfies the essential requirements in quality and functionality. Although, the essential requirements are fulfilled, little attention is given to determine the residual stresses prior to the launch. Therefore, the main objective of this thesis is to provide a simple approach to properly determine residual stress at any given time or location after manufacturing, with special consideration to glass reinforced laminates (GLARE), using incremental hole drilling (IHD). However, incremental hole drilling is just one of many methods available to measure residual stresses within materials, it is the only method standardized by the American Society for Testing and Materials (ASTM) [4]. This method is relatively simple to perform, provides reliable results, and introduces minimal damage to the specimen, hence its classification as a semi-destructive method. In the following section, an overview of the various methods for residual stress measurement is described, in addition, the justification for the choice of using IHD is presented.

1.2. Overview of Stress Measurement Techniques

In the past century, many techniques were developed in order to measure the residual stresses within structures. Each method has its own limitations regarding material and physical properties. Fortunately, due to the advancement of computing power and capabilities, the accuracy, reliability, and accessibility of calculation models have improved. This improvement is a direct result of the capability of numerical models to process massive amounts of data without the need for any simplifications. The measurement techniques are divided into three categories, based on the amount of damage introduced to the specimen: destructive, semi-destructive, and nondestructive methods. Destructive and semi-destructive techniques are based on the strategy of relieving the stress in the component by cutting or removing material resulting in relaxation of the part. The relaxation of the material is apparent in small deformations, which are measured using either conventional equipment, such as strain gauges, or advanced optical methods, such as Digital Image Correlation (DIC) and Electronic Speckle Pattern Interferometry (ESPI). Multiple calculation models are available to relate the measured strain response to residual stresses. These stress release methods are also known as mechanical methods.

In contrast, nondestructive techniques do not introduce any damage to the specimen and are based upon the monitoring of a physical property related to stress. These techniques are extremely useful in monitoring the health of a component in service. In addition, saving costs on routine check-ups; an example is the ultrasound approach. Current techniques for residual stress measurement are presented in the flow chart below (Figure 1.4). Description of these techniques is provided, which reviews a prior study of the measurement techniques to determine the appropriate method to use in this research.

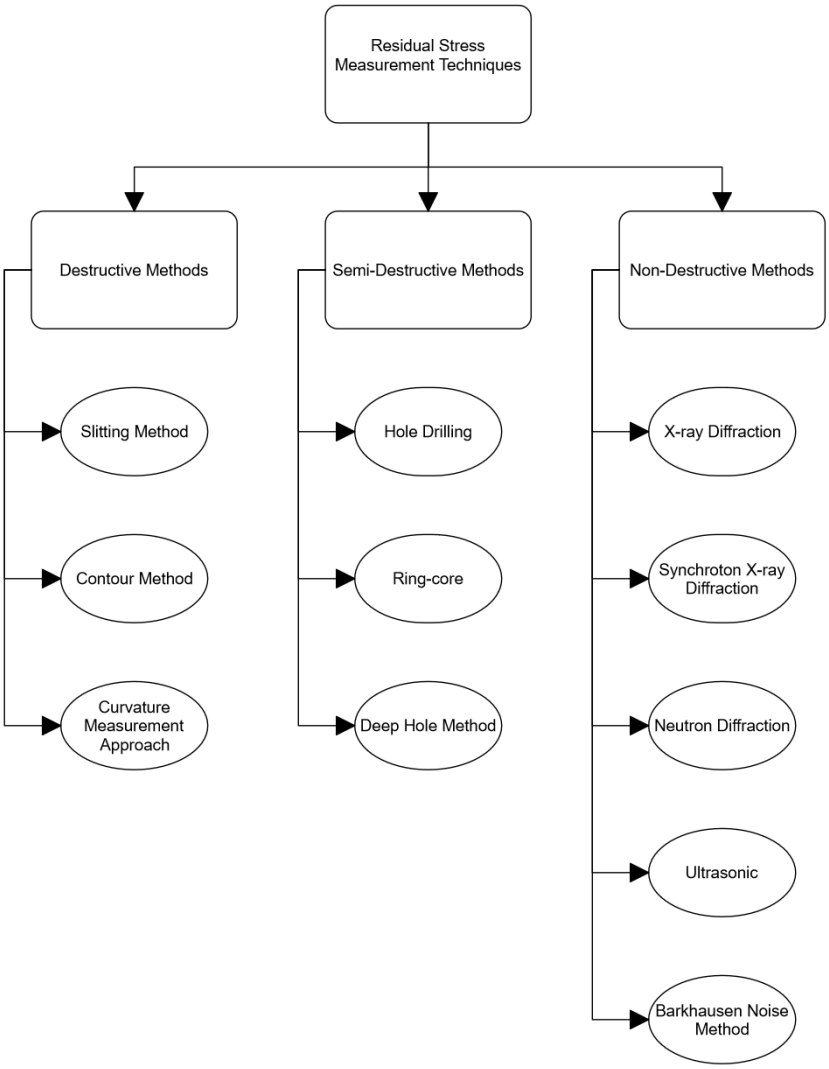

Figure 1.4: Current measurement methods for residual stress determination.

1.2.1. Destructive methods.

Destructive methods are widely used due to their simplicity, high accuracy and reliability. Three different methods were reviewed which are the slitting, contouring and curvature measurement techniques. The **slitting** principle is simple, where a cut is made through the use of electric discharge wire, leading to the relaxation of the material near the slit faces, these relaxations are measured and recorded. Finite element models (FEM) are used to invert these strains into stresses through the use of power series [17]. Slitting is highly suited for through thickness measurements and require very light surface preparation for the strain gauges. It is also very affordable, fast, and provides excellent repetition of results. A major downside of this technique, is that it is still a laboratory method since there is no appropriate portable cutting machine. In addition, the FE model becomes an issue for complex geometries, as it requires a full understanding of the limitations and boundaries of the problem in order to obtain reliable results.

Contouring is basically performed by cutting the component into two halves, then the deformations normal to the cut face are measured using a coordinate measure machine (CMM). Analogously to the slitting method, FEM is used to invert the measured strains into stresses, where the model is based on superposition principle. The complexity of the FEM model and the immaturity of the technique are the main challenges faced when using this method. Contouring is the newest destructive method—it was introduced 17 years ago during a conference [17].

Curvature measurement method is done by etching layers of one side of the component either mechanically or chemically and measuring the strain on the other side. This method was proven valid to measure deep bi-axial macro-stresses but not surface stresses [17]. Simple mathematical equations were utilized to measure the macro-stresses. Material type and geometry of the component are the main obstacles to measure residual stresses.

Analyzing the destructive methods lead to the conclusion that these methods are inadequate to be used for this study due to the high level of damage inflicted upon the structure which renders the part unusable after the test. In addition, the slitting and the contouring methods rely on the use of proper cutting machine usually an electric discharge machine (EDM) is used, which could not be used for a material such as GLARE since it is not a conductive material.

1.2.2. Semi-destructive methods.

The working principle behind these techniques is the same as the destructive methods, where strains from removal of material is measured, then inverted to stresses. A positive aspect of semi-destructive methods is that the induced damage is usually minor and repairable, so multiple measurements on the same component can be performed. **Hole drilling** and **ring core** are similar techniques in their mathematical and theoretical approaches, where the only difference lies in the strain gauge setup. The gauges in ring core techniques lie within a ring where material is removed through the use of a technique known as Trepan technique [17]. Figure 1.5, illustrates the placement of the strain gauges in the hole drilling technique on the left and the ring core method on the right. The latter provides better distribution of the residual stresses measured, given that it measures a larger area of relieved stresses [17]. Although it may therefore seem the better method, it is more difficult to prepare; substantial time and expertise are required to remove the material.

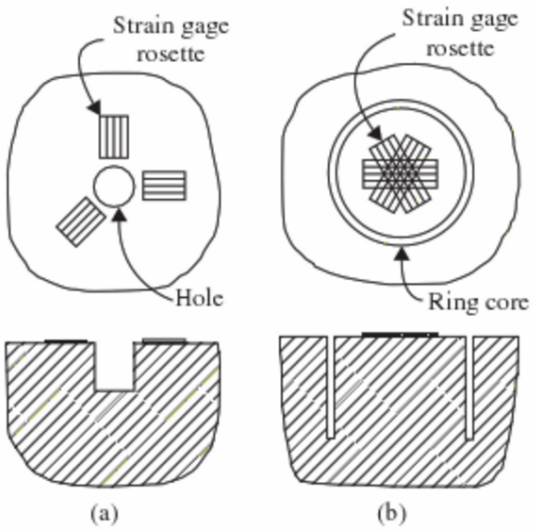

Figure 1.5: Strain gauge positions for a) hole drilling technique and b) ring core technique [17].

Hole drilling is an affordable, fast, and popular method across different engineering fields. It is applicable to metals, ceramics, and plastics with known elastic parameters. Moreover, it can be used to measure bi-axial stresses, though the out-of-plane stress is measured with low accuracy and high difficulty. The main issue with this method is the introduction of stresses due to drilling process. In order to minimize measurement errors, accurate tooling and a high level of experience with handling the method are required. The third option, **deep hole drilling** (DHD), mainly differs in the fact that the strain gauges are positioned within the hole inside walls. This technique was originally developed for the analysis of rock mechanics and was later introduced to the fields of civil engineering and aerospace. However, it is mostly used for large isotropic components with a minimum thickness of 6 mm.

1.2.3. Non-destructive methods.

These techniques do not introduce any damage to the specimen and are favored among many manufacturers. While these techniques boost production and efficiency, their disadvantages lie in the high initial costs of the tooling and complexity of the calibration systems. The immaturity of nondestructive techniques hinders their implementation and efficient use in the industry for the purpose of determining residual stresses. This is particularly true for new materials such as GLARE, given the complexity of the material itself. In addition, the testing equipment are designed with high correlation to the component geometry, which is unfeasible for this study.

Diffraction methods such as X-ray and neutron diffraction are capable of measuring both micro and macro stresses in metallic as well as ceramic structures, based on the crystallization order of the atoms. The principle as stated before is to monitor a physical property related to stress, which is the inter-planar spacing between the atoms in this case. The strain is found by comparing the spacing in a stressed state with a stress free state, then the stress is obtained using general stress-strain relation. Both diffraction methods are similar in principle but differ in penetration level. Neutron diffraction has the greater penetration level, but its initial investment cost is significantly higher than that of X-ray diffraction. The penetration level of an X-ray limits its use to surface measurements with high reliability.

Ultrasonic method is another variant of the non-destructive method, which depends on the acoustoelastic effect of ultrasonic waves [17]. This effect entails that the acoustic waves travel with varying speeds in different materials and are effected by the introduction of stress. By appropriate implementation and understanding of the fundamentals, reliable and concise results are obtained. The sensitivity of this method depends on the type of material and it's geometry. Ultrasonic method is typically used in product quality checks given its rapid testing and no requirement of surface treatments. The major downside to this method is that it is required to have a reference sample in a stress free state with the same structure to compare it to the stressed state, which is not possible for GLARE laminates.

Other magnetic techniques are available but were excluded from this thesis due to their lack of applicability. An example is the Barkhausen noise (MBN) method, which is used for ferromagnetic materials and thus has limited benefits to this study.

1.3. Thesis Strategy & Structure

In this study, the objective is to formulate an approach to measure residual stresses in structures after manufacturing. Upon inspection of the various techniques, hole drilling was selected. This choice is mainly due to this method's simplicity, reliability, and applicability to a range of materials. Furthermore, the tools required for experimental runs are the most suitable with respect to material type, available equipment, and expertise. The other semi-destructive methods are more difficult to perform experimentally. In this study, surface deformations due to hole drilling are measured with conventional measurement devices, rather than highly advanced optical measurements, which require complex and massive numerical models that are beyond the scope of this thesis. Furthermore, the use of strain gauge rosettes to measure the strains is standardized within the ASTM E837 method, and is widely used.

Accordingly to the objective of the study, a research strategy is implemented to accomplish the stated goal. Fiber metal laminates (FML) are manufactured with aerospace standards to be used throughout the study. The hole drilling process according to the standard provided ASTM E837-13 is analyzed and implemented, where, the released strains are monitored and recorded. Simultaneously, a numerical model is built using a finite element software named ANSYS [27], to provide the means to determine calibration constants; these constants are coefficients that relate the strain response to its associated stress applied. The simplest form of this is Hooke's law ($\sigma = E\epsilon$) where the modulus relates the strain to its associated stress. Numerical simulations of hole-drilling are built for isotropic, orthotropic, and hybrid materials. In these numerical simulations, residual stress is applied in the magnitude of 1 MPa then the strain response is determined. By analyzing the relation between the stresses

and strains from the simulation, the constants are found. Verification of the models is done by verifying the obtained coefficients with the ones provided in the ASTM E837 Standard for isotropic materials, and with the coefficients determined by Schajer and Yang [21] for orthotropic materials.

Afterwards, the actual residual stresses within the manufactured laminates are determined, by using the experimentally measured strain with the computed coefficients. Upon determination of the residual stresses, their verification with the theoretical stresses is essential to confirm the validity of the method. The theoretical stresses are calculated using the classical laminate theory (CLT).

With the research objective in mind, the thesis is constructed in the following manner: basic definitions and concepts used throughout the study are reviewed in chapter 2. Chapter 3 discusses the mathematical background of the hole drilling method and classical laminate theory, followed by the experimental set up, procedure, and results in chapter 4. In chapter 5, the numerical models built using ANSYS are explained and verified by comparing the computed calibration coefficients to the theoretical constants provided by the ASTM [4] or Schajer and Yang work [21]. Validation of the hole drilling method to determine residual stresses within GLARE is presented in chapter 6. Finally, concluding remarks and recommendations are presented in chapter 7.

2

Literature Review

Several concepts are discussed in this chapter to provide the literature background for this study. As the main purpose of the study is to investigate residual stresses, understanding the types and sources of residual stresses is essential. In addition, the history of innovative composite material is briefly discussed, with particular attention to manufacturing processes. The chapter concludes with a brief description of the hole drilling method.

2.1. Types & Sources of Residual Stresses

Residual stress origins and sources are defined through intensive research to improve decision making during the design phase of a product and are classified as mechanical, thermal, or chemical stresses. In the study of a component's fatigue performance, show that unintentional tensile forces could have detrimental consequences for the component life cycle. In contrast, compressive forces usually are induced to improve the fatigue performance of parts [22]. This improvement in fatigue is due to the fact that compressive stresses work in the opposite direction of the forces applied, which mitigates the magnitude of the total exerted force such as in the case of plastic hole expansion [22]. While tensile stresses occur in the same direction of the force exerted, amplifying the force magnitude which leads to earlier failures than expected. A schematic of the mechanical, thermal, and chemical induced stresses in a base material is presented in Figure 2.1.

Mechanically generated stresses are mostly due to manufacturing processes such as machining and cold working. Cold working process implies that plastic deformation of the component occurs which results in a residual stress distribution within the material [22]. Machining induces stress mainly due to the change in the shape of a component by cutting or removing layers of the material, in addition, the introduction of plastic deformations. Moreover, stresses are created due to assembly of different parts together, which is a result of their dimensional tolerances variation.

Thermal Stresses are generated due to mismatch of coefficient of thermal expansion (CTE), temperature fluctuations and heat treatments. First, manufacturing of components with different constituents such as metal hybrid or composites, entails the use of different materials with varying CTE. The constituent with the lower CTE will constrain the other constituent from expansion, which will introduce a distribution of residual stresses. Second, thermal stresses created by temperature changes results in distortions, change in shape of the component and introduction of stresses, one example of this is welding. Finally, heat treatments processes induce stresses within parts by altering the thermal gradients through heating or cooling and controlling the rate of temperature change. Examples of such processes are annealing, tempering, and quenching.

Chemically induced stresses are the consequence of surface treatments, such as nitriding, carbonizing, and ion implantation. This process entails altering the surface by diffusing or modifying the material composition to improve the life span of the product and its corrosion resistance. Surface treatments are widely used in fields like the aerospace and automotive industry.

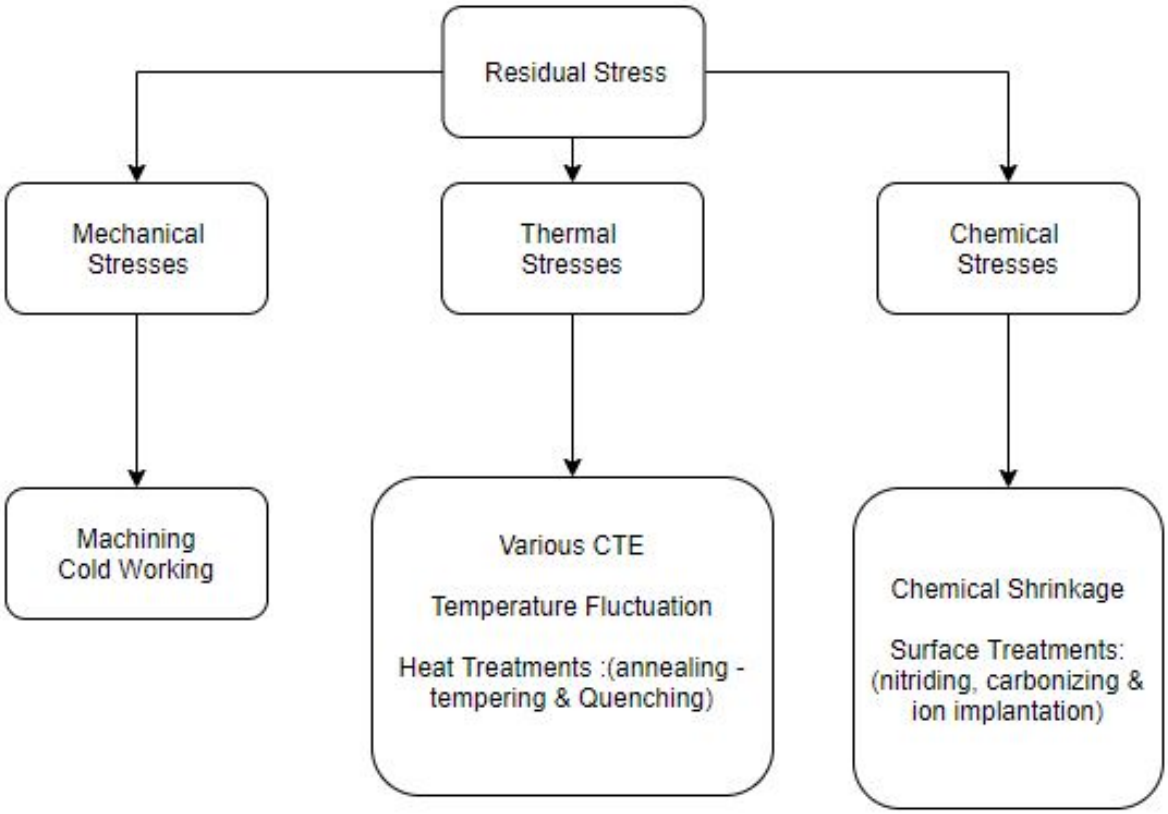

Figure 2.1: A schematic classification of mechanical, thermal, and chemical induced stresses in a base material.

In thermoset and thermoplastic composites, three sources of residual stresses are established: micro stresses between individual fibers within a lamina, macro stresses between plies caused by the multiaxial orientation of the plies within a laminate, and macro stresses generated by the mismatch of CTE of the laminate constituents during consolidation and solidification processes of composites. The micro residual stresses in composites result from polymerization during the curing process due to the mismatch in the volume change between the fibers and matrix; this volume change is known as chemical shrinkage [1]. The macro-stresses generated given the multiple fiber directions within the laminate, which are oriented differently to account for the expected loading. This orientation is required because of the anisotropic nature of composites. The 10% rule is typically recommended in designing composite laminates, meaning that at least ten percent of the laminate's total stiffness should be applied in all possible load direction.

2.2. Materiology

Presently, thousands of materials are available to engineers to use for different purposes and applications, ranging from standard isotropic metals that have been around for several hundred years, such as cast iron, copper and brass [8], to more complex structures like composites and ceramics. A composite is defined as a heterogeneous combination of two or more homogeneous constituents bonded together, each with its own distinctive properties to provide a structure with unique properties that are not achievable by its individual components. This definition is generally applicable to many structures and materials, but the focus of this study is hybrid structures with constituents which are fibers, matrix and Aluminum, where the fibers may be continuous or discontinuous [6].

The material behavior of these hybrid structures is far from isotropic, as their mechanical response is directional dependent—these materials are considered anisotropic. Anisotropy is a property in which the mechanical properties of the material differ depending on the material orientation. Assuming linear elasticity for an anisotropic material, the stress-strain relation of such a material is presented by the generalized form of Hooke's law. The generalized form of the law, also known as the stiffness matrix, contains 36 elastic constants, where each stress

component depends on all the strain components. Which means that in-plane stressing of the component would lead to in-plane and shear strains, as illustrated in Figure 2.2.

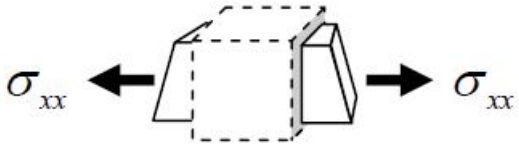

Figure 2.2: A unit of material undergoing shear deformation due to in-plane uniform stress.

$$\begin{bmatrix}\sigma_1\\ \sigma_2\\ \sigma_3\\ \tau_4\\ \tau_5\\ \tau_6\end{bmatrix} = \begin{bmatrix}C_{11} & C_{12} & C_{13} & C_{14} & C_{15} & C_{16}\\ C_{21} & C_{22} & C_{23} & C_{24} & C_{25} & C_{26}\\ C_{31} & C_{32} & C_{33} & C_{34} & C_{35} & C_{36}\\ C_{41} & C_{42} & C_{43} & C_{44} & C_{45} & C_{46}\\ C_{51} & C_{52} & C_{53} & C_{54} & C_{55} & C_{56}\\ C_{61} & C_{62} & C_{63} & C_{64} & C_{65} & C_{66}\end{bmatrix}\begin{bmatrix}\epsilon_1\\ \epsilon_2\\ \epsilon_3\\ \gamma_4\\ \gamma_5\\ \gamma_6\end{bmatrix} \tag{2.1}$$

Fortunately, in most materials at least some symmetry is found within the orthogonal planes of the microstructure. The lamina, which consists of fibers and matrix constituents, have three symmetrical orthogonal directions. Thus, the generalized form (2.1) is simplified and reduced to a simple form (2.2) with nine elastic constants, and expressed in terms of engineering constants as follows:

$$\begin{bmatrix}\epsilon_1\\ \epsilon_2\\ \epsilon_3\\ \gamma_4\\ \gamma_5\\ \gamma_6\end{bmatrix} = \begin{bmatrix}\frac{1}{E_1} & -\frac{\nu_{21}}{E_2} & -\frac{\nu_{31}}{E_3} & 0 & 0 & 0\\ -\frac{\nu_{12}}{E_1} & \frac{1}{E_2} & -\frac{\nu_{32}}{E_3} & 0 & 0 & 0\\ -\frac{\nu_{13}}{E_1} & -\frac{\nu_{23}}{E_2} & \frac{1}{E_3} & 0 & 0 & 0\\ 0 & 0 & 0 & \frac{1}{G_{23}} & 0 & 0\\ 0 & 0 & 0 & 0 & \frac{1}{G_{13}} & 0\\ 0 & 0 & 0 & 0 & 0 & \frac{1}{G_{12}}\end{bmatrix}\begin{bmatrix}\sigma_1\\ \sigma_2\\ \sigma_3\\ \tau_4\\ \tau_5\\ \tau_6\end{bmatrix} \tag{2.2}$$

Where:

1. E_1, E_2 and E_3 are the Young's elastic modulus in the 1, 2, and 3 material directions.
2. ν_{12} is the Poisson's ratio, providing the ratio between the transverse (2-plane) and normal strain (1-plane) for the applied stress in material direction 1, ν_{13} and ν_{23} are similarly described.
3. G_{12} represents the shear modulus in the associated plane; thus shearing in the 1-2 plane, G_{13} is similarly described. It is important to note that the 3-plane is usually considered the out of plane direction; thus, G_{23} is the transverse shear modulus.
4. The other three Poisson's ratios ν_{21}, ν_{31} and ν_{32} are dependent since symmetry of the stiffness matrix implies that $\nu_{12}E_2 = \nu_{21}E_1$, $\nu_{13}E_3 = \nu_{31}E_1$ and $\nu_{23}E_3 = \nu_{32}E_2$.

These nine elastic coefficients are sufficient to describe and assess the behavior of a laminate consisting of multiple plies or laminae. However, for a single ply or lamina, it is important to clarify that there is no shear coupling, meaning that normal strains are only caused by normal stresses, and shear strains are only caused by shear stresses. This effect reduces the stress-strain relation to depend only on four elastic moduli. Therefore, a lamina is classified as a transversely orthotropic material.

The transversely orthotropic lamina consists of unidirectional fibers oriented in the 0° to carry the primary load in the normal direction, whereas the perpendicular direction (90°) depends only on the strength of the matrix, which is only capable of carrying low loads. Although it may seem logical to orient all the available plies in the direction of the primary load case, this strategy is rarely taken in practice, since it is much more convenient to have a balanced laminate to account for more than one load direction. An example of this is the quasi-isotropic laminate (Figure 2.3), where the fibers are oriented in four load directions to provide a better distribution of the extensional properties but it is important to note that qausi-isotropic structure limits the benefit of anisotropy,

thus analysis of the structure stress state is crucial to obtain the most optimal solution.

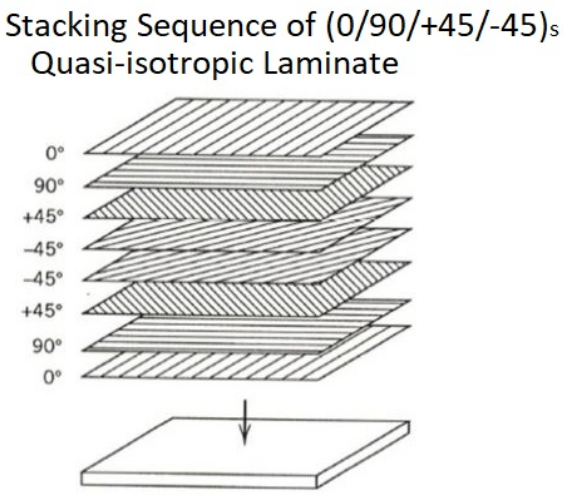

Figure 2.3: Presentation of a quasi-isotropic lay-up.

2.2.1. History & Innovation of Composites

The first significant use of composites occurred in the late 1950s, when the Akaflieg Phönix FS-24 (Figure 2.4) was built using fiber glass and balsa wood sandwich design. The sandwich design was based on the work of professors and students at the University of Stuttgart, where they produced a balsa wood and paper sailplane. The application of composites was further exploited by the helicopter industry at the end of 1960s. The helicopter industry was the first to use composites to build primary structures, such as the rotor blades in the Aerospatiale Gazelle (Figure 2.5). This event was followed by an increase in the use of composites for smaller conventional aircrafts in the 1970s. As interest grew, studies were conducted in order to understand the behavior of composites. The use of composites in larger aircrafts was first approved by the FAA in 1980s for the Beech Starship I (Figure 2.6), whose fuselage was fully made out of graphite and epoxy face sheets with a Nomex core sandwich structure [8].

Figure 2.4: The Akaflieg Phönix FS-24 aircraft [8].

Figure 2.5: The Aerospatiale Gazella aircraft [8].

The extensive research on composites and the quadruple increase in fuel prices for political reasons at the start of the 1980s lead to requests to replace metallic structures with lighter composite ones, such as the horizontal stabilizer in the Boeing 737 or the horizontal and vertical stabilizers in the Airbus A-320. Up until this point, the main focus was developing the sandwich design of composites. However, in the 1990s, the use of Fiber Metal Laminates (FML) began with GLARE, one of the most promising new materials introduced to the aeronautical industry, as it was found to perform well under impact. It was therefore incorporated in the Boeing 777 as the cargo floor, and ever since, the use of hybrids to replace aluminum-based parts in aircrafts has increased gradually. Moreover, years of experimental research have shown that GLARE has better fatigue, corrosion, and residual stress performance than aluminum. The increase in the use of composites in large civilian aircrafts peaks in the current century with 50% of the Boeing 787 and 60% of the A-350 (Figure2.7) being composite [8].

Figure 2.6: The Beech Startship I approved by the FAA [8].

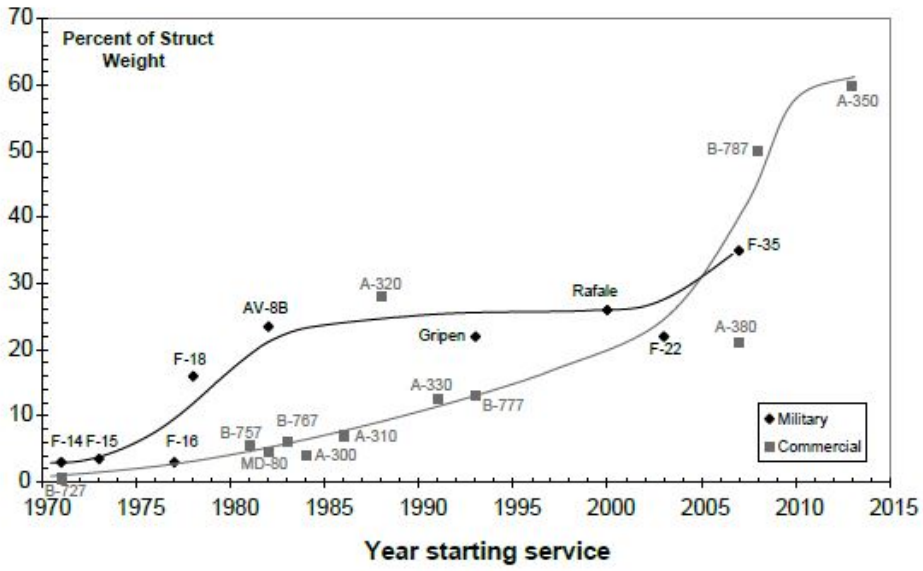

Figure 2.7: Illustration of the increase in composite usage in modern aircrafts.

2.2.2. Manufacturing of Composite Laminates

General production of composite products are divided in four steps. **[1]** forming where the constituents are changed into the desired shape usually through the appliance of temperature and pressure. **[2]**, machining is used to remove or trim any undesired part of the structure. **[3]** the parts are joined and assembled together through bonding or mechanical joining. The assembly phase is a time consuming process and costly, thus it is favorable to minimize it by integrating parts in one production cycle which entails less riveting resulting in less stress raisers. **[4]**, finishing is done for environmental resistance and smoother outside surface [11]. Manufacturing concepts are quite similar for various types of composites. Impregnation is the first step where the fibers and resins are mixed together, mostly in a controlled environment to avoid any contamination. Impregnation is either performed at the start of production cycle or prior to it by the material supplier known then as prepregs. Second, stacking and layup of the prepreg lamina is performed on a preshaped mould according to the desired orientation, this step is crucial in achieving the required composite architecture that satisfies the design requirements. Layup is either done by hand or through automated robots. In the case of FML, some of the prepreg layers are replaced by metal layers. Finally, consolidation and solidification are required to obtain the finished part. Consolidation is used to create contact between the adjacent layers to remove entrapped air during processing, usually performed using vacuum pressure. Solidification or curing is performed for advanced composites, in a controlled environment—GLARE, for example, requires an autoclave. This is mainly to obtain a good quality part, in addition, speeding up the curing process for thermosets by increasing the temperature, while for the thermoplastics the temperature is decreased to obtain faster solidification [11].

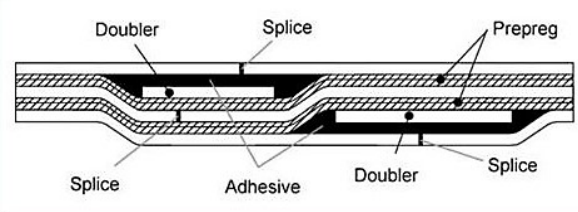

Figure 2.8: Illustration of the splice in self forming technique used in GLARE manufacturing [1].

Further concepts essential to the manufacturing of FML are the splicing and self forming techniques (SFT) shown in Figure 2.8. The overlap splicing technique was introduced in order to overcome the limitation from the dimensions of the constituent materials by splicing and to have sufficient margins with respect to tolerance

by overlapping. The overlap splicing is performed with minimum consequences for the thickness, resulting in lighter and wider panels but with higher chances of delamination. This drawback is hindered by applying doublers, which can be placed either internally or externally [24] . The SFT is used to produce laminates with splices and doublers in one curing cycle. The curing is performed within an autoclave to ensure the pressure required. Filling the gaps in between the metal sheets with adhesive increases the shear and delamination strength of the laminate as the load transfer becomes less critical at the gaps. In some cases the efficiency of the component is increased by using the prepreg layers as doublers within the splices, thus saving weight [1]. The main reason doublers are usually applied is to increase the thickness locally at certain locations such as windows or cutouts where local strengthening is required.

Production limitations of FML are the formability and machinabiltity. Formablility of the FML is limited, because bending of the laminates is directly dependent on the allowable deformation of the fibers or resin, thus the small limit strain of FML for failure; specifically GLARE makes it inadequate for forming processes. In addition, Machining as stated before should be controlled to minimize stresses created by it, and to avoid delamination of the laminate.

2.3. Hole Drilling

A brief introduction to the hole drilling method and its recent applications. In addition, the history of this technique and other relevant research are briefly discussed.

2.3.1. Introduction to Hole Drilling

Hole drilling as a semi-destructive method entails an acceptable minimal damage to the specimen, which is usually repaired or removed afterwards. Since minimal damage is inflicted, it is possible to conduct multiple local inspections to improve the measuring output. The basic procedure for hole drilling is performed by drilling a small hole in the specimen, resulting in elastic relaxations of the surrounding areas due to removal of the material, as depicted in Figure 2.9 [17]. The magnitude of the relaxation is on the scale of a couple hundred micrometers and sometimes less than one hundred microns. The conventional method for measuring the stresses is through the use of strain gauge rosettes. These standardized gauges have three main measurement directions for the uniform in-plane stresses σ_x, σ_y and τ_{xy}. Three different types of strain gauge rosettes are mainly used: type A, which is used in general cases; type B, which is most suitable in the case of near obstacle measurements; and type C, which contains half bridge circuits that account for thermal errors. The standard test procedure is thoroughly presented in the ASTM test method [4], which includes surface preparation, assumptions, and limitations.

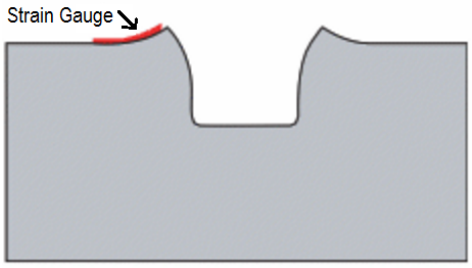

Figure 2.9: Relaxation of the surrounding areas after hole drilling [17].

One example of hole-drilling application is on welding components that leads to the presence of residual stresses due to phase change, high temperature fluctuations in the Heat Affected Zone (HAZ) and shrinkage [25]. Hole drilling is applied by mounting the strain gauges on the surface of the HAZ (Figure 2.10) then acquisition of the strain responses is performed accordingly to the ASTM E837 standard. Furthermore, a simple analysis variant of hole drilling known as the Through Hole Method is used to determine the stresses in a straight forward wise is done. The maximum tensile and compressive stresses at the top layer were found to be equal to 1694 MPa and 105 MPa respectively [25]. Further description of the method is provided in the third chapter.

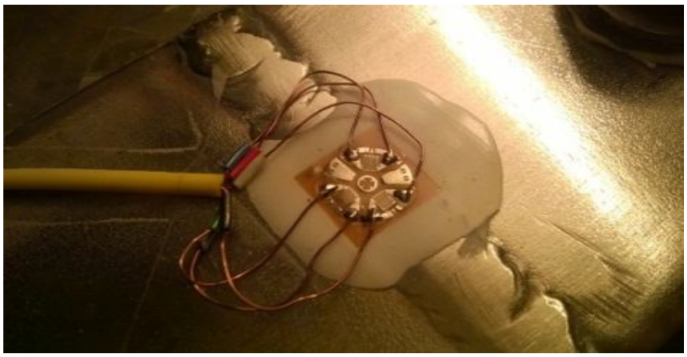

Figure 2.10: Strain gauge rosette installed on the HAZ [23].

2.3.2. History & Innovations

The research conducted by Mathar in the 1930s is the basis for the hole drilling method [17]. Mathar used a mechanical extensometer that limited the capability and reliability of his method to measure residual stress. A decade later, Soete applied strain gauges invented in the 1940s to measure the released strains from hole drilling, increasing the method's accuracy, capabilities, and reliability [25]. Extensive research was performed to improve the technique, notably including Kelsey's proposal to use incremental hole drilling in order to obtain the stress profile through the thickness [9]. In 1966, Rendler and Vigness developed the basic procedure for residual stress determination. Their method was built on the idea of using a standard strain gauge orientation to relate the relieved strain to stresses through calibration coefficients [15]. This idea initiated the process to standardize the method, as provided in the ASTM standard E837, which was first presented in 1981 [17].

In the modern age of high computational power and discretization, the accuracy of stress profiles using the ASTM-E837 has dramatically improved. However, the ASTM standard is based on the assumption that the material is linear, elastic, and isotropic. In consequence, the introduction of innovative composite structures, which are anisotropic materials, raised doubt over the validity of the method. This issue was first addressed by Bert et al. in 1968, followed by Prasad et al. in 1987, where both studies assumed that the released strains in anisotropic materials have a trigonometric response similar to the isotropic case [21]. This assumption was later proven invalid by Schajer and Yang in 1994 [21], and they introduced new calibration constants assuming only linear elasticity, whereas the coefficients are not trigonometric based anymore. Finally, in 2016, Ghasemi and Mohammadi demonstrated that the incremental hole drilling method can be successfully used for fiber metal laminates (FML) such as GLARE [7].

3

Theory and Methodologies

Identification of stresses acting upon a structure is an essential factor in understanding and predicting the behavior of any component. These residual stresses are a directly dependent on the internal strains in the elastic region of a component. The key theoretical methodologies used within the study are described in this chapter. First, the hole drilling method used to obtain residual stresses is discussed in detail. Second, the classical laminate theory used to verify the final results is presented.

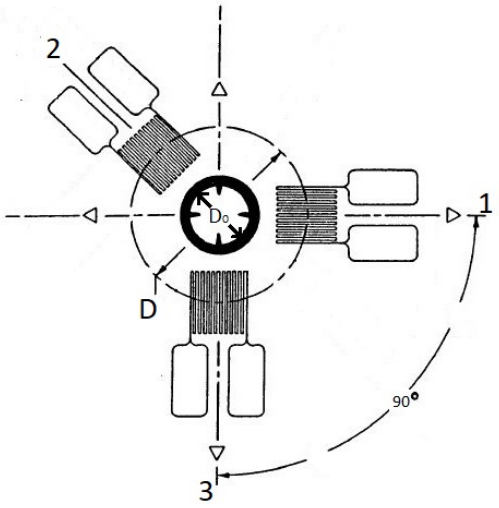

Figure 3.1: ASTM oriented strain gauges.

3.1. Hole Drilling Methodology

The hole drilling method determines residual stresses in linear elastic materials by gauging the strains at the surface of the material. The surface strains are generated due to the removal of material by drilling a hole at the geometric center of a rosette, which causes the surrounding material to relax, and a new stress-state is reached. The determined strains are then inverted into residual stresses using a set of numerically calibrated coefficients. It is therefore essential for the choice of strain gauge type to be set beforehand, as each rosette type has different sets of coefficients. The adopted orientation of the gauges is the type A strain gauge rosette, which is presented in the ASTM standardized test method. The type A rosette used for this study (Figure 3.1) comprises three strain gauges equidistantly oriented around the hole. The first gauge is defined as the reference direction, the second gauge is oriented 135° anti-clockwise to the reference direction and the third gauge is orthogonal to the reference direction. Important dimensions to note are the hole diameter $[D_0]$ and the rosettes circle diameter $[D]$, because the stress-strain sensitivity of the measurement is directly proportional to the ratio (D_0/D).

The standardized hole drilling technique comprised of two different stress gradients: the stress profile is considered to be either constant with depth or significantly changing with depth. The former, known as uniform stress, is applicable to relatively thin components, where the thickness is less than $(0.4D)$, and the latter, known as Non-uniform stress profiling, is performed for relatively thick components with thicknesses greater than $(1.2D)$. $[D]$ is the rosette gauge diameter. In other words, the standard hole drilling method presented covers thicknesses less than $(0.4D)$ or greater than $(1.2D)$. Intermediate thicknesses are considered to be finite components that require further investigation beyond the scope of the standardized test given the increased challenges. These challenges are addressed in the upcoming sections.

3.1.1. Uniform Stress

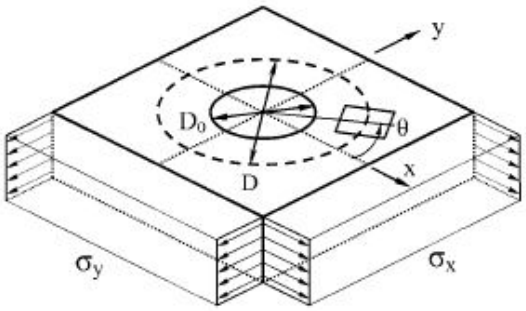

Figure 3.2: Uniform stresses at a flat component.

Considering the case presented in (Figure 3.2) where the in-plane stresses are constant with depth, the strain is measured during the central hole drilling by the gauges positioned at a location far from any edge or surface irregularities. The stress-strain relationship [4] between the relieved strains and their associated residual stress is

$$\epsilon = \frac{\sigma_x + \sigma_y}{2}\frac{(1+\nu)a}{E} + \frac{\sigma_x - \sigma_y}{2}\frac{b}{E}\cos 2\theta + \tau_{xy}\frac{b}{E}\sin 2\theta \tag{3.1}$$

In this equation $[\epsilon]$ is the measured strain, σ_x, σ_y and τ_{xy} are the in-plane stresses, $[\theta]$ is the incline angle between the component Cartesian x-y system and the strain gauge axis, ν is the Poisson's ratio, and the coefficients $[a]$ & $[b]$ are calibration coefficients that defines strain-stress sensitivity [17], which are computed using finite element analysis (FEA). A scalar value is found for each drill step using equation (3.1). The coefficients depend on the trigonometric dimensions such as hole diameter $[D_0]$, depth $[h]$ and the rosettes circle diameter $[D]$, therefore, they differ in each situation and for every gauge type. A study conducted by Schajer shows (Figure 3.3) that the coefficients variation with depth reaches a limiting value when the ratio (h/D) exceeds 0.4 D, which means that the strain gauges do not measure much strain variations by drilling to larger depth [17]. Noting that the magnitude of this ratio is approximately equal to the hole diameter $[D_0]$. This implies that choosing the upper limit of the allowable hole diameter results in a more reliable outcome; however, this is limited in order to avoid causing any damage to the strain grids.

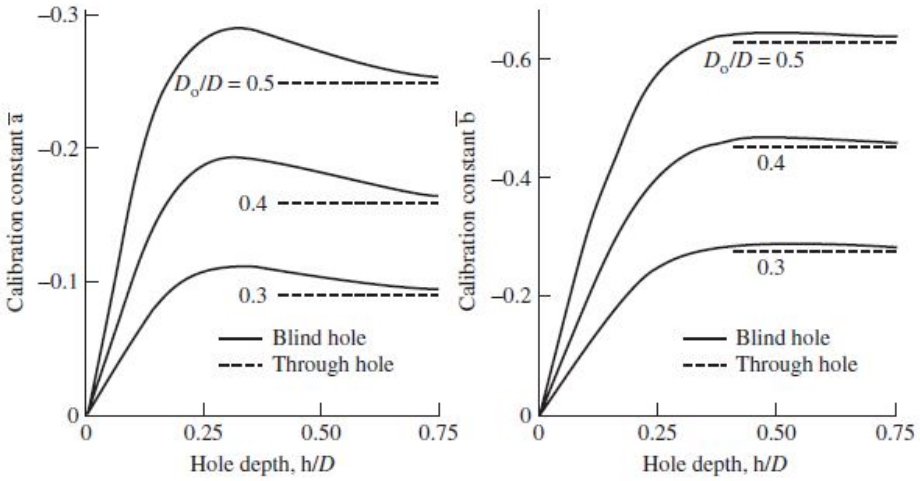

Figure 3.3: Calibration Coefficients (a & b) for a type A rosette [17].

The mathematical iteration for the uniform stress approach is simple. Because this approach has only three measured strains after each drill step and by using equation (3.1), the three unknown stresses are determined by simple algebra. Uniform analysis is also known as through or blind hole analysis, which entails a hole either being drilled through the thickness of a thin component or to the required depth in thick components. Further simplification of the stress-strain relation is performed by aligning the strain gauges reference direction with the system Cartesian x-axis ($\theta = 0$). Rewriting equation (3.1) as follows:

$$\epsilon = P\frac{(1+\nu)a}{E} - Q\frac{b}{E}\cos 2\theta + T\frac{b}{E}\sin 2\theta \tag{3.2}$$

Where P, Q and T are stress combinations representing the isotropic, 45° shear and axial shear stresses;

$$P = \frac{\sigma_x + \sigma_y}{2} \qquad Q = \frac{\sigma_y - \sigma_x}{2} \qquad T = \tau_{xy} \tag{3.3}$$

Computing equations (3.1 - 3.3) for each gauge, three strain equations are defined with three unknown in-plane stresses. Applying simple algebra, the stress-strain relations are found as follows:

$$P = \frac{E}{(1+\nu)a}p \qquad Q = \frac{E}{b}q \qquad T = \frac{E}{b}t \tag{3.4}$$

Analogously, p, q and t are strain combinations representing the isotropic, 45° shear and axial shear strains;

$$p = \frac{\epsilon_3 + \epsilon_1}{2} \qquad q = \frac{\epsilon_3 - \epsilon_1}{2} \qquad t = \frac{\epsilon_3 - 2\epsilon_2 + \epsilon_1}{2} \tag{3.5}$$

and the stresses are evaluated using:

$$\sigma_x = P - Q \qquad \sigma_y = P + Q \qquad \tau_{xy} = T \tag{3.6}$$

Furthermore, the maximum and minimum tensile/compressive stress can be found using equation (3.7).

$$\sigma_{max}, \sigma_{min} = P \pm \sqrt{Q^2 + T^2} \tag{3.7}$$

Using equations (3.1 - 3.6) is adequately sufficient for isotropic thin-walled structures. However, in the case of thick components, it is advised to drill up to the required depth in smaller segments in order to obtain more accurate and reliable results by averaging the collected data. 10 equal hole increments is recommended for a final depth of 0.2 D [4], beyond that the results are expected to diverge. Averaging is performed using formula (3.8).

$$P = \frac{E}{(1+\nu)}\frac{\sum ap}{\sum a^2} \qquad Q = E\frac{\sum bq}{\sum b^2} \qquad T = E\frac{\sum bt}{\sum b^2} \tag{3.8}$$

3.1.2. Non Uniform Stress

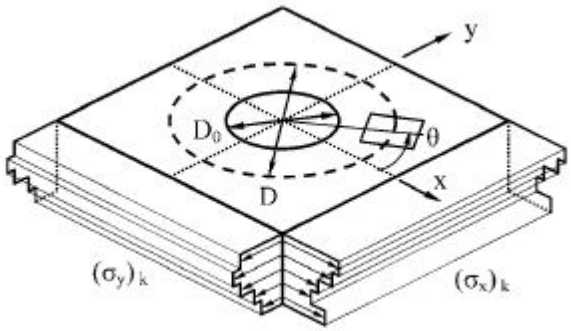

Figure 3.4: Non-uniform stresses at a flat component.

A more generalized approach is the non uniform stress commonly used for various materials, where the residual stresses vary with depth or thickness. In this method, increasing the amount of strain measurements even further is required for a reliable stress calculation; the available standard E837-13 standardizes 20 increments. Finite element modeling is used to determine the calibration coefficient to counter the shortcomings of the theoretical and experimental limitations.

Figure 3.4, presents the stepwise or integral approach, in which the acquired hole depth is drilled in n increments or steps where the in-plane stresses σ_x, σ_y and τ_{xy} are only uniform through one increment. In other words, the strain deformations at the surface are related to the combination of all in-plane stresses through the specimen depth [17]. The stress-strain relation for this integral approach is:

$$\epsilon_i = \frac{1+\nu}{E} \sum_{j=1}^{i} \bar{a}_{ij} P_j - \frac{1}{E} \sum_{j=1}^{i} \bar{b}_{ij} Q_j \cos 2\theta + \frac{1}{E} \sum_{j=1}^{i} \bar{b}_{ij} T_j \sin 2\theta \tag{3.9}$$

Where, ϵ_i is a vector representing the strain combination relieved when the hole depth is attained. Analogously, P_j, Q_j and T_j are vector quantities representing the isotropic stress combinations applied, and the calibration coefficients $[\bar{a}_{ij}]$ and $[\bar{b}_{ij}]$ become matrix quantities that define the stress applied at j depth to the ith hole increment. A physical interpretation of the calibration coefficient $[\bar{a}_{ij}]$ is shown in Figure 5.12, which is performed for four increments. Furthermore, it is important to note that the relieved strains measured at the surface after drilling an increment is a contribution of, first, the removal of material for that drilled increment such as a_{22} and a_{33}, second, the strain resulting from redistribution of prior released residual stresses due to the change in hole depth such as a_{21} and a_{32}.

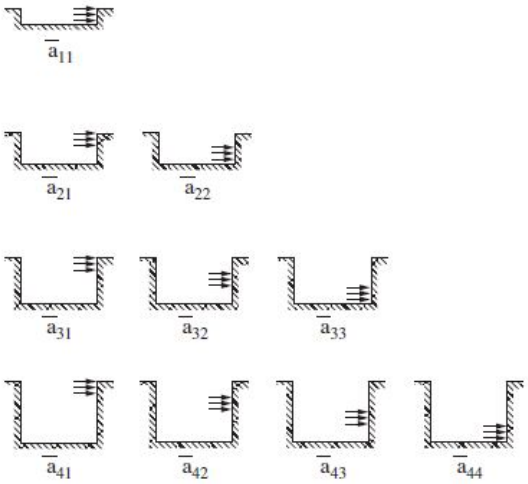

Figure 3.5: Presentation of the step-wise configuration of the coefficients [17].

By generalizing the stress calculation method, equation (3.4) becomes:

$$P_j = \frac{E}{(1+\nu)\bar{a}_{ij}} p_j \qquad Q_j = \frac{E}{\bar{b}_{ij}} q_j \qquad T_j = \frac{E}{\bar{b}_{ij}} t_j \tag{3.10}$$

Where the p_j, q_j and t_j are the strain vectors and analogously using the stress and strain combinations as in equations (3.3 and 3.5). The in-plane stresses at each increment are thus determined.

A physical limitation of the integral method is entailed by a principle known as Saint Venant's Principle, which states that the effect of static loads becomes smaller at sufficient distance away of the load [17]. Thus the deeper the measurements are required, the less accurate they are obtained.

Applying the recommendations to drill 20 increments with the physical interpretation as shown in Figure 5.12 will results in the coefficients matrices $\bar{a}$ and $\bar{b}$ to be numerically ill-conditioned. Therefore, it is suggested to seek the best-fit solution using Tikhonov regularization [17] that smooths the measured data. The regularization is performed with the use of a tri-diagonal matrix c to minimize the noise component in the stress measurements. The generalized equation (3.10) for the P_j vector becomes:

$$(\bar{a}^T \bar{a} + \alpha_P c^T c) P_j = \frac{E}{(1+\nu)} p_j \tag{3.11}$$

Analogously, the same is done for Q and T stress vectors with the matrix c as

$$[c] = \begin{bmatrix} 0 & 0 & & \\ -1 & 2 & -1 & \\ & -1 & 2 & -1 \\ & & 0 & 0 \end{bmatrix} \tag{3.12}$$

The optimization factor α (equation (3.11)) is the regularization parameter that sets the level of result best fitting [17]. An iterative process is required to obtain the optimum value, which eliminates most of the noise without the loss of valuable stress data.

3.1.3. Finite Materials

The hole drilling standard addresses two extreme cases in its approaches, as previously mentioned: components with thickness smaller than 0.4 times the gauge diameter (thin materials) and the more common extreme where the thickness is larger than 1.2 times the gauge diameter (thick materials). As such, the range in between these limits is considerably large. Considering a strain rosette with hole diameter of 2 mm as an example, the intermediate unavailable range is from 1.03 mm to 6.17 mm [4].In order to find a solution for this intermediate range,

the ASTM standard proposes extrapolating the calibration coefficients provided for thin and thick components. However, this is only an approximate solution [4]. Integral drilling in a finite thickness component creates an asymmetrical loading on one side of the component, leading to local bending (Figure 3.6) within the part [18].

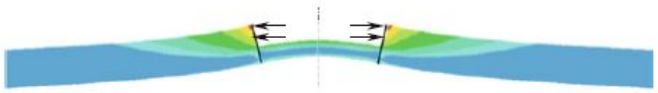

Figure 3.6: A finite element presentation of the local bending created by unsymmetrical loading [18].

Local bending is not apparent in the two extremes because; thin structures are drilled through the whole thickness in one shot, so the load is applied uniformly (Figure 3.7) throughout the thickness without any bending. In contrast, in thick components; presence of material below the hole supports and stiffens the structure, thus suppressing any bending effect from asymmetrical loading [18].

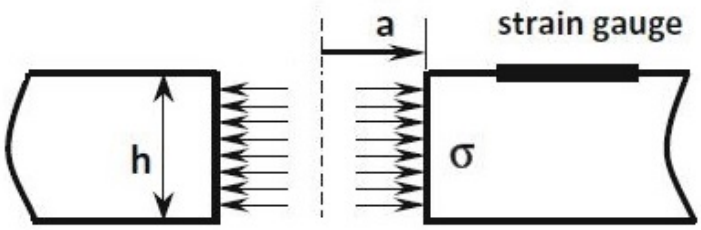

Figure 3.7: Applied loads at the hole boundary in a thin structure.

While the trigonometric equation (3.2) is still valid for isotropic linear material, FEM is required to obtain new calibration coefficients that take the bending effect into account. Gary S. Schajer and Colin Abraham studied the bending effect by simulating a simple model and applying stresses at the hole boundary with a reversed sign, as presented in Figure 3.8 [18].

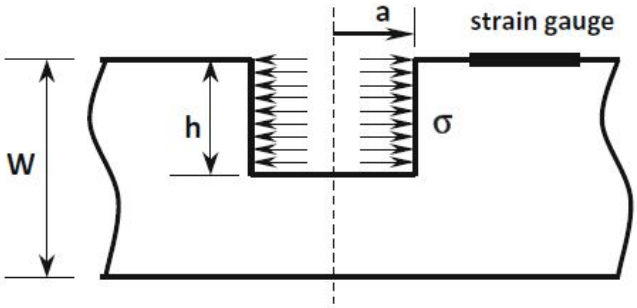

Figure 3.8: A finite element model for simulation of residual stresses at the hole boundary in a finite material [18].

Afterwards, the integral of the strains over each strain gauge area is computed to determine the gauge directional strain, which is used in conjunction with the known stresses to obtain the coefficients. The simulation results are promising: the calibration coefficients a and b presented in Figure (3.9) demonstrate that the calibration constants gradient increases rapidly with decreasing thickness, while the results converge with larger thicknesses. This result supports the hypothesis that increasing the amount of material below the hole stiffens it, hindering the bending effects on the calibration coefficients. It is interesting to note that in the case of shearing coefficient $\bar{b}$, the bending effect is not as apparent and the gradient is smaller due to the fact that the applied stresses in the x and y direction have opposite signs, thus minimizing the local bending effect.

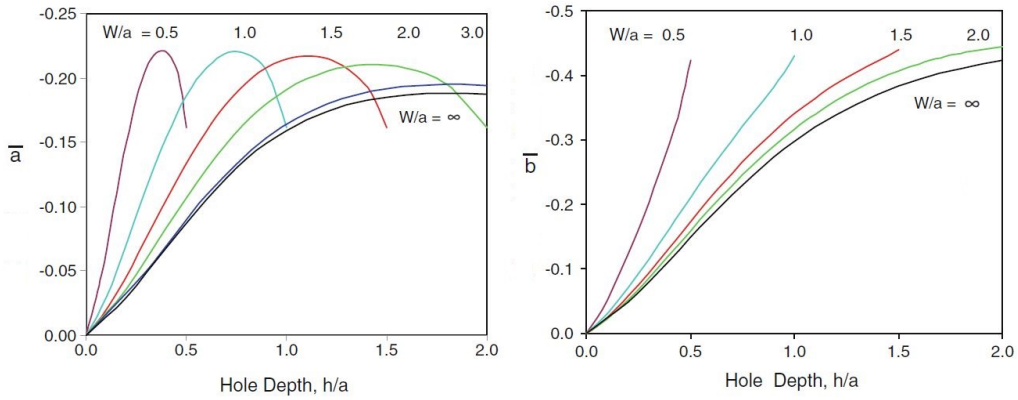

Figure 3.9: The calibration coefficients $\bar{a}$ and $\bar{b}$ for hole drilling in a finite material [18].

3.1.4. Orthotropic Materials

Up until this point, the presented methods to determine the interior stresses are specific to linear isotropic materials. However, the lightness of a structure has become a decisive factor in material selection for part manufacturing in many industry sectors. Consequently, the standardized approach is becoming less applicable due to the orthotropic nature of these materials. Fortunately, advances in computational power and modeling provide the possibility of addressing this issue. The orthotropic nature requires the decoupling of the stress and strain combinations along the x- and y-axis. Although the trigonometrical equation (3.1) is only valid for isotropic materials, it is convenient to rewrite it in matrix form to relate the Cartesian stresses (σ_x τ_{xy} σ_y) to the measured strains (ϵ_1 ϵ_2 ϵ_3) as follows:

$$\begin{bmatrix} A+B & 0 & A-B \\ A & 2B & A \\ A-B & 0 & A+B \end{bmatrix} \begin{bmatrix} \sigma_x \\ \tau_{xy} \\ \sigma_y \end{bmatrix} = \begin{bmatrix} \epsilon_1 \\ \epsilon_2 \\ \epsilon_3 \end{bmatrix} \tag{3.13}$$

Where

$$A = \frac{-\bar{a}(1+\nu)}{2E} \qquad B = \frac{-\bar{b}}{2E} \tag{3.14}$$

The stress-strain matrix form (3.13) demonstrates that only two coefficients A and B are required for isotropic material; however, this is insufficient to account for the orthotropic nature of new structures. The matrix approach can be generalized by assuming only linear elasticity. Generalizing equation (3.13) gives:

$$\frac{1}{E_x \cdot E_y} \begin{bmatrix} c_{11} & c_{12} & c_{13} \\ c_{21} & c_{22} & c_{23} \\ c_{31} & c_{32} & c_{33} \end{bmatrix} \begin{bmatrix} \sigma_x \\ \tau_{xy} \\ \sigma_y \end{bmatrix} = \begin{bmatrix} \epsilon_1 \\ \epsilon_2 \\ \epsilon_3 \end{bmatrix} \tag{3.15}$$

The elastic coefficients c_{11} to c_{33} are a function of orthotropic properties, the rossete, and hole geometric dimensions. The hole depth is a main factor for orthotropic laminates as stated before in the case of isotropic materials where the coefficients reach a limiting factor when the hole depth exceeds 0.4 D. For orthtropic material, the limit depends on the ratio between the out of plane shear modulus to the in-plane axial modulus. The lower the ratio becomes, the faster the hole depth limit is reached [21].

In the matrix form (3.15), the elastic coefficients are made dimensionless through the factor $\frac{1}{E_x \cdot E_y}$. Furthermore, it is important to note that these coefficients vary with each increment associated with vectors of stresses (σ_x τ_{xy} σ_y) and strains (ϵ_1 ϵ_2 ϵ_3) resulting in a stepwise configuration (Figure 3.10) for three increments. The physical interpretation is similar to the integral approach; the only difference lies in the amount of calibration coefficients computed for each drill step.

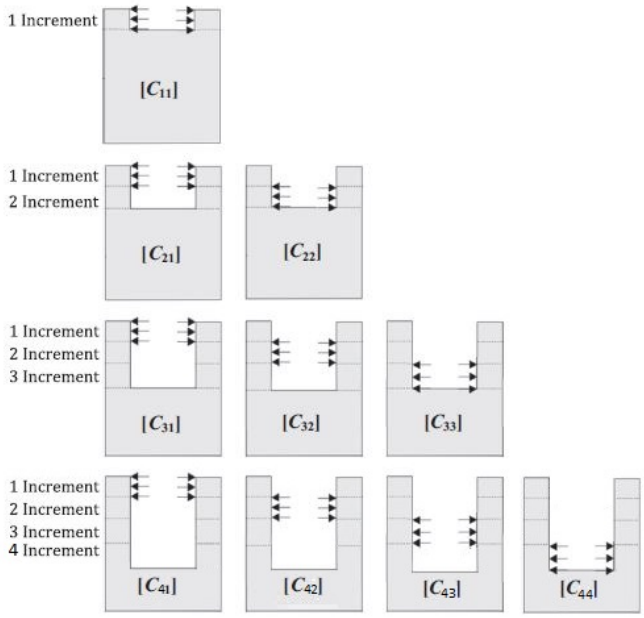

Figure 3.10: Presentation of the step-wise configuration of the coefficients.

The step-wise configuration is structured to include only four increments. Constructing this configuration in matrix form (3.16) illustrates the complexity and immense amount of computation required. The elastic coefficients are written in vector matrices with C_{ij} indices, where the index i is the hole depth increment at which the strain is measured, and j index represents the depth level of the applied stress.

$$\begin{bmatrix} \begin{vmatrix} c_{11} & c_{12} & c_{13} \\ c_{21} & c_{22} & c_{23} \\ c_{31} & c_{32} & c_{33} \end{vmatrix}_{11} & \begin{vmatrix} 0 & 0 & 0 \\ 0 & 0 & 0 \\ 0 & 0 & 0 \end{vmatrix} & \begin{vmatrix} 0 & 0 & 0 \\ 0 & 0 & 0 \\ 0 & 0 & 0 \end{vmatrix} & \begin{vmatrix} 0 & 0 & 0 \\ 0 & 0 & 0 \\ 0 & 0 & 0 \end{vmatrix} \\ \begin{vmatrix} c_{11} & c_{12} & c_{13} \\ c_{21} & c_{22} & c_{23} \\ c_{31} & c_{32} & c_{33} \end{vmatrix}_{21} & \begin{vmatrix} c_{11} & c_{12} & c_{13} \\ c_{21} & c_{22} & c_{23} \\ c_{31} & c_{32} & c_{33} \end{vmatrix}_{22} & \begin{vmatrix} 0 & 0 & 0 \\ 0 & 0 & 0 \\ 0 & 0 & 0 \end{vmatrix} & \begin{vmatrix} 0 & 0 & 0 \\ 0 & 0 & 0 \\ 0 & 0 & 0 \end{vmatrix} \\ \begin{vmatrix} c_{11} & c_{12} & c_{13} \\ c_{21} & c_{22} & c_{23} \\ c_{31} & c_{32} & c_{33} \end{vmatrix}_{31} & \begin{vmatrix} c_{11} & c_{12} & c_{13} \\ c_{21} & c_{22} & c_{23} \\ c_{31} & c_{32} & c_{33} \end{vmatrix}_{32} & \begin{vmatrix} c_{11} & c_{12} & c_{13} \\ c_{21} & c_{22} & c_{23} \\ c_{31} & c_{32} & c_{33} \end{vmatrix}_{33} & \begin{vmatrix} 0 & 0 & 0 \\ 0 & 0 & 0 \\ 0 & 0 & 0 \end{vmatrix} \\ \begin{vmatrix} c_{11} & c_{12} & c_{13} \\ c_{21} & c_{22} & c_{23} \\ c_{31} & c_{32} & c_{33} \end{vmatrix}_{41} & \begin{vmatrix} c_{11} & c_{12} & c_{13} \\ c_{21} & c_{22} & c_{23} \\ c_{31} & c_{32} & c_{33} \end{vmatrix}_{42} & \begin{vmatrix} c_{11} & c_{12} & c_{13} \\ c_{21} & c_{22} & c_{23} \\ c_{31} & c_{32} & c_{33} \end{vmatrix}_{43} & \begin{vmatrix} c_{11} & c_{12} & c_{13} \\ c_{21} & c_{22} & c_{23} \\ c_{31} & c_{32} & c_{33} \end{vmatrix}_{44} \end{bmatrix} \begin{bmatrix} \begin{vmatrix} \sigma_x \\ \tau_{xy} \\ \sigma_y \end{vmatrix}_1 \\ \begin{vmatrix} \sigma_x \\ \tau_{xy} \\ \sigma_y \end{vmatrix}_2 \\ \begin{vmatrix} \sigma_x \\ \tau_{xy} \\ \sigma_y \end{vmatrix}_3 \\ \begin{vmatrix} \sigma_x \\ \tau_{xy} \\ \sigma_y \end{vmatrix}_4 \end{bmatrix} = \begin{bmatrix} \begin{vmatrix} \epsilon_1 \\ \epsilon_2 \\ \epsilon_3 \end{vmatrix}_1 \\ \begin{vmatrix} \epsilon_1 \\ \epsilon_2 \\ \epsilon_3 \end{vmatrix}_2 \\ \begin{vmatrix} \epsilon_1 \\ \epsilon_2 \\ \epsilon_3 \end{vmatrix}_3 \\ \begin{vmatrix} \epsilon_1 \\ \epsilon_2 \\ \epsilon_3 \end{vmatrix}_4 \end{bmatrix} \tag{3.16}$$

In order to compute the real residual stresses at each increment, equation (3.16) is rewritten and the numerically computed coefficients are inverted to be used in conjunction with experimentally measured strain values as follows:

$$\begin{bmatrix} \begin{vmatrix} \sigma_x \\ \tau_{xy} \\ \sigma_y \end{vmatrix}_1 \\ \begin{vmatrix} \sigma_x \\ \tau_{xy} \\ \sigma_y \end{vmatrix}_2 \\ \begin{vmatrix} \sigma_x \\ \tau_{xy} \\ \sigma_y \end{vmatrix}_3 \\ \begin{vmatrix} \sigma_x \\ \tau_{xy} \\ \sigma_y \end{vmatrix}_4 \end{bmatrix} = \begin{bmatrix} \begin{vmatrix} c_{11} & c_{12} & c_{13} \\ c_{21} & c_{22} & c_{23} \\ c_{31} & c_{32} & c_{33} \end{vmatrix}_{11} & \begin{vmatrix} 0 & 0 & 0 \\ 0 & 0 & 0 \\ 0 & 0 & 0 \end{vmatrix} & \begin{vmatrix} 0 & 0 & 0 \\ 0 & 0 & 0 \\ 0 & 0 & 0 \end{vmatrix} & \begin{vmatrix} 0 & 0 & 0 \\ 0 & 0 & 0 \\ 0 & 0 & 0 \end{vmatrix} \\ \begin{vmatrix} c_{11} & c_{12} & c_{13} \\ c_{21} & c_{22} & c_{23} \\ c_{31} & c_{32} & c_{33} \end{vmatrix}_{21} & \begin{vmatrix} c_{11} & c_{12} & c_{13} \\ c_{21} & c_{22} & c_{23} \\ c_{31} & c_{32} & c_{33} \end{vmatrix}_{22} & \begin{vmatrix} 0 & 0 & 0 \\ 0 & 0 & 0 \\ 0 & 0 & 0 \end{vmatrix} & \begin{vmatrix} 0 & 0 & 0 \\ 0 & 0 & 0 \\ 0 & 0 & 0 \end{vmatrix} \\ \begin{vmatrix} c_{11} & c_{12} & c_{13} \\ c_{21} & c_{22} & c_{23} \\ c_{31} & c_{32} & c_{33} \end{vmatrix}_{31} & \begin{vmatrix} c_{11} & c_{12} & c_{13} \\ c_{21} & c_{22} & c_{23} \\ c_{31} & c_{32} & c_{33} \end{vmatrix}_{32} & \begin{vmatrix} c_{11} & c_{12} & c_{13} \\ c_{21} & c_{22} & c_{23} \\ c_{31} & c_{32} & c_{33} \end{vmatrix}_{33} & \begin{vmatrix} 0 & 0 & 0 \\ 0 & 0 & 0 \\ 0 & 0 & 0 \end{vmatrix} \\ \begin{vmatrix} c_{11} & c_{12} & c_{13} \\ c_{21} & c_{22} & c_{23} \\ c_{31} & c_{32} & c_{33} \end{vmatrix}_{41} & \begin{vmatrix} c_{11} & c_{12} & c_{13} \\ c_{21} & c_{22} & c_{23} \\ c_{31} & c_{32} & c_{33} \end{vmatrix}_{42} & \begin{vmatrix} c_{11} & c_{12} & c_{13} \\ c_{21} & c_{22} & c_{23} \\ c_{31} & c_{32} & c_{33} \end{vmatrix}_{43} & \begin{vmatrix} c_{11} & c_{12} & c_{13} \\ c_{21} & c_{22} & c_{23} \\ c_{31} & c_{32} & c_{33} \end{vmatrix}_{44} \end{bmatrix}^{-1} \begin{bmatrix} \begin{vmatrix} \epsilon_1 \\ \epsilon_2 \\ \epsilon_3 \end{vmatrix}_1 \\ \begin{vmatrix} \epsilon_1 \\ \epsilon_2 \\ \epsilon_3 \end{vmatrix}_2 \\ \begin{vmatrix} \epsilon_1 \\ \epsilon_2 \\ \epsilon_3 \end{vmatrix}_3 \\ \begin{vmatrix} \epsilon_1 \\ \epsilon_2 \\ \epsilon_3 \end{vmatrix}_4 \end{bmatrix} \tag{3.17}$$

3.2. Classical Laminate Theory

Composites lamination induces residual stresses within the layers due to the variation in th CTE of the layers during consolidation. Calculation of the macro-stresses is accomplished by assuming linear elasticity and plane stress for each layer, therefore, the out-of-plane stresses are negligible with respect to the in-plane stresses [8]. The stress strain relation in matrix form (3.18) is valid for orthotropic plies under plane stress, where the reduced stiffness matrix (Q) relies on basic ply properties, such as the longitudinal Young's modulus (E_L), transverse modulus (E_T), shear modulus (G_{LT}), and the major Poisson's ratio (ν_{LT}).

$$\begin{Bmatrix} \sigma_x \\ \sigma_y \\ \tau_{xy} \end{Bmatrix} = \begin{bmatrix} \frac{E_L}{(1-\nu_{LT}\nu_{TL})} & \frac{\nu_{LT}E_T}{(1-\nu_{LT}\nu_{TL})} & 0 \\ \frac{\nu_{LT}E_T}{(1-\nu_{LT}\nu_{TL})} & \frac{E_T}{(1-\nu_{LT}\nu_{TL})} & 0 \\ 0 & 0 & G_{LT} \end{bmatrix} \begin{Bmatrix} \epsilon_x \\ \epsilon_y \\ \gamma_{xy} \end{Bmatrix} \tag{3.18}$$

The matrix form (3.18) coincides with the principle directions of the material direction. Therefore, obtaining the stiffness matrix in any ply orientation (θ) is done through tensor transformations as follows:

$$\begin{Bmatrix} \sigma_1 \\ \sigma_2 \\ \tau_{12} \end{Bmatrix} = \begin{bmatrix} m^2 & n^2 & 2mn \\ n^2 & m^2 & -2mn \\ -mn & mn & m^2-n^2 \end{bmatrix} \begin{bmatrix} \frac{E_L}{(1-\nu_{LT}\nu_{TL})} & \frac{\nu_{LT}E_T}{(1-\nu_{LT}\nu_{TL})} & 0 \\ \frac{\nu_{LT}E_T}{(1-\nu_{LT}\nu_{TL})} & \frac{E_T}{(1-\nu_{LT}\nu_{TL})} & 0 \\ 0 & 0 & G_{LT} \end{bmatrix} \begin{Bmatrix} \epsilon_1 \\ \epsilon_2 \\ \gamma_{12} \end{Bmatrix} \tag{3.19}$$

Where $m = \cos\theta$ and $n = \sin\theta$.

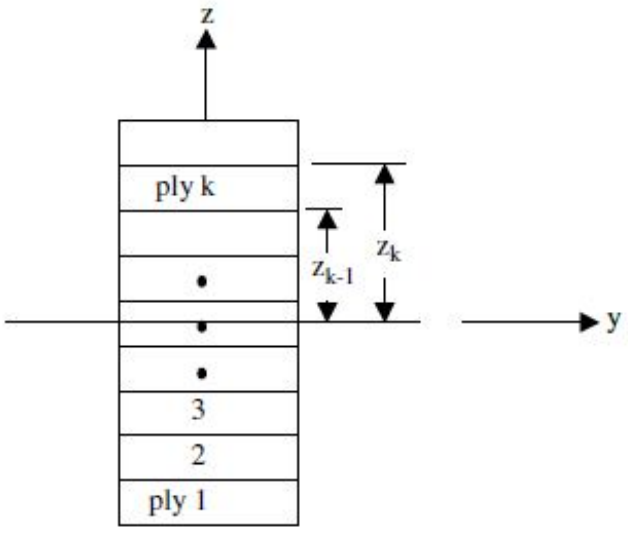

Figure 3.11: Presentation of the step-wise configuration of the coefficients [17].

Relating the external forces and moments to the stresses and strains is done to account for the thermal changes or any external load applied on the laminate. The forces are defined by integrating through the thickness of the laminate (Figure 3.11), and are conveniently expressed as summations over the plies eqaution (3.20), since the stiffness coefficients within each ply throughout the ply thickness is constant.

$$\begin{Bmatrix} N_x \\ N_y \\ N_{xy} \end{Bmatrix} = \begin{bmatrix} A_{11} & A_{12} & A_{16} \\ A_{12} & A_{22} & A_{26} \\ A_{16} & A_{26} & A_{66} \end{bmatrix} \begin{Bmatrix} \epsilon_x \\ \epsilon_y \\ \gamma_{xy} \end{Bmatrix} \tag{3.20}$$

Where

$$A_{ij} = \sum_{k=1}^{n} Q_{ij}(z_k - z_{k-1}) \tag{3.21}$$

Where A_{ij} is the extensional stiffness matrix i, j are the standard material directions, n is the total number of plies and z_k is the coordinate of the kth ply, as shown in Figure 3.11. The same calculation method applies to the moments; a collection of the terms and their interactions in matrix form is presented in equation (3.22).

$$\begin{Bmatrix} N_x \\ N_y \\ N_{xy} \\ M_x \\ M_y \\ M_{xy} \end{Bmatrix} = \begin{bmatrix} A_{11} & A_{12} & A_{16} & B_{11} & B_{12} & B_{16} \\ A_{12} & A_{22} & A_{26} & B_{12} & B_{22} & B_{26} \\ A_{16} & A_{26} & A_{66} & B_{16} & B_{26} & B_{66} \\ B_{11} & B_{12} & B_{16} & D_{11} & D_{12} & D_{16} \\ B_{12} & B_{22} & B_{26} & D_{12} & D_{22} & D_{26} \\ B_{16} & B_{26} & B_{66} & D_{16} & D_{26} & D_{66} \end{bmatrix} \begin{Bmatrix} \epsilon_x \\ \epsilon_y \\ \gamma_{xy} \\ \kappa_x \\ \kappa_y \\ \kappa_{xy} \end{Bmatrix} \tag{3.22}$$

Where

$$B_{ij} = \sum_{k=1}^{n} Q_{ij}(z_k^2 - z_{k-1}^2) \qquad D_{ij} = \sum_{k=1}^{n} Q_{ij}(z_k^3 - z_{k-1}^3) \tag{3.23}$$

B_{ij}, D_{ij} are the coupling and bending stiffness matrices respectively. The ABD matrix in equation (3.22) provides the link between the mid-plane strains ϵ° and curvatures κ. to the applied loads and moments as shown in equation (3.25). The matrix directly depends on the material properties and layup of the laminate. It is also important to note that in this study, the applied loads are thermal (N^T, M^T) resultants that are determined using equation (3.24) and substituted into the subsequent equation (3.25) providing the mechanical mid-plane strains and curvatures. Rewriting the equation provides:

$$N_i^T = \sum_{k=1}^{n} Q_{ij}^{(k)} \alpha_j^{(k)} \Delta T \qquad M_i^T = \sum_{k=1}^{n} Q_{ij}^{(k)} \alpha_j^{(k)} \Delta T \tag{3.24}$$

$$\begin{Bmatrix} \epsilon^\circ \\ \kappa \end{Bmatrix}_{mid-plane} = \begin{bmatrix} A & B \\ B & D \end{bmatrix}^{-1} \begin{Bmatrix} N \\ M \end{Bmatrix} \tag{3.25}$$

Where ΔT is the temperature difference and α is the vector of thermal expansion coefficients in the ply x-y system. Using the equation (3.26) to determine the ply strains in the x, y coordinate system;

$$\begin{Bmatrix} \epsilon_{xx} \\ \epsilon_{yy} \\ \gamma_{xy} \end{Bmatrix}_{Net}^{k} = \begin{Bmatrix} \epsilon_{xx} \\ \epsilon_{yy} \\ \gamma_{xy} \end{Bmatrix}^{\circ} + z \begin{Bmatrix} \kappa_{xx} \\ \kappa_{yy} \\ \kappa_{xy} \end{Bmatrix} \tag{3.26}$$

A second contribution of the induced strains within the laminate due to temperature change is the thermal strain created by free expansions or contractions of the material. In this case, the thermal strain vector $\epsilon_T^{(k)}$ is calculated using the following equation:

$$\{\epsilon\}_{Thermal}^{k} = \{\alpha\}_{Thermal}^{k} \Delta T = \begin{bmatrix} m^2 & n^2 & -mn \\ n^2 & m^2 & mn \\ 2mn & -2mn & (m^2 - n^2) \end{bmatrix}^{k} \begin{Bmatrix} \alpha_x \\ \alpha_y \\ \alpha_{xy} \end{Bmatrix}_{Thermal}^{k} \Delta T \tag{3.27}$$

Finally, the residual strain vector is calculated as the difference between the mechanical and thermal strains. It then becomes relatively simple to obtain the residual stresses using the stress-strain relation (3.29). The steps taken in CLT are presented in a flowchart in Figure 3.12.

$$\{\epsilon\}_{Residual-Strain}^{k} = \{\epsilon\}_{Net}^{k} - \{\epsilon\}_{Thermal}^{k} \tag{3.28}$$

$$\{\sigma\}_{Residual-Stress}^{k} = [Q_{ij}]^{k} \{\epsilon\}_{Residual-Strain}^{k} \tag{3.29}$$

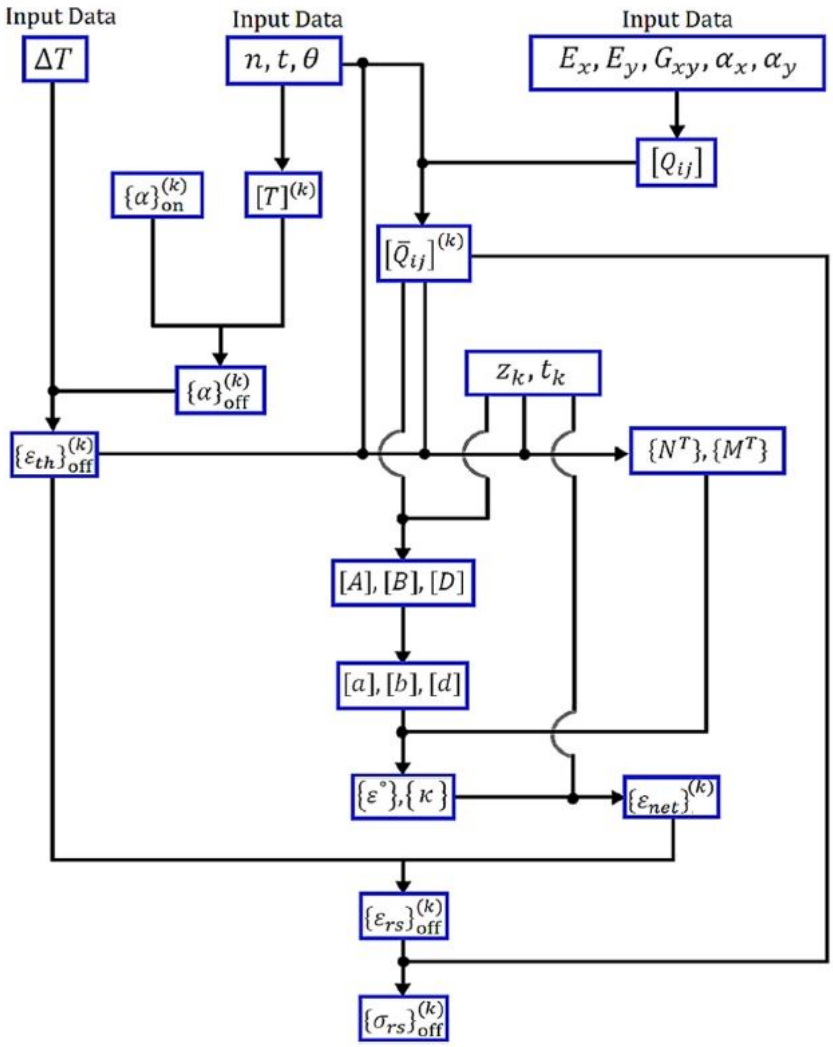

Figure 3.12: Presentation of the procedure flowchart [17].

4

Experimental

In this chapter, the experimental part of the study is described, in which the primary goal was to establish a method to measure residual stresses using the equipment available at the Technical University of Delft. Therefore, multiple experimental runs were conducted to examine the proper approach for hole-drilling. Besides the assessments carried out by outsourced parties such as Stresstech and Coventry College, this effort was accomplished to ensure the continuation of the project unhindered by any lack of equipment or expertise. The chapter begins with a description of the materials involved and their manufacturing steps. Then the conventional equipment and preparation techniques according to the ASTM E837-13 standard are presented. The standard is a guidance tool for experiments at the faculty workshop. In the chapter's conclusion, the assessments performed by the partners are analyzed.

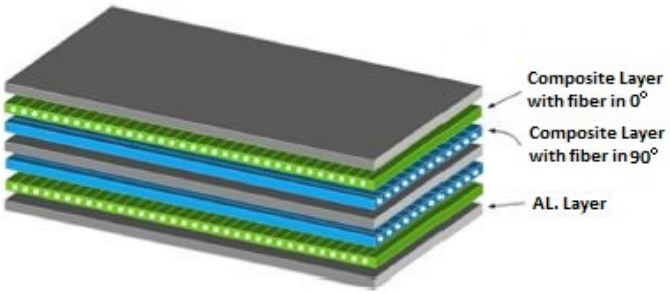

Figure 4.1: GLARE 3 structure with a stacking sequence $[AL/0/90/\bar{AL}]_s$.

4.1. Material

The project proposal was to produce multiple types of laminates including isotropic, orthotropic and hybrid laminates, evaluate their residual strains, build the associated numerical models and compare the reliability and efficiency of the measurement method for all variations. However, this was relatively ambitious given the time frame available for this master's thesis. It was decided to focus the efforts on a single type of material while varying the layup structure of its constituents. GLARE was preferred mainly for its hybrid nature, which combines the best features of both worlds, and it had the most interest among the parties involved. GLARE consists of alternating aluminum and unidirectional glass S2-fibers merged together using epoxy adhesive FM-94 [2]. Figure 4.1 introduces an example of the GLARE-3 structure $[AL/0/90/\bar{AL}]_s$ used in the study. The other FML structures used are $[AL/0]_s$ and $[AL/0/90/0/\bar{AL}]_s$, which are classified as GLARE 1 and GLARE 4A laminates. Table 5.2 illustrates the mechanical properties of the aluminum sheets and the glass-fiber composite as determined by a prior study [2]. The thicknesses of the S2 glass/epoxy and aluminum layers are 0.127 mm and 0.4 mm respectively. A square shape geometry is kept constant for all produced laminates, but with varying side lengths.

Table 4.1: Material properties of GLARE constituents used in the experimental and numerical study.

Mat.	$E_1[GPa]$	$E_2[GPa]$	$G_{12}[GPa]$	ν_{xy}	$\alpha_x(\mu/C^\circ)$	$\alpha_y(\mu/C^\circ)$
S2 Glass Fiber	52 .0	7.4	3.0	0.33	4.1	48.6
Aluminum	72.4	72.4	27.6	0.33	22	22

4.2. Manufacturing

GLARE was discovered through the efforts of researchers at the Technical University of Delft in cooperation with partners such as Fokker, then AkzoNobel. Therefore, GLARE manufacturing at this department is performed with highly experienced staff and is well established. The steps taken to produce a GLARE laminate are explained in this section. Three different batches were manufactured for this study; the first was designed to be 300 mm by 300 mm plates with the layup as follows $[AL/0/90/\bar{AL}]_s$. The first laminates were used for initial evaluation of the strain-acquisition and hole-drilling systems. The second batch was manufactured to be sent to the partners involved in the study for comparative hole-drilling tests. The dimensions of the plate were altered to 460 mm by 460 mm, which is the original width of the aluminum roll obtained from Fokker.

The third batch was also square laminates, but with a side length of 230 mm; the dimensions were halved to conserve material. This batch was used after a proper setup was acquired based on the first round of experiments. The second and third batches included the three layups stated above. Figure 4.2 depicts the Darley cutting machine used to cut the aluminum plates into the desired shape and dimensions. Afterwards, a simple clean surface was the only tooling required to initiate the stacking of the laminates.

Figure 4.2: The Darley machine used for cutting the aluminum into the desired shape and dimensions.

The prepreg material, which had been stored in a freezer was taken out and left in a clean environment for at least 24 hours to allow it to reach room temperature slowly in its original packing. This prevented from moisture condensation and to facilitate further easy processing [11]. Once the prepreg material reached acquired temperature, it was cut and stacked according to the required laminate and orientation within a clean room (Figure 4.3). The importance of the clean room lay in mitigation of any resident contaminants or voids, in addition, cleaning the surface of aluminum sheets using acetone or ethanol prior to layup was beneficial for the same reason. Usually the cutting process is automated for large production lines, but for this study, it was convenient to use a ruler and a utility knife.

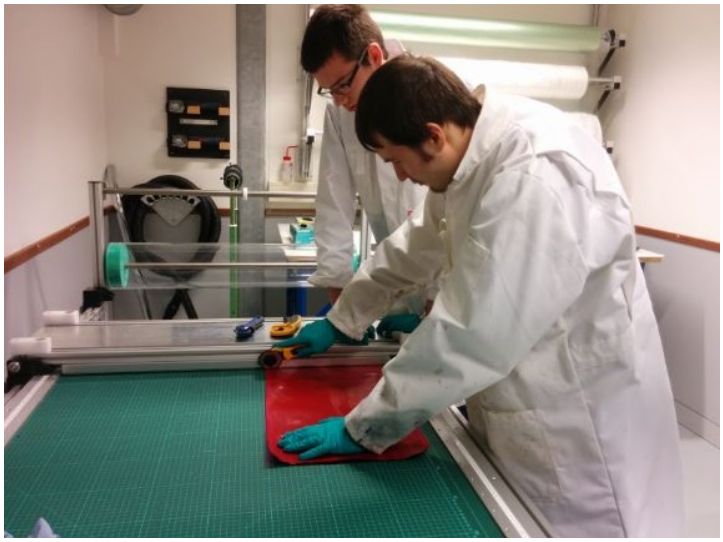

Figure 4.3: The clean room used for stacking the GLARE laminates.

Stacking was performed according to the desired configuration, with the rolling direction of the aluminum sheets used as reference for the 0° direction of the glass fiber. Note that the aluminum and prepreg sheets tend to curve due to storing them as a roll; therefore the surface of the sheets was flipped once the midpoint of stacking sequence was reached. Afterwards, the stacked laminates were placed on a flat tool for consolidation. Curing, or consolidation, of the laminates was commuted in the autoclave (Figure 4.4).

Figure 4.4: The autoclave used for part consolidation, with controlled temperature (T) and pressure (P).

Prior to consolidation, a release agent was applied to the tool surface to ensure the part would be released after curing. In addition, the laminates were vacuum bagged. The steps required to prepare a vacuum bag are stated as follows, from the bottom (tool surface) to the top:

1. Covering the tool surface with peel ply to ensure separation of the laminates and to protect the tool for future uses.
2. Applying a bleeder, a porous fabric that absorbs excess resin and allows the entrapped air or moisture to escape. Then, placement of the laminates on top of the bleeder.
3. Applying a second layer of the porous fabric a breather, which allows the entrapped air and void to escape. Its main function is to creating even pressure on top and around the laminates.

4. Finally, a polyamide (PA) film is applied, which is expandable to allow some deformation for the vacuum bag.

Once the vacuum bag was sealed using tacky tape and no leakage was found, the laminates were ready for consolidation in the autoclave. A standard cure cycle (Figure 4.5) was used for the GLARE plates, with 6 bar pressure and 120° Celsius for 1 h, with heating and cooling rates of 2.5° Celsius per minute. In addition, the vacuum pressure was maintained at 1 bar. After Consolidating, the laminates were removed from the tool and the edges were trimmed for better handling during the experimental testing. Figure 4.6 illustrates a manufactured part ready for testing.

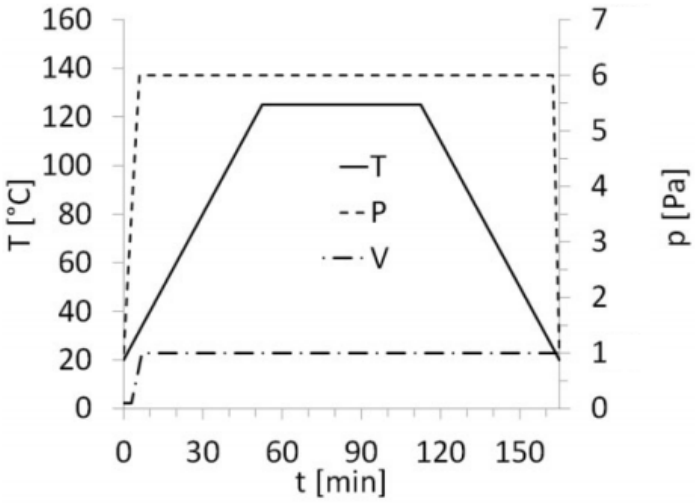

Figure 4.5: Standard cure cycle for the manufacture of GLARE with temperature (T), autoclave pressure (P) and vacuum-bag pressure (V).

Figure 4.6: A standard GLARE laminate with a 300 mm side length.

4.3. Hole-drilling Procedure

In this section, the proper measuring techniques and equipment are illustrated, ranging from surface preparation, strain-gauge installation, strain-data acquisition systems and the drilling machine. First, appropriate surface treatment is essential to prevent poor gauge bonding and inaccuracies of the result. It is recommended within the ASTM standard E837-13 to clean and degrease the surface first to produce a smooth surface, and avoid mechanical roughening of the surface in order not to induce any surface residual stresses. Accurate alignment of the lines for strain-gauge positioning is crucial, because the directional elastic moduli is directly proportional to the orientation of the gauge rosette with regard to the rolling direction of the aluminum, which is also the 0° direction of the oriented fibers [17]. Finally, appliance of the adhesive should be minimal but still sufficient for good adhesion. This is important to avoid variations between the specimen surface strains and the measured strains.

The strain-monitoring instruments must have strain resolution, stability and repeatability of $\pm 2x10^{-6}$[4]. In addition, the lead wire must be short as possible to minimize lead-wire resistance [17]. Continuous strain measurements by the data acquisition systems are preferred because the strain variations will include those caused by drilling as well as by thermal changes. Analyzing continuous strain measurements helps define the settling time required for the strain response to stabilize before recording them.

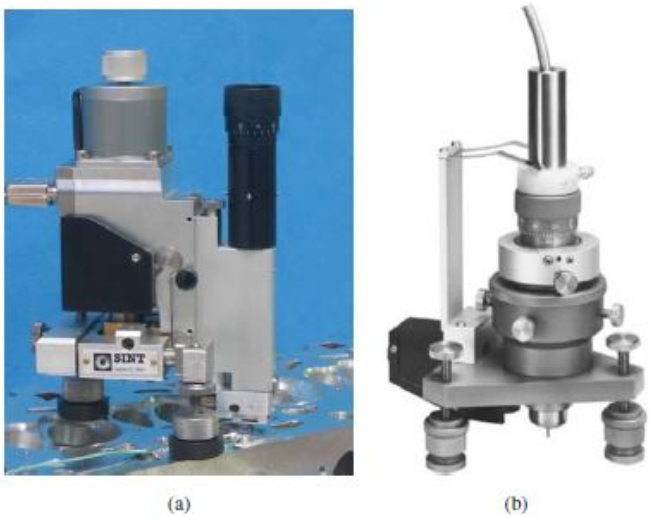

Figure 4.7: Hole-drilling machines, (a) SINT MTS3000 and (b) Micro-Measurements RS-200 [17].

The vital requirement of the hole-drilling machine is to drill the hole exactly at the center of the rosette; the accuracy must be within $\pm 0.004D$. In other words, it is required to be within ±0.00205 mm for the 5.13 mm type A rosette used in this study. Figure 4.7 illustrates two typical examples of hole-drilling machines used specially for hole drilling, each with different advantages and limitations [17].Care is required when choosing the type and shape of the drill tip according to the standard ASTM E837-13 [4]. Usually a flat or slightly concave drill head is favored, such as a cutter with 5° relief on each side [17]. The importance of this resides in the assumption that the hole has a flat end, which is also the case simulated in the finite element model. Variations in the hole geometry would naturally cause the results to deviate.

Incremental hole-drilling procedure is summarized as follows:

1. The procedure is initiated by attaching the strain gauge properly and checking the quality of the installation, then the connection to the data-acquisition box is done and checked for open loop.

2. The drill bit is aligned with the center of the strain rosette, usually using a microscope, and the specimen surface is calibrated as the zero depth level prior to drilling.

3. The first depth or increment step is drilled with high orbital speeds but at a very low feed rate to minimize the induction of any thermal gradients that could alter the strain measurements.

4. Once the increment depth is reached, the drill tool is withdrawn from the material and the drill is turned off. Afterwards, the strain acquisition box is monitored until the strain response stabilizes, indicating the true strain to be recorded. The true strain is the measured strain from drilling the increment with no effects from temperature gradients. From this, the correct settling time of the signal is identified and used as a standard in the increments to follow.

5. Then the remaining increments are drilled, and the strain recordings are continued as specified. Careful examination of the hole and the strain-gauge rosette after the drilling process is essential for assessing the hole-drilling performance. In addition, analyzing such data can provide useful information for adjusting the experimental setup for future runs.

4.3.1. Experimental Runs

Initially it seems that no suitable equipment is available for reliable hole drilling within the department. However, the literature provides alternatives to conventional hole-drilling machines. Inherently a new setup or procedure requires extensive verification and adaption of the process since no prior experience is available. The hole-drilling process for this experiment was built upon multiple runs, which are discussed in more detail in this section.

First Run. Simple through-hole analysis was used with different materials to provide an estimate of the magnitude of the possible strains to be measured during testing. The drilling was performed using the hand drill in Figure 4.8a, and the strain monitoring was performed using a Keithley model 2701 shown in Figure 4.8b, which is a high performance multimeter/data acquisition system, capable of measuring both AC and DC voltages and currents, resistances, temperature, frequency and continuity. Therefore, the system is considered very versatile and expensive. The key feature of the model 2701 is that it provides an Ethernet interface, with free software Excel.INX-1A (Figure 4.9) already embedded in the system.

(a) Conventional hand drilling machine.

(b) Keithley model 2701, numerically controlled.

Figure 4.8: Equipment used in the first round of experiments at the faculty of Aerospace Engineering. (a) Hand drilling machine, (b) Keithley strain-acquisition box.

The Microsoft add-in utility is an interface for exporting the acquired strain data directly and converting it into useful information, thus simplifying data analysis. Using the key feature, the first-run results are presented in Figure 4.11. Note that the strain values should not be taken as a basis for stress calculations. This is because normal directional strain gauges were used, as shown in Figure 4.10 and not the special strain rosettes used for hole drilling. Although the strain gauges were carefully placed according to the required angle orientations and dimensions under a microscope, it was difficult to reach the required accuracy. Therefore, the charts are useful only for studying the strain behavior and for initial assessment of the equipment.

ExceLINX KEITHLEY A Greater Measure of Confidence

Task: Configure Scanning DMM Channels

Task	Name	DMM Config
	Description	
	Created By	Metingen Keithley
	Company	TU Delft
	Date Created	1/27/2016
	Date Modified	7/13/2017
	Status/Cmds	Task stopped successfully
Instrument	Device	MODEL_2701_at_TCPIP_192.168.
	Model	M2701
	Password	
	Slot 1 Module	M7708*
	Slot 2 Module	Empty*
	Slot 3 Module	
	Slot 4 Module	
	Slot 5 Module	
	Front Panel Lockout	On
Setup	Line Sync	Off
	Autozero	On
	Display Digits	6½
	DCV Input Divider	Off
	Open TC Detection	Off
	Temp Scale	°C
Limits	Digital Outputs	Off
	Pulse Output	Off
	Polarity	High
	Duration	0.02 sec
	Master Latch	Off

Channel Scan List

Channel	Measurement	Scaling	Alarm Limits	Rep Filter	Sampling	Options

Figure 4.9: Excel.INX-1A, a utility add-in used to export the Keithley's response into useful information presented in Excel form.

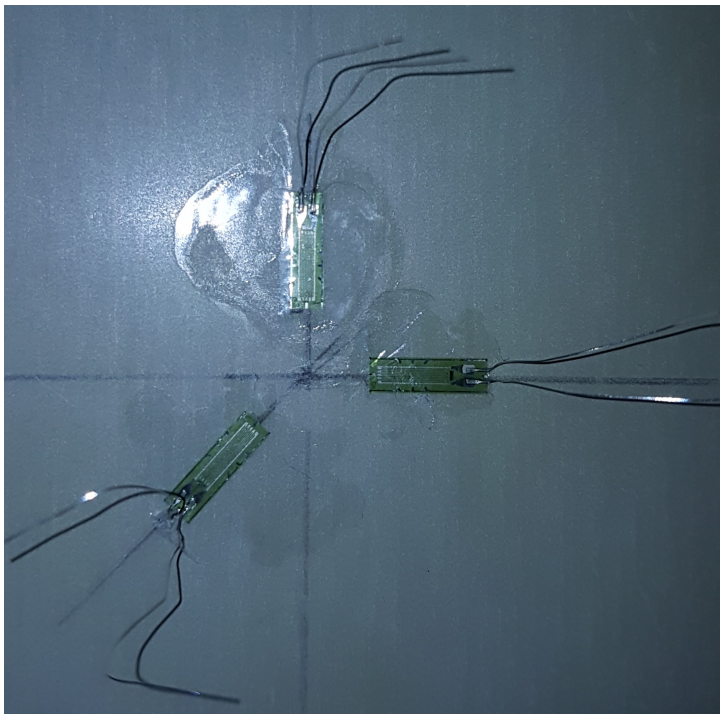

Figure 4.10: The type and positioning of the normal strain gauges for the 1st run of experiments.

The experimental results shown in Figure 4.11, illustrate the behavior of the stress response during the drilling of a GLARE laminate in four steps. The minimum peaks represent the drilling moments of the part. Once the drilling action was halted, the strain response stabilized until a second drilling phase was begun. It was deduced that the larger the drill, the more strain is released since more material is removed from the laminate. Finally, this experimental run was highly beneficial in gaining experience with handling of the strain-monitoring equipment, strain-gauge installation and surface preparation.

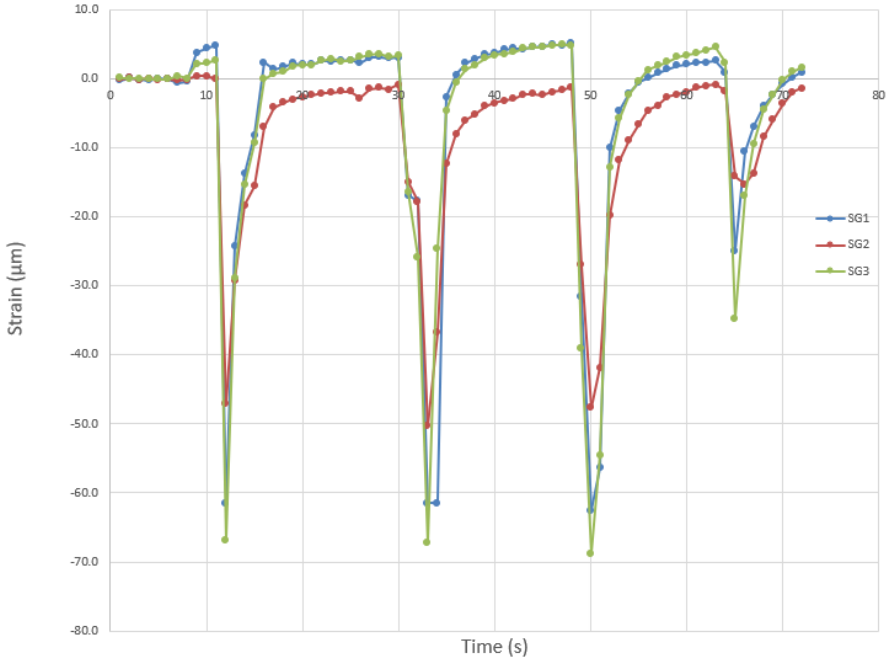

Figure 4.11: The strain response recorded by the Keithley for the first run of experiments.

Second Run. After the first run, it was decided to use a CNC milling machine in order to control the depth of each increment, accurate alignment of the drill bit and the feed rate, and to apply high orbiting speeds. The depth, orbiting speed and feed rate are controlled through numerical inputs by the technician, and the settling time between the drilling increments is defined within the control interface. The alignment of the drill bit with the rosette center is performed prior to drilling using a microscope to ensure the accuracy required by the standard. Additionally, the zero level (z-axis coordinate of the CNC) is defined at the surface of the material by slowly lowering the drill with an edge finder containing a soft probe at the end. Once the location and level of the hole are acquired, the numerical program is started. It follows quite simple steps:

1. Lower the drill to z = -0.25 mm depth level with a speed of 0.5 mm per second.
2. Lower the drill to z = 0 depth level with a speed of 10 μm per second. This basically means it drills through the strain rosette layer and reaches the specimen surface.
3. Raise the drill to z = -0.25 mm depth level with a speed of 10 μm per second and hold for the settling time.
4. Lower the drill to z = [depth level of first increment] with a speed of 10 μm per second. Once the depth level is reached, the drill is drawn back to z = 0.25 mm and hold for the settling time.
5. The incremental drilling is continued in the same manner for the remaining increments.
6. The strain measurement is continued during the whole drilling process and is analyzed afterwards for determination of the released strain per increment.

Table 4.2: The layup and ID of the GLARE laminates used in the second experimental run.

ID	Layup	Thickness [mm]
1764	AL/0/0/AL	1.054
1766.1	AL/0/90/AL/90/0/AL	1.708
1766.2	AL/0/90/AL/90/0/A	1.708
1768	AL/0/90/0/AL/0/90/0/AL	1.926

New GLARE laminates were manufactured for this round; their stacking sequence and thicknesses are presented in Table 4.2. Four laminates were made and drilled at three locations per laminate as illustrated in Figure 4.12.

Thus, a total of 12 measurement turns were conducted during this round, with two different increment sizings. The first increment sizing was based on the ASTM standard, where 11 increments are drilled to a depth of up to 0.64 mm, eight of them through only the first layer of the laminate (aluminum layer, t = 0.4 mm), and the rest through the next composite layers. This first increment sizing is named the long cycle (LC) during the study for convenience. The LC was mainly performed to provide enough incremental information to measure the residual stresses within the aluminum layer. The LC sizing is presented in Table 4.3. The laminates were fixed in place through the use of a vacuum plate ensuring the flatness of the laminate.

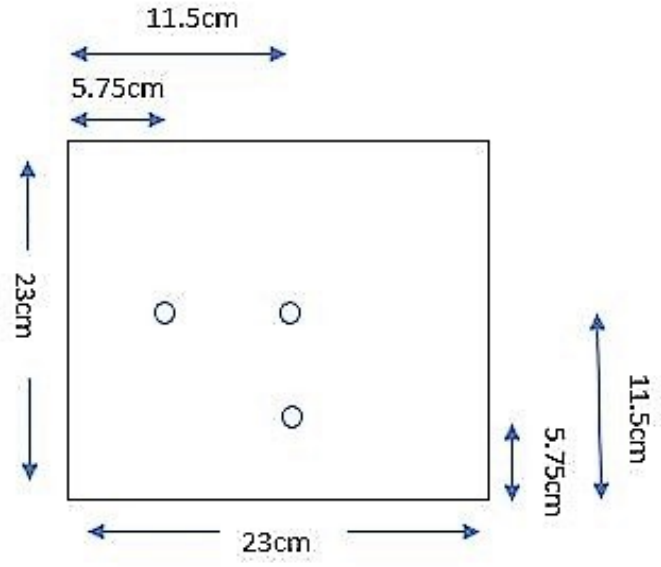

Figure 4.12: The test locations of the hole-drilling experiments.

Table 4.3: The first (LC) and second (SC) increment sizing used in the study.

Increment numbering (n)	First increment sizing (LC) depth level [μm]	Second increment sizing (SC) depth level [μm]
1	16	200
2	48	400
3	80	527
4	112	654
5	160	
6	224	
7	288	
8	352	
9	448	
10	512	
11	640	
Settling time[minutes]	1	2
TOTAL time [minutes]	20	12

The second increment sizing was performed according to the preferred incremental measurement of residual stresses through the laminate thickness to include more layers and minimize unnecessary computational power and effort. The sizing included two increments for the first aluminum layer, then one for each composite layer, concluding a total of four increments for each hole-drilling cycle. This is also called the short cycle (SC). The SC was based on previous studies showing that one increment per layer is sufficient for reliable results [22]. Moreover, it is possible to verify this by analyzing the data obtained for the LC, since multiple increments are computed to measure the stresses within the first layer. The incremental steps for both cases are presented in

Table 4.3, where the settling time and the time required for one cycle of hole drilling is also mentioned. For this round, a second data-acquisition box NI9219, was used because of it's small size and portability. From which the strain responses are exported using the LABVIEW interface available on a personal laptop that was connected to the NI instrument through a usb cable.

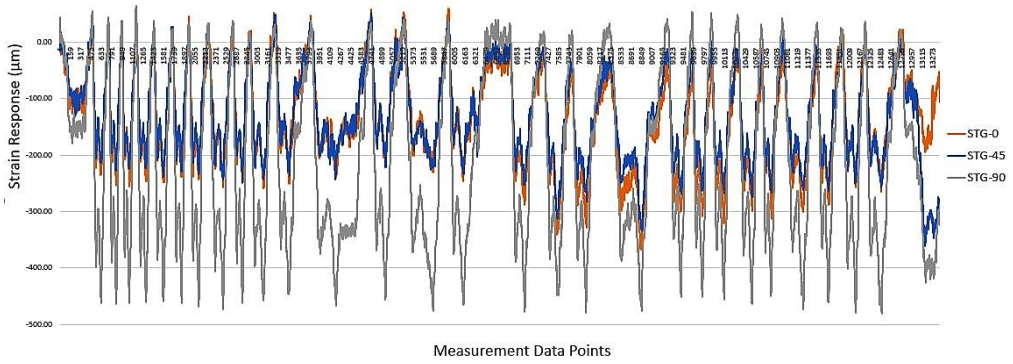

Figure 4.13: The strain responses recorded by the NI9219 for the second run of experiments using the LC.

Analyzing the second round results show high oscillations within the response signals illustrated in Figures 4.13 and 4.14 for first and second increment sizing respectively. Data range sampled from 8,000 to 14,000 data points for the SC and LC. The probable causes of the oscillations were studied prior to the commencement of the third round of hole-drilling experiments, leading to the realization that noise was introduced within the measurement system, therefore for the next run a different system was used.

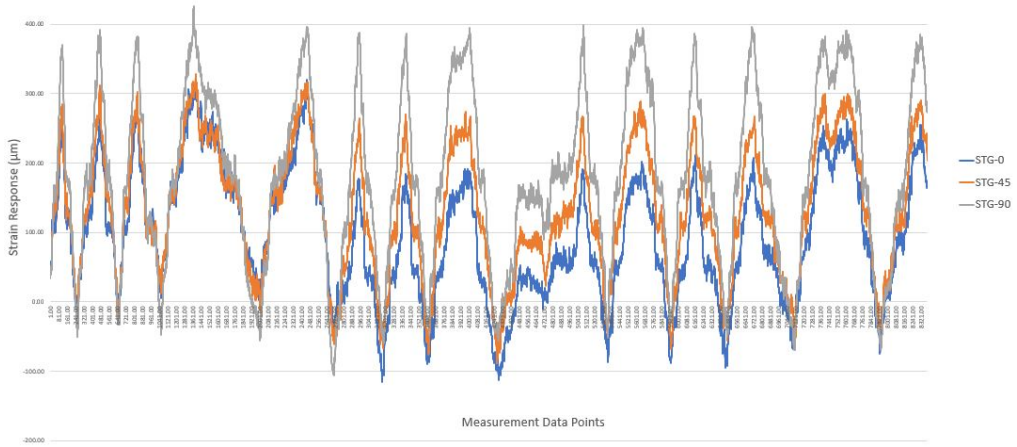

Figure 4.14: The strain responses recorded by the NI9219 for the second run of experiments using the SC.

Third Run. GLARE laminates with same stacking sequences as in the second run were used in the third, and the test variables were kept the same. The differences were that the strain-monitoring device used was the Peekel a multi channel strain-acquisition box, and the GLARE laminates were fixed using metal restraints. The lack of experience and noise amplification of the NI instrument were the main reasons for using the peekel for this round. The constraints were changed to hinder the induction of vibrations during drilling. Analyzing the data from the third run temperature fluctuations were found due to drilling at the surface of the material which were measured using a thermocouple attached on the surface of the component. This entails that the hole-drilling procedure is required to be optimized further by trying new alternatives for the equipment currently used which would be a time consuming process because of the high sensitivity of the hole-drilling process to many factors.

4.3.2. Research Partners

Experience is a major factor in the quality of measurements obtained from hole drilling. Significant errors could be induced by the operator or the equipment. More experienced and highly capable parties were requested to perform the same hole-drilling process of the laminates. Outsourcing the experimental load, to complement the work performed within the facilities, was expected to boost the success rate of this study. Two highly capable parties were involved:

Stresstech, a technical company involved in the measurement of residual stresses within components through various techniques, such as X-ray diffraction, Barkhausen noise and hole drilling.

Coventry University, an academic group in the United Kingdom with staff highly experienced in hole drilling. In addition, the group has high interest in studying the residual stresses within GLARE laminates.

Stresstech

The researchers at Stresstech performed measurements using the first batch (460 mm by 460 mm) of GLARE laminates, but the laminates were trimmed to fit within their machine perimeter. The trimmed plates were rectangular with approximately 170 mm by 100 mm side lengths, as illustrated in Figure 4.15. Moreover, the stress directions are noted as $SigXX$ for the rolling direction and $SigYY$ for the transverse direction. The depth profile of the experimental measurement was discretized according to the LC, as illustrated in Figure 4.16.

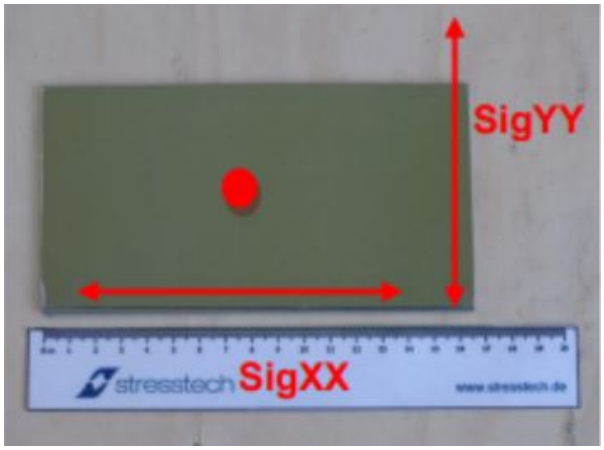

Figure 4.15: The newly fitted GLARE laminates required for testing.

The strain responses were recorded using an optical system known as PRISM, which utilizes the use of Electronic Speckle Pattern Interferometry (ESPI) with hole drilling for residual stress measurements. The main objective of using PRISM is to speed up the measurement process, by skipping the time consuming and labor intensive process of positioning and installing strain gauges on the specimen surface. The optical system measured the strain by monitoring the surface distortions through a series of images taken before and after each increment step [20]. Analyzing the pixel intensities of these images with the relations (4.1), provided a phase map ω. The released strains were then exported from the phase map using an advanced algorithm embedded within the software.

$$\begin{aligned} I_i(p,q) &= I_{ref}(p,q) + I_{obj}(p,q) + 2\cos\phi_{(p,q)}\sqrt{I_{ref}(p,q)\cdot I_{obj}(p,q)} \\ \omega &= \tan^{-1}\left[\frac{(I_1-I_3)(I_1^{'}-I_3^{'})+(I_2-I_4)(I_2^{'}-I_4^{'})}{(I_1-I_3)(I_2^{'}-I_4^{'})-(I_2-I_4)(I_1^{'}-I_3^{'})}\right] \end{aligned} \tag{4.1}$$

Afterwards, the released strains were inverted into stresses using the calibration coefficients provided by ASTM E837-13. The stresses σ_{xx}, σ_{yy} and τ_{xy} for a laminate with layup; $[AL/0]_s$ are plotted with respect to the depth profile in Figure 4.16. However, the computed stresses are not representative for the GLARE laminates because

the calibration constants used were those associated with isotropic materials. In other words, the algorithm recognizes this part as a fully isotropic structure, not as a hybrid structure. Therefore, the experimental efforts were discontinued, as the hole-drilling capabilities were limited to isotropic material. However, analyzing the behavior of the stress curves would be useful in the upcoming stages.

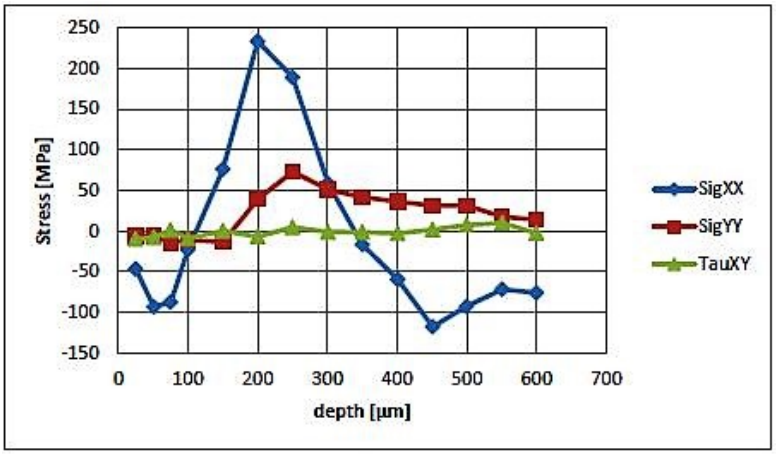

Figure 4.16: The residual stresses computed for GLARE with layup $[AL/0]_s$.

The stress curves through the depth profile obtained from the three configurations show similar behavior, with the stresses in the x-direction (rolling direction) after the first increment displaying the release of compressive stresses that transform smoothly into tensile stresses with a maximum at 0.2 mm. The peak is at the same location for all configurations, the midpoint of the aluminum layer. Afterwards, the tensile stresses decrease again until they smoothly transform into compressive stresses with the minimum at the midpoint of the composite layer (second layer). The behavior of the stresses through the thickness of each layer show that the stresses change linearly within each layer.

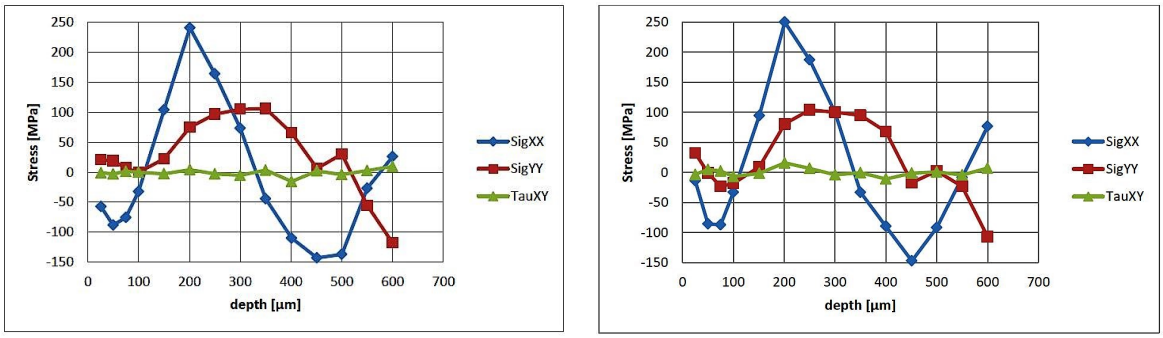

(a) $[AL/0/90/\bar{A}L]_s$ (b) $[AL/0/90/0/\bar{A}L]_s$

Figure 4.17: The residual stresses computed for GLARE with the remaining layups.

Viewing the presented plots together reveals that more stresses are released in the x-direction than the other axes. The reason is that the fibers are predominately oriented in the 0° direction which hinders the aluminum layers tendency to elongate at high temperatures (during cure) since fibers have significantly lower elongation or deformation rate, usually around 1% - 2% [8]. Furthermore, it is apparent that the stresses in the rolling direction (x-axis) increase slightly with addition of 0° directional layers. Analogously, by observing the released stresses in the y-direction in the three plots, one sees that by adding a composite layer oriented in the 90° in the second and third configurations introduces released stresses in the same direction. Finally, minimal shearing stresses are observed due to the laminates being symmetric.

Coventry University

For the second partner, experiments were conducted at the Department of Manufacturing and Materials Engineering at Coventry University, United Kingdom. The incremental hole drilling was done using the drilling devices provided by Stresscraft Ltd. The specialized hole-drilling machine is a 3-axis, numerically controlled device and is designed to perform the drilling in an orbital motion, as illustrated in Figure 4.18. Orbital drilling requires a drill bit that is much smaller than conventional cutters to drill the same hole diameter, resulting in less heat induction during the drill process. Lower temperature gradients directly affect the strain response stability in a positive manner. In addition, the machine's ability to drill harder materials increases because the wear created during the drill process is lower. While the drill motion and type of cutter were different, the incremental hole-drilling procedure, surface treatment and strain monitoring were very similar to the previous tests.

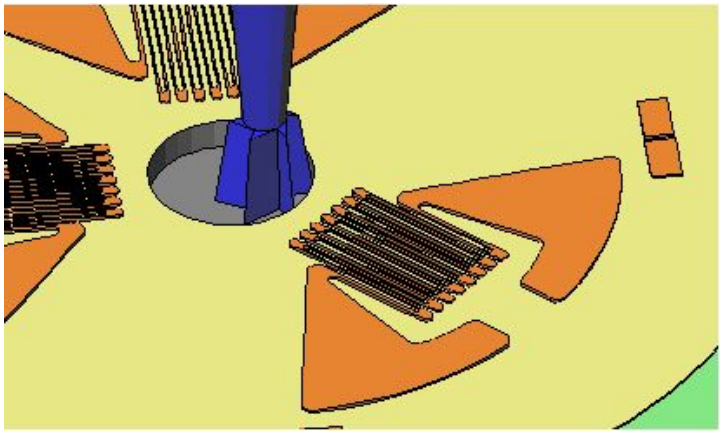

Figure 4.18: The orbital motion of hole-drilling machine for better strain response stability [26].

An experimental run was conducted by the group, and the depth profile of the run was incremented using the first sizing (LC). Similarly to the residual stresses obtained by Stresstech, the downside to the system used by Coventry University was that the strain-to-stress software is built for isotropic materials, so the computed stresses are also irrelevant to GLARE laminates. However, the strain measurements were performed using strain gauges and were recorded as presented in Table 4.4 for the LC run. These strain values are beneficial since using them together with the numerical code built for this study would provide reliable stress measurements.

Table 4.4: The strain values obtained for the LC sizing run for all GLARE configurations.

First run using LC	$[AL/0]_s$			$[AL/0/90/\bar{AL}]_s$			$[AL/0/90/0/\bar{AL}]_s$		
Depth level $[\mu m]$	$\epsilon_1[\mu\epsilon]$	$\epsilon_2[\mu\epsilon]$	$\epsilon_3[\mu\epsilon]$	$\epsilon_1[\mu\epsilon]$	$\epsilon_2[\mu\epsilon]$	$\epsilon_3[\mu\epsilon]$	$\epsilon_1[\mu\epsilon]$	$\epsilon_2[\mu\epsilon]$	$\epsilon_3[\mu\epsilon]$
16	9	12	14	9	13	14	10	9	11
48	17	22	28	16	24	28	20	18	23
80	23	29	38	19	29	36	26	23	30
112	29	30	37	17	28	35	29	22	27
160	30	7	-10	4	8	7	25	2	-7
224	23	-17	-55	-6	-17	-31	16	-21	-41
288	25	-23	-68	-14	-25	-35	6	-35	-57
352	36	-10	-52	-17	-21	-19	0	-35	-48
448	24	-5	-20	-38	-16	19	-17	-33	-25
512	11	-2	8	-23	-10	17	-3	-28	-32
640	7	5	26	-19	-5	22	-3	-23	-25

Although, LC sizing is more than sufficient to determine the residual stresses within the laminate, it is recommended for future studies to obtain a run with SC sizing. This will help to minimize wasting resources and mitigate sensitivity errors. In addition comparing the accuracy of both results would be beneficial to assess the

hypothesis of one increment being enough for each layer of the laminate. Finally, it was observed from analyzing the behavior of the stress curves computed by both partners using different equipment and approaches for the drilling procedure and strain monitoring; are of the same magnitude and show similar behavior as it is presented in Figure 4.19, the stresses in the X-axis on the left and the stresses in the Y-axis on the right. Thus, the relaxed strain values presented by the Coventry University group were used with proper confidence to compute the residual stresses within GLARE laminates.

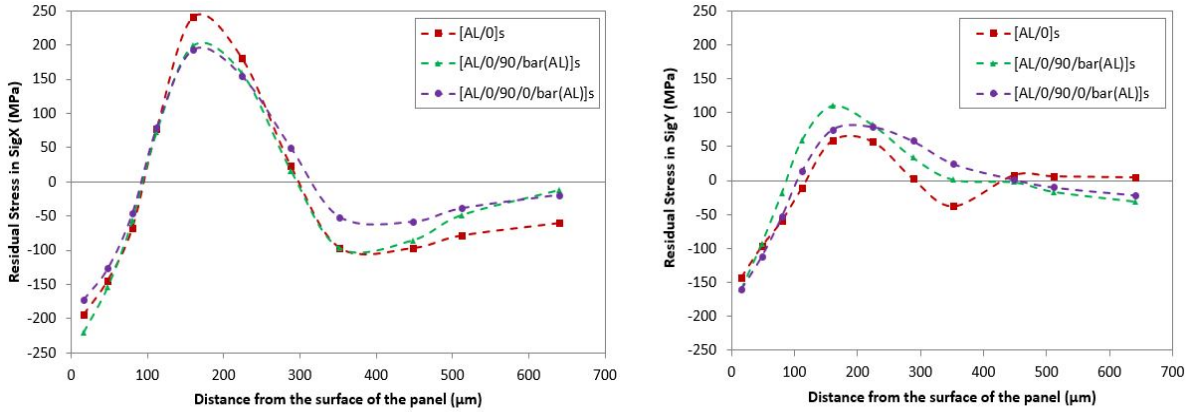

Figure 4.19: A stress comparison with respect to the magnitude and distribution between Stresstec and Coventry College.

5

Simulation

Finite element analysis was performed primarily to determine calibration coefficients relating the measured strains within a component to interior stresses. The numerical analysis was executed in an ascending order with respect to the complexity of material type and structure. First, two-dimensional (2D) plane-stress simulations of thin structures were performed, where the simulations represented a through-hole analysis (uniform stresses) of isotropic and orthotropic materials. Then, a three dimensional (3D) model of the through hole approach was built which takes the thickness of the material into account (No plane stress assumed). Afterwards, the incremental hole drilling, also known as non-uniform stress approach, was simulated for isotropic material. Finally, the simulation of the incremental hole drilling was performed for laminated components with finite thicknesses, such as GLARE.

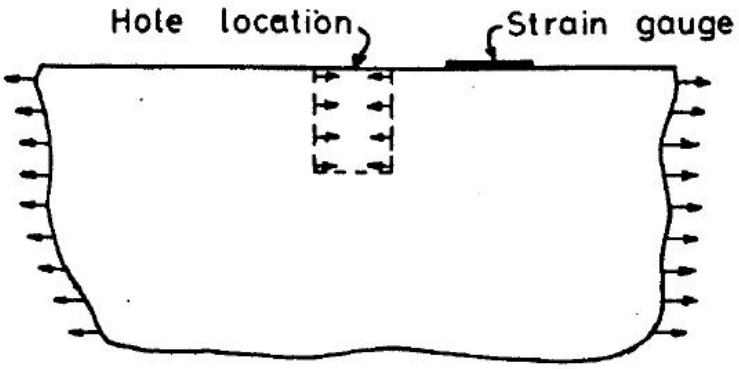

Figure 5.1: Material cross-section in equilibrium state [18].

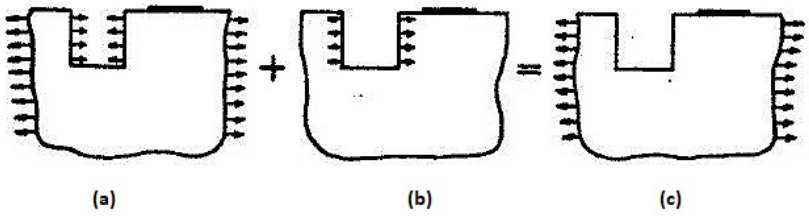

Figure 5.2: Super-positioning of the exerted loads on a component: (a) Original stresses, (b) Interior stresses residing with the hole increment, (c) Final stresses after hole drilling.

The simulation of hole drilling in different materials was executed by a finite element software package (ANSYS) [27]. The results obtained were verified with the ASTM E837-13 standard and research papers done by

G.S. Schajer. Two complementary approaches were used to simulate the hole drilling of a material, based on the superposition principle. Consider a material under loading at its boundaries, far from the intended drill location as shown in Figure 5.1. The interior stresses are in equilibrium with the stresses applied at the boundary. The equilibrium state is disturbed by the drilling of the hole, resulting in redefinition of the stress state. Figure 5.2(b) displays the stress change due to drilling in a linear elastic material, which is equal and opposite to the stresses within the hole increment at the original equilibrium state, (a). The sum is (c), which is the new equilibrium state after the hole has been drilled. In other words, figure 5.2(b) represents the redistribution of interior stresses due to hole drilling, and the associated strains are the relieved strains measured by the strain gauges [16].

Determination of the calibration constants by simulating the stress state (b) is made possible by finite element modeling, which was experimentally impracticable. Therefore, the more logical and accessible technique used by multiple researchers has been to simulate the stress states in (a) and (c), and to numerically determine the strain in both cases and the deviation in strain values between the stress states in (a) and (c), is due to the material relaxation from hole drilling. Both approaches were simulated and are referred to as stress at hole boundary (SHB) for the former and stress at edge boundary (SEB) for the latter method.

The feedback of the strain gauges was computed numerically in two ways, which provided almost identical results as follows:

1. The magnitudes of released strains for all the elements under the strain gauge area were averaged.
2. The strain integral under the strain gauge area was computed as in equation (5.1), which is basically the change in the in-plane displacement in that area divided by the side length of the strain gauge.

$$\epsilon_{StrainGauge} = \frac{1}{r_2 - r_1} \int_{r_1}^{r_2} \epsilon(r) dr = \frac{\delta_2 - \delta_1}{r_2 - r_1} \tag{5.1}$$

5.1. Uniform Stress Analysis of Thin Structures

This section covers the simulation performed for 2D thin structures (plane stress) where the hole drilled is through the thickness of the material. The SEB method is presented first, as it is experimentally possible and more common. Then the second approach, SHB, is discussed. The model capability is verified with the coefficients provided by ASTM E837-13 standard.

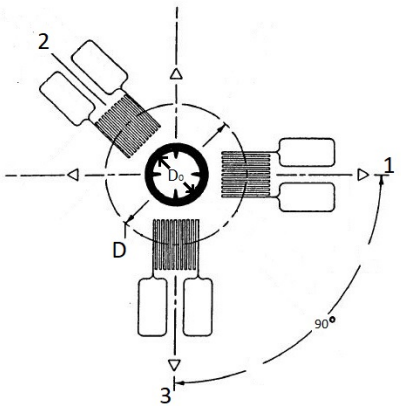

Figure 5.3: ASTM Oriented Strain gauges.

The orientation used throughout the study was as presented in Figure 5.3, where the rosette is anti-clockwise oriented with the notation 1 representing the rolling direction of the aluminum plates and the fiber direction for a unidirectional lamina oriented with 0° coinciding with global Cartesian system. The notation 3 represents the direction orthogonal to the rolling direction, coinciding with the matrix 90° direction. Finally, notation 2 represents the shearing component and is at 135° anti-clockwise from the rolling direction.

Analogously, the numerically calculated strains ϵ_1, ϵ_2, and ϵ_3 are associated with the in-plane stresses σ_x, τ_{xy}, and σ_y respectively, through equations (5.2) for isotropic and (5.4) for orthotropic materials.

5.1.1. 2D Isotropic Materials

The material used in the model was steel under plane-stress conditions, with elastic modulus 200 GPa and Poisson's ratio 0.3. The plate, hole and strain gauge dimensions were accurately simulated, noting that the hole diameterD_0 with respect to mean gauge diameter D were varied between 0.3 D to 0.5 D to compare the results with the standard. The side dimensions of the plate are 300 mm by 300 mm, the locations of the strain gauges are in a circle formation with 5.13 mm as mean gauge diameter (D), and the gauges side dimensions are 1.59x1.59 mm. These dimensions comply with the dimensions for a type A strain rosette provided in the E837-13 standard. Additionally, ($plane183$) element type was used to mesh the model, resulting in each strain gauge having 36 elements, as shown in Figure 5.4. Mesh refinement was useful to converge the obtained results when required.

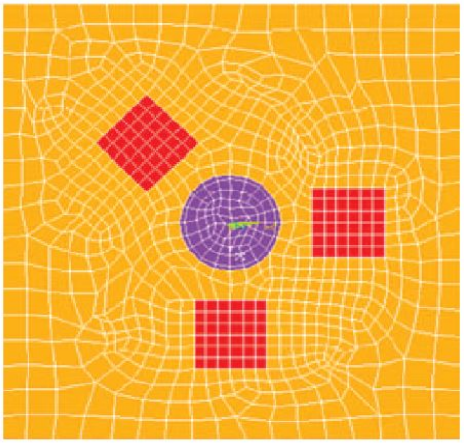

Figure 5.4: Simulation of the 2D isotropic component.

Stress at Edge Boundary. The simulation of the hole-drilling process using the SEB method was performed by applying initial stress at the edge of the plate. A uniaxial stress of 1 bar is applied, and then the elements under the hole area are removed to simulate the drilling of the hole. The removal of the elements was done by deleting or "killing" the elements within the model. The ANSYS $EKILL$ function was used, which basically multiplies the stiffness of the selected elements by a significantly low factor, the default being $1 \cdot 10^{-6}$. Furthermore, the strains were numerically determined for the stressed plate before and after introduction of the hole. The difference between the two strain responses is due to the relaxation of the surrounding material resulted from material removal through hole drilling. Figure 5.5, presents the simulation of a 2D component under uniaxial stresses at the edge.

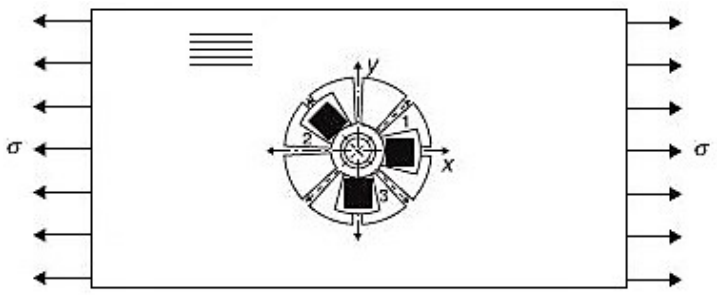

Figure 5.5: Simulation of the thin component under plane stress with uniaxial stresses at the edge boundary.

Stress at Hole Boundary. The simulation of hole drilling using the SHB approach is different from the SEB method, since the hole was not removed during the simulation but was introduced in the design of the plate geometry. Thus, a plate with a hole was designed using the exact same dimensions for the plate and strain gauges as in the previous method. Two-dimensional surf elements (surf153) were used to apply the stresses at the hole boundary, in addition to the plane elements (plane183) for simulating the plate. The stresses applied for an isotropic linear material were simplified by the trigonometric nature of the drilled hole and assumed to have a $\cos(n\theta)$ distribution as proposed by literature [18]. In previous research, it has been shown that axisymmetric loading, $n = 0$, is representative for the A coefficient (isotropic loading), whereas the B coefficient (shearing loading) corresponds to a harmonic loading with $n = 2$. Figure 5.6 presents the simulation of a 2D component under trigonometric stresses at the hole boundary. Finally, it is important to note that the SHB method is more time and computationally efficient, since the strain responses of the model are directly related to the residual stresses within the drilled hole, contrary to the SEB method where the difference between two strain responses is required to be related to the residual stress within the drilled hole.

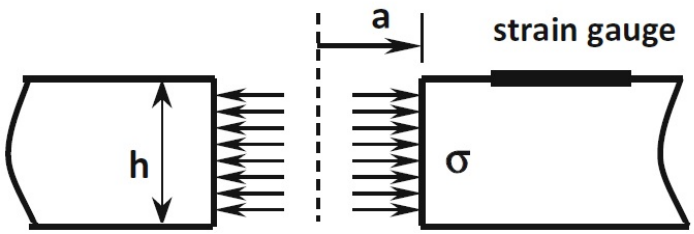

Figure 5.6: Simulation of the thin component under plane stress with stresses at the hole boundary.

Calibration Coefficients. Using the strain responses generated from simulating hole-drilling with applied stress magnitudes already known, the calibration coefficients (A and B) were calculated by using the matrix equation (5.2). Where equations (5.3) were used to make the obtained coefficients dimensionless to verify the constants with the available constants in the ASTM standard. The verification is shown in Table 5.1. Comparison of the simulation results to the standard values demonstrates that the simulations SEB and SHB are capable of determining the coefficients with a standard deviation of 2% to a maximum of 7%.

$$\begin{bmatrix} A+B & 0 & A-B \\ A & 2B & A \\ A-B & 0 & A+B \end{bmatrix} \begin{bmatrix} \sigma_x \\ \tau_{xy} \\ \sigma_y \end{bmatrix} = \begin{bmatrix} \epsilon_1 \\ \epsilon_2 \\ \epsilon_3 \end{bmatrix} \tag{5.2}$$

Where

$$A = \frac{-\bar{a}(1+\nu)}{2E} \qquad B = \frac{-\bar{b}}{2E} \tag{5.3}$$

Table 5.1: The results obtained by SEB and SHB compared with the ASTM standard.

D_0/D	Calibration Coefficients	ASTM	SEB		SHB	
			Value	Error (%)	Value	Error (%)
0.3	a	0.088	0.088	0.90	0.088	0.93
	b	0.283	0.274	3.07	0.281	0.61
0.4	a	0.157	0.157	0.41	0.157	0.52
	b	0.463	0.448	3.20	0.473	2.30
0.5	a	0.244	0.246	1.07	0.246	1.05
	b	0.642	0.620	3.40	0.687	7.00

5.1.2. 2D Orthotropic Materials

Orthotropic materials under plane-stress conditions require only four elastic moduli to express the stress-strain

relation. The elastic moduli E_x and E_y are the longitudinal and transverse moduli, G_{xy} is the in-plane shear modulus and ν_{xy} is the Poisson's ratio. The Cartesian x and y axes are the global material axes, and the orientation of the strain gauge rosette is kept the same. The use of the uniform stress analysis approach to simulate hole drilling requires the more generalized version of the matrix equation (5.2), which is written for convenience as follows:

$$\frac{1}{E_x \cdot E_y} \begin{bmatrix} c_{11} & c_{12} & c_{13} \\ c_{21} & c_{22} & c_{23} \\ c_{31} & c_{32} & c_{33} \end{bmatrix} \begin{bmatrix} \sigma_x \\ \tau_{xy} \\ \sigma_y \end{bmatrix} = \begin{bmatrix} \epsilon_1 \\ \epsilon_2 \\ \epsilon_3 \end{bmatrix} \tag{5.4}$$

The mechanical properties of glass epoxy unidirectional lamina, presented in Table 5.2, were used in this simulation. The dimensions of the plate and the location of the hole were the same as in the previous analysis. The plate was meshed using plane183 elements for both SEB and SHB calculation approaches, in addition, the surf153 elements were used in the latter approach, where stresses were applied at the hole boundary. Simulation of orthotropic material was done in the same manner as for the isotropic material, but different boundary conditions were applied. Due to the material's orthotropic nature, the elastic moduli in the x and y axes are not equal, thus the stress combinations as described in the theoretical chapter must be decoupled.

Table 5.2: Material properties of the orthotropic material used in the numerical simulation.

Material	$E_1[GPa]$	$E_2[GPa]$	$G_{12}[GPa]$	ν_{xy}
Orthotropic	200	50	40	0.25

Stress at Edge Boundary. Decoupling of the stresses was achieved by applying uniaxial stresses in each of the principle directions separately. By examining the matrix (5.2) it is clear that three separate simulations are required to compute all nine constants. The three simulations are:

Uniform stress applied at the edge of the plate in the x-axis, as given in Figure 5.5.This entails that the residual stress $\sigma = \sigma_x = 1\ MPa$, while, $\sigma_y = \tau_{xy} = 0$. The constants c_{11}, c_{21} and c_{31} are given by:

$$c_{11} = \sqrt{E_x E_y}\frac{\epsilon_1}{\sigma} \qquad c_{21} = \sqrt{E_x E_y}\frac{\epsilon_2}{\sigma} \qquad c_{31} = \sqrt{E_x E_y}\frac{\epsilon_3}{\sigma} \tag{5.5}$$

A second column of constants is computed by applying uniform shear stress at the side edges of the plate, as presented in Figure 5.7. This entails that the residual stresses $\sigma = \tau_{xy} = 1MPa$, while, $\sigma_x = \sigma_y = 0$. The constants c_{12}, c_{22} and c_{32} are given by:

$$c_{12} = \sqrt{E_x E_y}\frac{\epsilon_1}{\sigma} \qquad c_{22} = \sqrt{E_x E_y}\frac{\epsilon_2}{\sigma} \qquad c_{32} = \sqrt{E_x E_y}\frac{\epsilon_3}{\sigma} \tag{5.6}$$

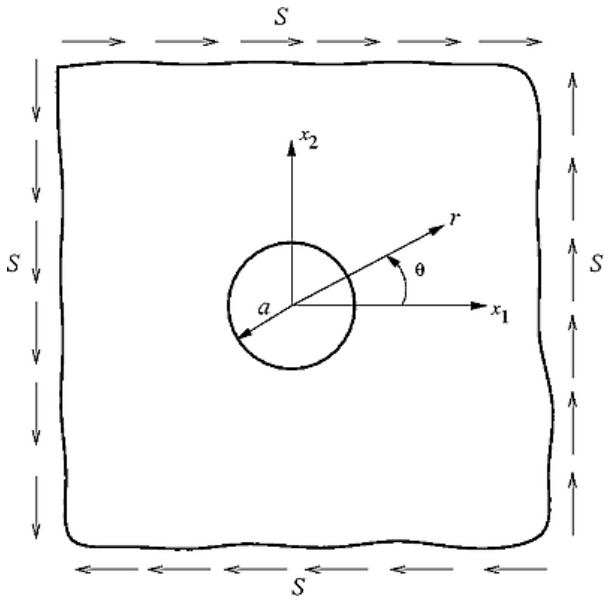

Figure 5.7: Simulation of the thin component under plane stress with applied shear stresses at the edge boundary.

The final column of constants is determined by applying uniaxial stress in the y principle axis of the plate, as presented in Figure 5.8. Thus, the residual stresses $\sigma = \sigma_y = 1MPa$, while, $\sigma_x = \tau_{xy} = 0$. The constants c_{13}, c_{23} and c_{33} are given by:

$$c_{13} = \sqrt{E_x E_y}\frac{\epsilon_1}{\sigma} \qquad c_{23} = \sqrt{E_x E_y}\frac{\epsilon_2}{\sigma} \qquad c_{33} = \sqrt{E_x E_y}\frac{\epsilon_3}{\sigma} \tag{5.7}$$

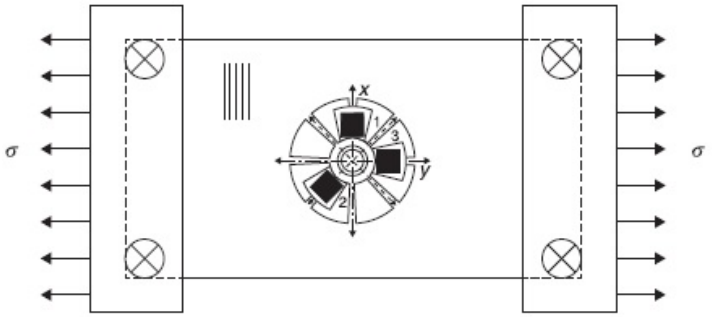

Figure 5.8: Residual uni-axial stress applied in the y global axis of the plate at the edge boundary.

Stress at Hole Boundary. As stated before, stress decoupling of the loads applied at the hole boundary is required for orthotropic materials, and therefore, the trigonometric functions are required to be decoupled. Relating the far field decoupled stress to the distortions around a hole is possible only for isotropic materials, this is due to the anisotropic nature of the orthotropic materials. Figure 5.9 shows the results of a study conducted by Dr. Gary Schajer [21], that presents the angular variation of the strain responses which varies with increasing orthotropy but coincides at 0° and 90°. Therefore, the analyses of 2D orthotropic material was conducted using SEB method, as the the trigonometric functions for SHB case provides a totally different stress state which is not equal to a uni-axial stress load, thus the results of the model could not be verified. However, it is important to note that a method proposed by Lekhnitskii's for using the trigonometric relations is available to obtain the stress responses for orthotropic materials but requires the strain measurements to be done at the hole boundary which is a different type of analysis called bore hole technique [21].

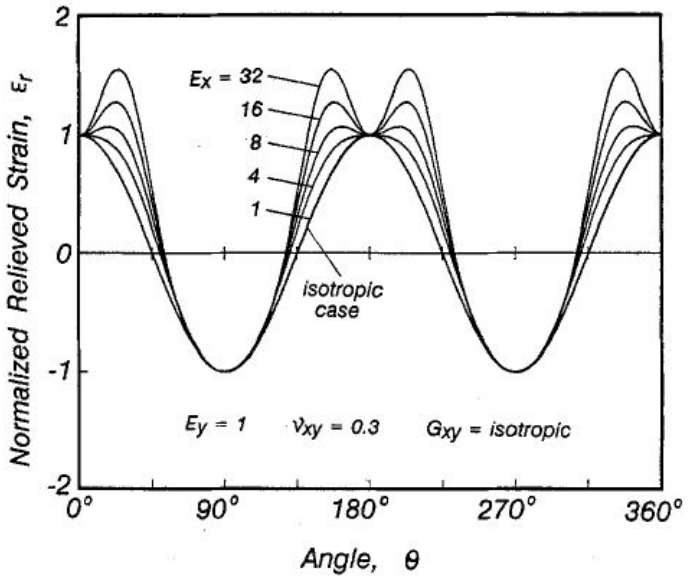

Figure 5.9: Angular variation of the stress response for orthotropic materials [21].

Calibration Coefficients. Fine agreement is found between the simulated FEM results and the theoretical results in literature, sensitivity analyses are performed for the SEB method. The variation of the coefficients with respect to the change of normal and shear moduli with a fixed Poisson's ratio is presented in Table 5.3. In addition, the sensitivity study with respect to the Poisson's ratio, with the moduli remaining constant, is shown in Table 5.4.

Table 5.3: Dimensionless constants for hole-drilling into othrotropic Materials using uniform stress analysis ($\nu_{xy} = 0.25$).

E_x/E_y	G_{xy}/E_y	C_{11}	C_{21}	C_{31}	C_{22}	C_{13}	C_{23}	C_{33}
1	0.1	- 0.559	-0.321	0.112	1.030	0.112	- 0.321	- 0.559
1	0.2	- 0.482	-0.205	0.134	0.747	0.134	- 0.205	- 0.482
1	0.3	- 0.442	-0.158	0.145	0.643	0.145	- 0.158	- 0.442
1	0.4	- 0.417	-0.132	0.152	0.572	0.152	- 0.132	- 0.417
2	0.3	- 0.379	-0.161	0.164	0.763	0.134	- 0.230	- 0.559
4	0.4	- 0.301	-0.133	0.183	0.826	0.127	- 0.286	- 0.754
8	0.3	- 0.252	-0.160	0.183	1.136	0.098	- 0.506	- 1.117

Table 5.4: Dimensionless constants for hole-drilling into othrotropic Materials using uniform stress analysis ($G_{xy}/E_y = 0.1$).

E_x/E_y	ν_{xy}	C_{11}	C_{21}	C_{31}	C_{22}	C_{13}	C_{23}	C_{33}
1	0	- 0.567	-0.300	0.159	1.115	0.159	- 0.300	- 0.567
1	0.25	- 0.559	-0.321	0.112	1.030	0.112	- 0.321	- 0.559
1	0.5	- 0.551	-0.341	0. 064	0.945	0.064	- 0.341	- 0.551
1	0.75	- 0.542	-0.361	0.016	0.860	0.016	- 0.361	- 0.542

Furthermore, the results obtained from the SEB are verified with the results presented by Schajer and Yang [21] in Table 5.5, which shows a maximum error of 8%, this error is measured using equation (5.8).

$$\%_{error} = \left| \frac{C_{SEB} - C_{Schajer}}{C_{Schajer}} \right| \cdot 100\% \tag{5.8}$$

Table 5.5: The results obtained by SEB compared with G.S. Schajer & L. Yang for othrotropic materials using through hole analysis.

Calibration Coefficients	Schajer Coefficients	SEB	
		Value	Error (%)
C_{11}	-0.285	-0.273	4.08
C_{21}	- 0.084	-0.085	1.49
C_{31}	0.206	0.198	3.80
C_{22}	0.681	0.655	3.80
C_{13}	0.157	0.145	7.07
C_{23}	-0.196	-0.190	2.99
C_{33}	-0.646	-0.631	2.9

5.1.3. 3D Simulation of Thin Structures

The uniform stress analysis of thin structures was done using 2D finite element analysis, without the involvement of any analytical approximations, and thus the simulation of thin structures using SEB or SHB in 3D offers no advantages. On the contrary, the simulation would only become larger, and a coarser mesh would be created, in addition, computational power and time would be wasted. To make this apparent, a simulation code was built in ANSYS using 3D solid elements (solid186) with the plate, hole and strain gauge dimensions were kept the same as in the 2D analysis. The diameter of the drilled hole was held constant at a value of 0.4 D, to monitor the effect of the thickness variations on the results obtained, the thicknesses used were varied between 0.1 mm, 0.5 mm and 1 mm. The simulation of 3D stresses in isotropic materials is presented in Figure 5.10.

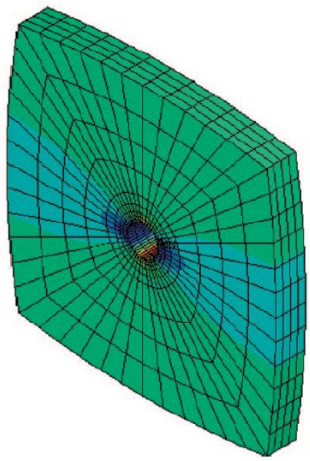

Figure 5.10: Released strain during the simulation of the 3D Isotropic component.

The hole-drilling process was simulated for this case by applying the appropriate stress functions at the edge boundary, then, the released strains were computed using the average strain under the strain gauge area. By computing the calibration coefficients and comparing it with the ASTM standard, the error range rapidly increased to a maximum of 25%, this was found for isotropic materials, which inherently would be much higher for orthotropic materials. Table 5.6, presents the computed constants a and b for the different thicknesses in 3D simulation with 2D ASTM standard.

Table 5.6: Dimensionless constants computed through simulation of hole-drilling in isotropic materials while varying the thicknesses, compared with ASTM Standard.

Thickness [mm]	Calibration Coefficients	ASTM	SEB	
			Value	Error (%)
0.1	a	0.120	0.123	2.5
	b	0.371	0.337	9.16
0.5	a	0.120	0.115	4.17
	b	0.371	0.320	13.7
1	a	0.120	0.112	6.67
	b	0.371	0.277	25.33

5.2. Incremental Hole Drilling of Thick Isotropic Structures

Incremental hole-drilling method (IHD) was introduced in literature to increase the accuracy and reliability of strain responses deep within the material, since it was illustrated that a nonuniform stress profile exists in thick and hybrid materials, as shown in Figure 5.11. The simulation and verification of this model is performed for isotropic materials. The strain rosette is placed at the surface of the material, and equal increments were drilled through the thickness gradually, which redistributed the residual stress within the material. Simulating incremental hole drilling using the SEB or the SHB approach is quite complex, since the relaxed strains from drilling incrementally were found to be not only a factor of the residual stresses applied in the same step, but is also caused by the redistribution of residual stresses of the previous steps or increments.

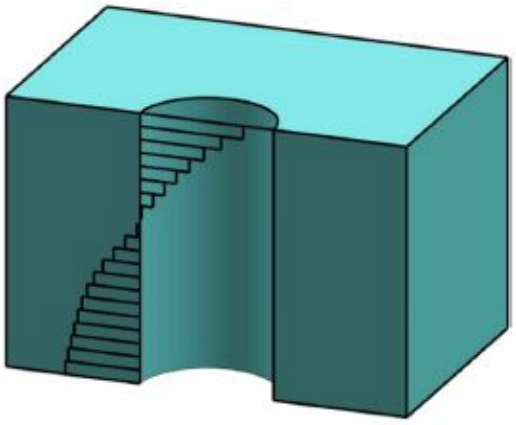

Figure 5.11: Approximation of the stress profile for Incremental hole drilling.

Stress at Hole Boundary. IHD is simulated first by using stress at hole boundary due to the fact that this is numerically simpler than using the SEB method, in addition, literature [19] is used for verification by apply the stress state of SHB. For isotropic materials, axi-symmetric and harmonic stress functions are still valid and were applied at the hole faces in order to determine the calibration coefficients for each increment. Although, the simulation process sounds similar to the simple through hole approach, it is more complex and indirect problem. The reason being the requirement to differentiate between the strain response due to; first, the released stresses at the same drill increment, second, redistribution of the previously released stresses, as presented before in the step-wise configuration (5.12) in theoretical background chapter.

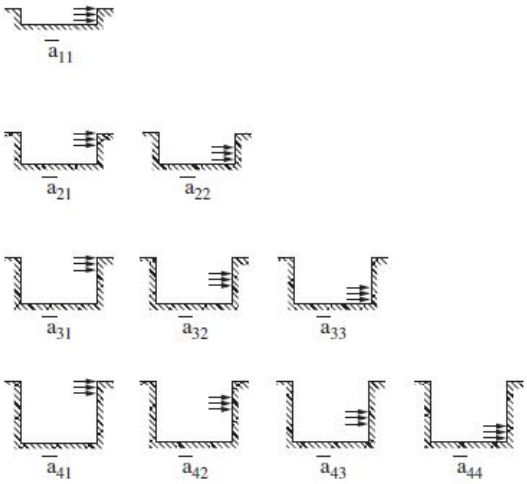

Figure 5.12: Presentation of the step-wise configuration of the coefficients [17].

Where the a_{ij} coefficients are strain relaxations to a unit stress existent within increment j, of a hole depth equal to i increments deep. It is important to understand that the strain relaxations $\epsilon(h)$ measured by the strain gauges at the surface are equal to the integral of infinitely small strain relaxations components from stress at all depth levels H till the final hole depth h is reached as shown in equation (5.9).

$$\epsilon(h) = \frac{(1+\nu)}{E} \int_0^h A(H,h)\sigma(H)dH \tag{5.9}$$

Where the term $A(H,h)$ is the strain relaxation per unit depth at by a unit stress H, when the hole depth equals h as shown in Figure 5.13 and the term $\frac{(1+\nu)}{E}$ is to express material dependence.

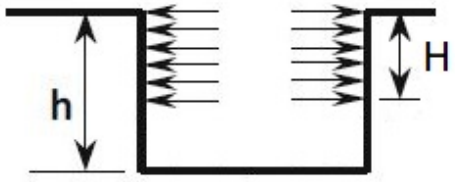

Figure 5.13: Physical presentation of the stress level H with regard to the hole depth h [19].

In practice, it is impossible to compute the infinitely small strain relaxations while increasing the hole depth gradually, as this requires infinite number of strain gauge measurement runs. However, it is possible to do a number of discrete measurements which corresponds to the discrete form used for IHD as follows:

$$\epsilon_i = \frac{(1+\nu)}{E} \sum_{j=1}^{j=i} a_{ij}\sigma_j \tag{5.10}$$

Where ϵ_i is the strain relaxation measured at the i increment, a_{ij} are strain relaxations coefficients as defined before, and σ_j is the equivalent stress within the j increment. Thus, the relation between coefficients a_{ij} and the strain relaxations A(H,h) is found as shown in equation (5.11).

$$a_{ij} = \int_{H_{j-1}}^{H_j} A(H,h)dH \tag{5.11}$$

Finally by using equation (5.11), the coefficients were determined. And using the coefficients in conjugation with the experimental strain results, a step-wise approximate solution of the stress profile with respect to depth

is found. The stress solution obtained is the equivalent uniform stress within each increment, which is not equal to the average stress within that increment due to the high sensitivity to the stresses closer to the surface [19].

In order to verify this numerical model, the output ($A(H,h)$) of the models are verified with the strain relaxations determined by G. Schajer [19] by applying axi-symmetric loading to the hole boundary, with depth variables $H = Z/r_m$ and $h = z/r_m$, z is the hole depth and Z is the depth from surface. The simulation is performed in ANSYS with 3D (solid186) elements for meshing the part and 3D surf (surf154) elements to apply the residual stresses at the hole boundary. A thick square plate was simulated, with thickness of 10 mm, side dimensions of 100 mm by 100 mm and a type A rosette with 5.13 mm gauge diameter at the center of the plate. Moreover, the increments were generated prior to the step loading of the specimen. Four equal depth increments were generated with $z = 0.1r_m$ and a hole radius $r_a = 0.4r_m$. Table 5.7 presents the verified $A(H,h)$ strain relaxations with a maximum error of 1.86%.

Table 5.7: The strain relaxations obtained from SHB compared with G.S. Schajer using Incremental hole drilling method.

Strain Relaxations	Schajer Results	SHB	
		Value	Error (%)
$A(H=0.1,h=0.1)$	-.0490	-0.0488	0.41
$A(H=0.1,h=0.2)$	- 0.0671	-0.0670	0.14
$A(H=0.2,h=0.2)$	-0.1070	-0.1056	1.31
$A(H=0.1,h=0.3)$	-0.0754	-0.0753	0.13
$A(H=0.2,h=0.3)$	-0.1261	-0.1261	0
$A(H=0.3,h=0.3)$	-0.1503	-0.1475	1.86
$A(H=0.1,h=0.4)$	-0.0792	-0.0791	0.13
$A(H=0.2,h=0.4)$	-0.1339	-0.1341	0.15
$A(H=0.3,h=0.4)$	-0.1644	-0.1643	0.06
$A(H=0.4,h=0.4)$	-0.1760	-0.1742	1.03

Stress at Edge Boundary. The physical interpretation of the strain relaxation for SEB is the same as done for the stress at hole boundary. The difference as previously explained is in the simulation approach where the hole is introduced with the EKill function to delete the elements under the hole area while the plate is under bi-axial loading at the edge boundary and the appropriate strain relaxations $A(H,h)$ in this case equal the difference of the strain responses before and after the introduction of the hole. Moreover, simulation is performed using 3D (solid186) elements, while keeping the increment sizing, plate and hole dimensions the same as in SHB method. Table 5.8 presents the verified $A(H,h)$ strain relaxations.

Table 5.8: The strain relaxations obtained through SEB compared with G.S. Schajer using Incremental hole drilling method.

Strain Relaxations	Schajer Results	SEB	
		Value	Error (%)
$A(H=0.1,h=0.1)$	-0.0490	-0.0494	0.82
$A(H=0.1,h=0.2)$	-0.0671	-0.0729	8.64
$A(H=0.2,h=0.2)$	-0.1070	-0.1000	6.54
$A(H=0.1,h=0.3)$	- 0.0754	-0.0943	25.07
$A(H=0.2,h=0.3)$	-0.1261	-0.1322	4.84
$A(H=0.3,h=0.3)$	-0.1503	-0.1409	6.25
$A(H=0.1,h=0.4)$	-0.0792	-0.1058	33.59
$A(H=0.2,h=0.4)$	-0.1339	-0.1488	11.12
$A(H=0.3,h=0.4)$	-0.1644	-0.1642	0.12
$A(H=0.4,h=0.4)$	-0.1760	-0.1675	4.83

Analyzing the results of numerical model show that the strain outputs start to deviate with increasing the hole depth h and keeping the stress depth H the same, with the highest error of 33.6% found in the stress output $A(H=0.1,h=0.4)$. This is inherently due to the fact the simulation in this case is different from the case of applying the stress at the hole boundary, since the uni-axial stresses applied is distributed differently at the inner

sides of the hole depth. Finally the strain relaxation coefficients are also checked with respect to the same paper, shown in Table /refIS, which show significant increase in the error percentage with deeper increments. Thus, careful interpretation of results should be performed with higher number of increments.

Table 5.9: The strain coefficients obtained through SEB compared with G.S. Schajer using Incremental hole drilling method.

Strain Coefficients	Schajer Results	SEB	
		Value	Error (%)
a_{11}	-0.0490	-0.0494	0.82
a_{21}	-0.0671	-0.0729	8.64
a_{22}	-0.0399	-0.0271	32.1
a_{31}	- 0.0754	-0.0943	25.07
a_{32}	-0.507	-0.1322	4.84
a_{33}	-0.0242	-0.1409	6.25
a_{41}	-0.0792	-0.1058	33.59
a_{42}	-0.0547	-0.1488	21.39
a_{43}	-0.0305	-0.1642	49.55
a_{44}	-0.0116	-0.1675	71.55

Based on the simulations performed up to this point, a decision is made for the purpose of computing the residual stresses within laminated structures with one or more orthotropic constituents. As it could be observed from the verified models that the method of applying stress at the edge boundary is suitable when using the through hole analysis approach, it provides results with high accuracy for both isotropic and orthotropic materials. In addition, it does provide acceptable agreement with the theoretical results in the case of isotropic materials using incremental hole drilling for the first couple of increments. On the other hand, using the method of applying stress at the hole boundary provides very fine agreement for isotropic materials in both analysis types of through hole and incremental hole drilling, but unfortunately there is no concrete method of relating far-field direct stresses to the distortions around a hole in an orthotropic infinite plate. Thus, SEB was chosen to be applied in the case laminated structures with orthopic nature.

5.3. Incremental Hole Drilling of Laminated Structures

Up to this point, simulations of thin and thick structures have been addressed, using both uniform and nonuniform stresses. The written code became more and more complex to simulate the strain response of laminated structures such as FML. Which are the main focus of this study due to their importance, as discussed in the first chapter, especially GLARE. The structural composition of GLARE required it to be simulated using incremental hole drilling while taking into account the orthotropic nature of the material. The flow chart in Figure (5.14), provides a better illustration of the effect of using the integral approach for three increments. Considering the previous simulation runs and their verified outcomes, it was proposed to use SEB approach and to limit the count of the increments to three increments to minimize the effect of simulation errors.

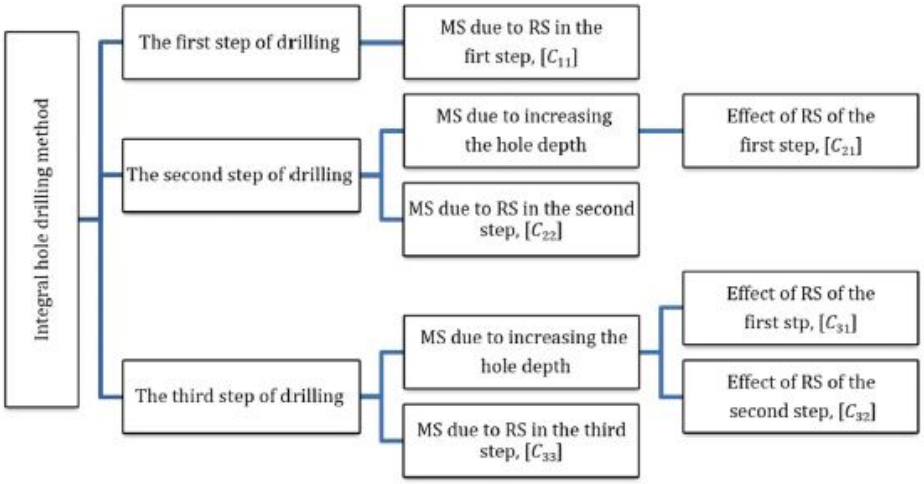

Figure 5.14: Flow chart illustrating the stain response when using the integral approach.

Based on the simulation proposal for GLARE, a code is developed in ANSYS to relate the experimentally measured strains to residual stresses within GLARE. The mechanical properties are presented in Table 5.10, with all nine elastic moduli included; this is essential to account for the bending effects resulting from the thickness of the GLARE laminate being considered finite. To simulate this, (3D) 20-node solid elements (solid186) were used to simulate each layer of the laminate separately, taking into account that each layer has its own thermo-mechanical properties.

Table 5.10: Material properties of GLARE constituents used within the numerical study.

Material	$E_1[GPa]$	$E_2 = E_3[GPa]$	$G_{12} = G_{13}[GPa]$	$G_{23}[GPa]$	$\nu_{12} = \nu_{13}$	ν_{23}	$\alpha_x(\mu/C^\circ)$	$\alpha_y(\mu/C^\circ)$
S2 Glass Fiber	52 .0	7.4	3.0	1	0.33	0.2	4.1	48.6
Aluminum	72.4	72.4	27.6	27.6	0.33	0.33	22	22

Additionally, the geometrical dimensions, fiber orientations, location and type of the strain rosettes were considered during simulation. Furthermore, uni-axial stress loads were applied to obtain the strain matrix responses as defined for the IHD method, then the three columns of equation (5.12) are obtained respectively. This is performed progressively for each increment. Computing the calibration matrices for each increment step result in a significant amount of data. However, the simulation is quite similar and repetitive as only two variable are interchanged which are; h the hole depth increment and H depth level to which the stress is applied. The coefficient matrices obtained for the first three drill steps were used in combination with the experimentally obtained strain results to obtain the final stress results which are discussed in the upcoming chapter. The same is performed for all three layups of GLARE.

$$\frac{1}{E_x \cdot E_y}\begin{bmatrix} c_{11} & c_{12} & c_{13} \\ c_{21} & c_{22} & c_{23} \\ c_{31} & c_{32} & c_{33} \end{bmatrix}\begin{bmatrix} \sigma_x \\ \tau_{xy} \\ \sigma_y \end{bmatrix} = \begin{bmatrix} \epsilon_1 \\ \epsilon_2 \\ \epsilon_3 \end{bmatrix} \tag{5.12}$$

6

Discussion

The capability of incremental hole drilling to determine the residual stresses within GLARE laminates is verified in this chapter. The verification is performed by means of theoretical calculations, in particular the Classical Laminate Theory. The residual stresses are obtained by multiplying the inverse of the calibration constant matrices (Chapter 5) times the experimentally measured strains (Chapter 4). Then, comparison of the results with respect to the theoretical CLT stresses is done, where the discussion is to validate the objective of the project; incremental hole drilling method is appropriate to determine residual stresses within the laminate with acceptable standard deviation.

6.1. Theoretical residual stress of GLARE using CLT

A MATLAB software was written to compute the stresses within each layer theoretically; taking in consideration the fiber orientations, thermal coefficients and thickness of the different layers. This is performed prior to the verification to gain insight on the stress level within the laminates. The results (Figure 6.1) are associated with layup: $[AL/0]_s$, where the magnitude of the relieved in-plane stresses σ_x and σ_y are plotted with respect to the layer profile. Figures 6.2 and 6.3 are for the layups $[AL/0/90\bar{A}L]_s$ and $[AL/0/90/0/\bar{A}L]_s$ respectively. The depth profile is incremented in steps at the midpoint of each layer since the stress is constant through each layer.

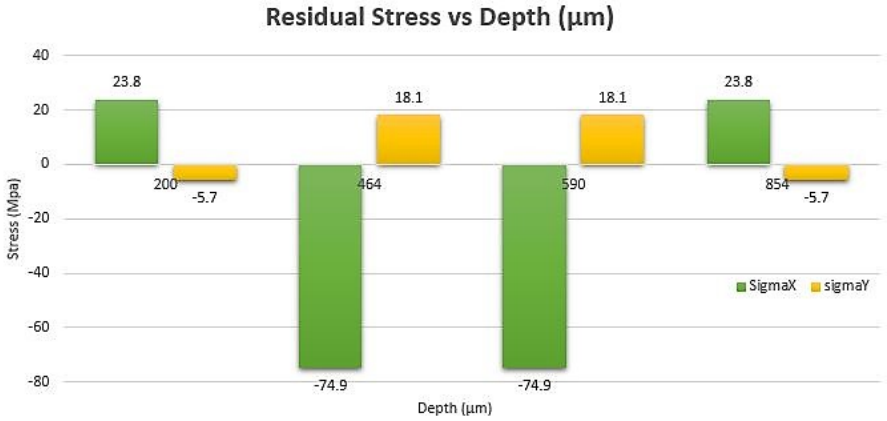

Figure 6.1: Residual stresses σ_x and σ_y plotted for GLARE layup: $[AL/0]_s$.

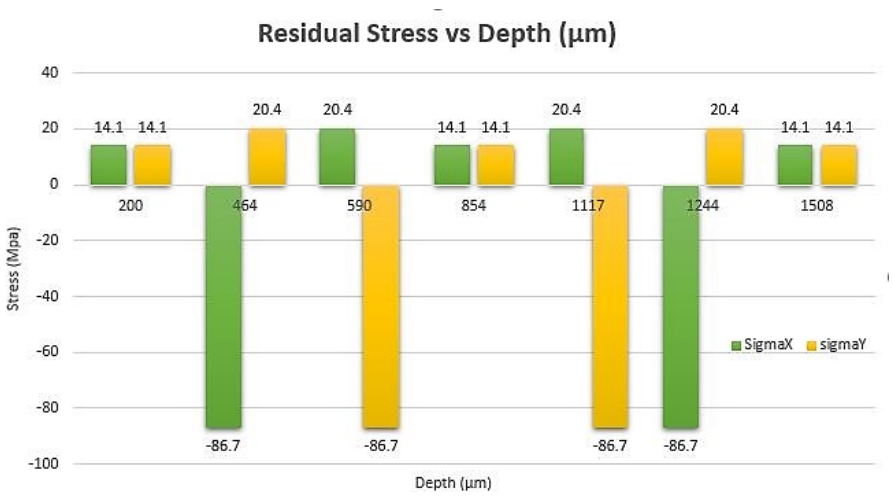

Figure 6.2: Residual stresses σ_x and σ_y plotted for GLARE layup: $[AL/0/90\bar{AL}]_s$.

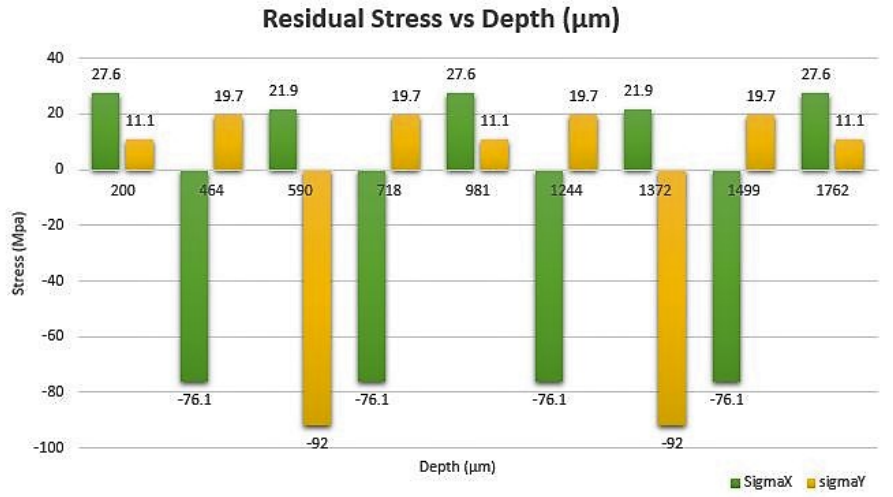

Figure 6.3: Residual stresses σ_x and σ_y plotted for GLARE layup: $[AL/0/90/0/\bar{AL}]_s$.

The theoretical analysis of the GLARE laminates using CLT show that the stress magnitude remains constant in each layer but changes between the different layers as shown in Figure 6.1. This is true because the laminates are oriented to be symmetrical which entails that the bending stresses are insignificantly small. In addition, the stresses are symmetrical with respect to the mid-plane of the laminate due to the laminate being symmetric, and balanced, which also results in the shear stresses (τ_{xy}) to be equal to zero.

6.2. Residual Stress In GLARE using IHD

Determination of the residual stresses was done as presented in equations (6.1 - 6.2) for the first two increments, the rest of the drilled increments were progressively analyzed in the same manner. It is important to note that the computations in this section are associated with the LC sizing, in addition, the computations are performed for the first three increments of the LC sizing to obtain the residual stress in first layer.

Residual stress in the first increment (depth = $16\mu\ m$):

$$\sigma_1 = \epsilon_1 [C_{11}]^{-1} \rightarrow \begin{bmatrix} \sigma_x \\ \tau_{xy} \\ \sigma_y \end{bmatrix}_1 = \begin{bmatrix} \epsilon_1 \\ \epsilon_2 \\ \epsilon_3 \end{bmatrix}_1 \begin{bmatrix} c_{11} & c_{12} & c_{13} \\ c_{21} & c_{22} & c_{23} \\ c_{31} & c_{32} & c_{33} \end{bmatrix}_{11}^{-1} \tag{6.1}$$

Residual stress in the second increment (depth = $48\mu\ m$):

$$\sigma_2 = [C_{22}]^{-1}(\epsilon_2 - [C_{21}]^{-1}\sigma_1) \rightarrow \begin{bmatrix} \sigma_x \\ \tau_{xy} \\ \sigma_y \end{bmatrix}_2 = \begin{bmatrix} c_{11} & c_{12} & c_{13} \\ c_{21} & c_{22} & c_{23} \\ c_{31} & c_{32} & c_{33} \end{bmatrix}_{22}^{-1} \left(\begin{bmatrix} \epsilon_1 \\ \epsilon_2 \\ \epsilon_3 \end{bmatrix}_2 - \begin{bmatrix} c_{11} & c_{12} & c_{13} \\ c_{21} & c_{22} & c_{23} \\ c_{31} & c_{32} & c_{33} \end{bmatrix}_{21}^{-1} \begin{bmatrix} \sigma_x \\ \tau_{xy} \\ \sigma_y \end{bmatrix}_1 \right) \tag{6.2}$$

Near surface stresses were computed using the drill steps which are mainly for the first Aluminum layer. This entails that the stress resultants of each drill increment should be around 23.8 MPa and -5.7 MPa for relieved stress in the first and third direction of the layup $[AL/0]_s$, Analogously, the same is done for the other layups. Using the proposed code within the final section of the simulation chapter for GLARE by taking into consideration the material and structure properties of the different laminates show unfortunately irregular and high percentage of errors in the final result as seen in Table 6.1 for layups $[AL/0]_s$ and $[AL/0/90/\bar{AL}]_s$. It is unfortunate that the results are not aligning with the theoretical ones which is due to a multiple reasons listed as follows:

1. The appliance of the stress load is currently performed at the edge of the plate boundary, which already was proven to be partially sound for isotropic materials. Thus, it is inherently that using the same method for fiber metal laminate which are orthotropic (anisotropic) materials would result in higher rate of deviation.

2. Incremental hole drilling in theory was built on the appliance of loads at the inner surface of the hole, which is not possible yet to be performed for orthoropic materials since there are no known equations that could relate the radial and tangential displacements around a hole in an infinite plate subjected to a far-field applied stress under plane stress conditions such as the closed form presented by Timoshenko and Goodier for isotropic material. In addition, the work presented by Lekhnitskii solution is only valid for stress at the hole boundary which is not the case for hole drilling where the strains are measured by strain gauges relatively far enough from the hole boundary.

3. The objective of the study was a bit ambitious to be performed without any previous experience or knowledge on incremental hole drilling, since this leaves a significant room of uncertainties in the experimental region.

4. Finally, the obtained results for GLARE depend on two aspects; first, the numerical model which was verified during the development process, second, the experimentally measured strain which were obtain by an outsourced (third) party due to lack of experience and equipment to perform incremental hole drilling within the department. In addition, it is not possible to verify the strain measurements obtained by the third party.

Finally, from the measurements and the study, it is concluded that the developed IHD method is still insufficient to determine residual stresses with acceptable reliability and accuracy for highly advanced materials such as fiber metal laminates.

Table 6.1: The experimental results verified with the help of (CLT) theoretical calculations for the Aluminum layer of GLARE laminates, for layups $[AL/0]_s$ and $[AL/0/90/\bar{AL}]_s$.

Stresses	Theoretical Stress Values [MPa]	Experimental Stress Values IHD [MPa]	Stress Difference Values [MPa]	Error Percentage [%]
σ_x ($[AL/0]_s$)	23.8	5.5	18.3	76.9
τ_{xy} ($[AL/0]_s$)	0	–	–	–
σ_y ($[AL/0]_s$)	-5.7	-12.1	-6.4	107.9
σ_x ($[AL/0/90/\bar{AL}]_s$)	14.1	21.3	7.2	51.1
τ_{xy} ($[AL/0/90/\bar{AL}]_s$)	0	–	–	–
σ_y ($[AL/0/90/\bar{AL}]_s$)	14.1	17.9	3.8	27.5

7

Conclusions and Recommendations

7.1. Conclusion

Stresses are present naturally in every physical object due to various reasons, yet the importance of a certain category known as residual stresses has been put in spotlight at the start of this thesis. These stresses have potential to accumulate and cause grave consequences such as accidents as observed in history and showcased in the introduction. In many cases, careful assessment of residual stresses has been bypassed and instead structures have simply been overdesigned to tackle the problem.

A more direct solution to this problem was found in monitoring a physical property related to the interior stresses while releasing those stresses by either destructive or semi destructive methods, each with its own boundaries and benefits. Hole drilling, a semi destructive method was chosen for the study. Advancements of computational systems such as Finite Element Analysis (FEA) lead to the use of hole drilling for more complex materials. Therefore, the modeling of residual stresses by means of discretizing the structure in FEM, results in the extrapolation and computational simulation of the given structural scenario. Analysis of the simulation results provides the coefficients required to relate the interior stresses to relaxed strains measured through hole drilling. While this approach might be generally applicable in the field of Mechanics of Materials, the various possible combinations of different materials, manufacturing techniques and programming of the software makes every situation different from eachother and therefore also yields a design problem for the engineer.

In this thesis, various cases were studied such as two-dimensional application on isotropic materials such as stainless steel, in addition, two dimensional simulation of orthotropic materials such as graphite epoxy plies, two dimensional mainly presents the plane stress analysis of these components. A more complex version of hole drilling is incremental hole drilling (IHD) which is performed to measure non uniform stresses within thick (three dimensional) isotropic materials as well as laminated hybrid structures such as GLARE. IHD offers high accuracy of measurements, since it is not only considering the released stresses due to removal of material in the designated hole but also takes into account the redistribution of stresses of previous drilled hole increments due to geometry change.

Subsequently, GLARE properties and dimensions were simulated into ANSYS to determine the residual stresses as described in detail in chapter three. The matrix of coefficients found using FEM is used in correlation with experimental measured strains to determine the residual stresses, which was done for a depth profile concerned with the first layer (Aluminum) of the laminates as multiple increments are drilled within the first layer to obtain the stress profile near surface. The manufactured laminates are symmetric, thus the stresses are symmetric with respect to the midplane. The experimental strains were provided by research partners using conventional hole-drilling machine and strain gauges. Finally, the accuracy and feasibility of the designed approach is verified and evaluated by means of comparison to theoretical approach, namely Classical Laminate Theory (CLT).

FEM simulated cases illustrated a fine agreement with previous related studies with a maximum error of 7% for the two (2D) dimensional applications for isotropic and orthotropic materials. In addition, incremental hole

drilling was further simulated for thick isotropic material with nonuniform stress distribution through the thickness, where the maximum error of 2% was found. However, when comparing the results obtained for GLARE laminates showed significant variation with the theoretical calculated stresses using CLT, where the error rate was irregular and highly unstable. This error was concluded to be due to multiple reasons, mainly due to the complexity of the material and the translation of far field stresses to the appropriate measured stresses in hole drilling is not applicable in the case of hybrid materials. Moreover, the strain measurements are done on the surface, while the computed stresses are associated with deep interior layers. In conclusion, this specifically designed approach for measuring and modeling residual stress has proven to be an applicable to be used for isotropic components with high accuracy and feasibility, however, it still requires more time and effort to be capable of applying incremental hole drilling for materials such as FMLs.

7.2. Recommendations

The Novelty of the IHD method in order to determine the residual stresses within GLARE at the faculty of the Aerospace Engineering, leaves significant room for progress and improvement. Therefore, some recommendations are briefly discussed by the author in this section. The lack of experience and equipment to perform IHD are the main challenges encountered, thus more practice and experimenting with the incremental hole drilling by the use of CNC or different drilling method is required.

Advancing the applicability of the method for advanced structures require dividing the physical problem into smaller segments to tackle each complex feature separately, which is inherently beneficial. The complexity arises from either the laminated structure composition or the material complex behavior. First, it is recommended to study the use of through hole analysis for laminated isotropic structures, this entails understanding the effect of having thin layers of isotropic material stacked on top of each other. The result of this analysis should present an approximate solution of the residual stress, then using incremental hole drilling with the same isotropic structure should be performed in order to obtain a more accurate stress solution. Second, it is further beneficial to study the use of hole drilling for orthotropic laminates in the same order of method complexity from an approximate solution (uniform stress) to a more accurate solution (non-uniform stress). Finally, based on these studies, the decision should be made either to perform these techniques or conclude the unfeasibility of the method for hybrid structures. However, these approaches are not possible without first gaining confidence with the practical part of the method, thus some practical suggestions are listed below:

Drill type and Equipment. Noise and irregular signal responses of the experimental strain measurements performed at the in-house workshop rendered them unusable for this study. The high instability rate of the strain results were concluded to be caused by the thermal gradients generated from drilling the laminates, although, the feed rate was quite low as much as $10\mu\ m$ per second in order not to effect the strain responses. A CNC milling machine with a concave end were used to chip away the material. Therefore, it is recommended to change the type of the drill into a smaller orbital drill which will help with the stability of the measurements. In addition, dedicating more time and effort in studying the effect of different cutter types and shapes will help with the improvement of the IHD method, In this study a solid carbide cutter was used.

Post drilling error examination of hole end and positioning of the rosette. Post IHD examinations are crucial to improve the calculated results. Since, the numerical constants that relate the measured strains to stresses; were found using a simulation built upon the assumptions of the tester. Two main assumptions with considerable effect on the final results are: the final diameter of the hole end, since, all hole drilling calculation methods assume a flat end. In addition, checking the alignment of gauge rosette with the global material directions which could alter the effective properties of the laminate in the numerical analysis. Both checks are essential after finishing the drilling process, in order to correct for any misalignment or response deviation. Furthermore, it is recommended to asses the condition of the gauges to determine the quality of drilling and bonding. This provides a tool to identify the suitability of the strain results for reliable strain measurements. The major post activities include:

1. The strain gauges are checked using a microscope for any debonding of the around the hole.

2. Careful removal of the rosette is done post drilling and the lower side of the gauge is inspected. A smooth matte surface is required to be seen, since, any markings on the bottom side of the gauge will be unfavorable for the measurement reliability.

3. The final hole depth is also measured to verify that the drilling initiated from the surface (zero depth level), which means the correct increment sizing was used.

Hole diameter and type of strain gauges. It was concluded from the research; the accuracy and reliability of the IHD method decreases with deeper stresses. Therefore, it was proposed to drill relatively larger increments for deeper stress measurements, which means more material is removed for each increment resulting in higher strain magnitudes to account for the decrease in the gauge sensitivity. The same effect is also achievable by increasing the acquired hole or strain gauge rosette diameters, which is beneficial in the case of laminates with non uniform stresses. Since, increasing the increment size is limited by the thickness of a layer which is sometimes insufficient to produce significant strain magnitudes to be measured accurately. The single drawback to this will be the amount of surface damage induced in the part.

Sensitivity tests to address the effect of unsymmetrical laminate/ different material. After establishing a reliable method to measure released strains within the faculty, it is recommended to further study the sensitivity and behavior of the IHD with respect to various layups and materials. Because the experiments done in this study were only concerned with symmetrical laminates, in order to minimize any variations or complexity generated by the eccentricities found in unsymmetrical laminates. In addition, understanding the sensitivity of the calculation method with respect to different materials and setups, requires longer period of time to be executed than the scope of this study.

Strain Monitoring. Strain monitoring was proposed during the measurement procedure but still requires extensive research. Strain Monitoring during the cure cycle showed promising preliminary results, since the strain profile was found to adhere to the temperature profile of the process feedback values, obtained by embedded thermo-couples within the autoclave. This might be beneficial for understanding the behavior of various laminates during cure.

A

Appendix - A. Theoretical Coefficients

A.1. ASTM E837-13 Isotropic Dimensionless Coefficients

TABLE 3 Numerical Values of Coefficients ā and b̄ for Uniform Stress Evaluations

Rosette A	$\bar{a}$					$\bar{b}$				
Blind Hole Depth	Hole Diameter, in. (mm)					Hole Diameter, in. (mm)				
in. (mm)	0.060 (1.52)	0.070 (1.78)	0.080 (2.03)	0.090 (2.29)	0.100 (2.54)	0.060 (1.52)	0.070 (1.78)	0.080 (2.03)	0.090 (2.29)	0.100 (2.54)
0.000 (0.0)	.000	.000	.000	.000	.000	.000	.000	.000	.000	.000
0.004 (0.1)	.008	.011	.015	.021	.026	.016	.021	.028	.037	.045
0.008 (0.2)	.019	.027	.036	.047	.059	.037	.050	.066	.084	.103
0.012 (0.3)	.032	.044	.059	.076	.097	.062	.084	.110	.137	.171
0.016 (0.4)	.045	.062	.083	.106	.136	.088	.119	.155	.193	.241
0.020 (0.5)	.057	.078	.104	.134	.170	.115	.154	.200	.248	.307
0.024 (0.6)	.068	.093	.124	.158	.199	.140	.187	.242	.299	.367
0.028 (0.7)	.078	.106	.140	.178	.222	.164	.218	.280	.345	.418
0.032 (0.8)	.082	.117	.154	.195	.241	.185	.246	.314	.385	.463
0.036 (0.9)	.093	.126	.165	.208	.256	.204	.270	.343	.419	.501
0.040 (1.0)	.098	.133	.173	.218	.267	.221	.291	.370	.449	.533
Through Hole	.088	.120	.157	.199	.244	.283	.371	.463	.554	.642

Figure A.1: ASTM numerical values of isotropic coefficients for uniform stress analysis.

A.2. Schajer G.S. Orthotropic Dimensionless Coefficients

TABLE 1—DIMENSIONLESS COMPLIANCES FOR HOLE DRILLING INTO AN ORTHOTROPIC MATERIAL

E_x/E_y	ν_{xy}	G_{xy}/E_y	c_{11}	c_{13}	c_{21}	c_{22}	c_{23}	c_{31}	c_{33}
E_y/E_x	ν_{yx}	G_{xy}/E_x	c_{33}	c_{31}	c_{23}	c_{22}	c_{21}	c_{13}	c_{11}
1	.00	.10	−.591	.169	−.291	1.180	−.291	.169	−.591
1	.25	.10	−.583	.123	−.314	1.097	−.314	.123	−.583
1	.50	.10	−.575	.076	−.336	1.013	−.336	.076	−.575
1	.75	.10	−.568	.030	−.357	.930	−.357	.030	−.568
1	.00	.20	−.514	.193	−.188	.877	−.188	.193	−.514
1	.25	.20	−.503	.146	−.205	.788	−.205	.146	−.503
1	.50	.20	−.491	.098	−.221	.699	−.221	.098	−.491
1	.75	.20	−.478	.049	−.235	.609	−.235	.049	−.478
1	.00	.30	−.474	.205	−.146	.757	−.146	.205	−.474
1	.25	.30	−.460	.157	−.160	.665	−.160	.157	−.460
1	.50	.30	−.445	.109	−.172	.572	−.172	.109	−.445
1	.00	.40	−.450	.213	−.123	.692	−.123	.213	−.450
1	.25	.40	−.433	.164	−.135	.598	−.135	.164	−.433
1	.00	.50	−.433	.218	−.108	.650	−.108	.218	−.433
2	.00	.15	−.453	.156	−.226	1.156	−.345	.185	−.743
2	.25	.15	−.448	.122	−.244	1.097	−.357	.153	−.737
2	.50	.15	−.443	.088	−.263	1.038	−.369	.122	−.730
2	.75	.15	−.438	.053	−.281	.978	−.380	.090	−.723
2	.00	.30	−.403	.180	−.144	.865	−.225	.207	−.631
2	.25	.30	−.396	.145	−.159	.802	−.233	.175	−.621
2	.50	.30	−.389	.110	−.174	.739	−.240	.143	−.611
2	.75	.30	−.382	.074	−.188	.675	−.247	.110	−.600
2	.00	.45	−.377	.193	−.111	.751	−.177	.217	−.576
2	.25	.45	−.369	.158	−.124	.686	−.182	.185	−.563
2	.50	.45	−.360	.122	−.137	.620	−.187	.152	−.550
2	.75	.45	−.350	.085	−.149	.554	−.191	.119	−.536
2	.00	.60	−.361	.201	−.092	.689	−.150	.223	−.541
2	.25	.60	−.351	.165	−.105	.623	−.154	.191	−.527
4	.00	.20	−.350	.137	−.186	1.212	−.435	.195	−.949
4	.25	.20	−.347	.112	−.201	1.171	−.441	.174	−.944
4	.50	.20	−.344	.088	−.216	1.129	−.447	.152	−.938
4	.75	.20	−.341	.063	−.232	1.087	−.453	.131	−.932
4	.00	.40	−.318	.162	−.116	.910	−.288	.215	−.787
4	.25	.40	−.314	.136	−.130	.866	−.291	.193	−.778
4	.50	.40	−.310	.110	−.143	.821	−.294	.171	−.770
4	.75	.40	−.306	.084	−.156	.776	−.296	.149	−.761
4	.00	.60	−.301	.175	−.088	.792	−.229	.223	−.707
4	.25	.60	−.296	.149	−.101	.746	−.230	.201	−.696
4	.50	.60	−.291	.122	−.112	.700	−.231	.179	−.685
4	.75	.60	−.286	.096	−.124	.653	−.231	.157	−.674
4	.00	.80	−.291	.183	−.073	.728	−.196	.228	−.659

Figure A.2: Dimensionless numerical values of orthotropic coefficients for uniform stress analysis.

B

Appendix - B. Additional Charts provided by Partners

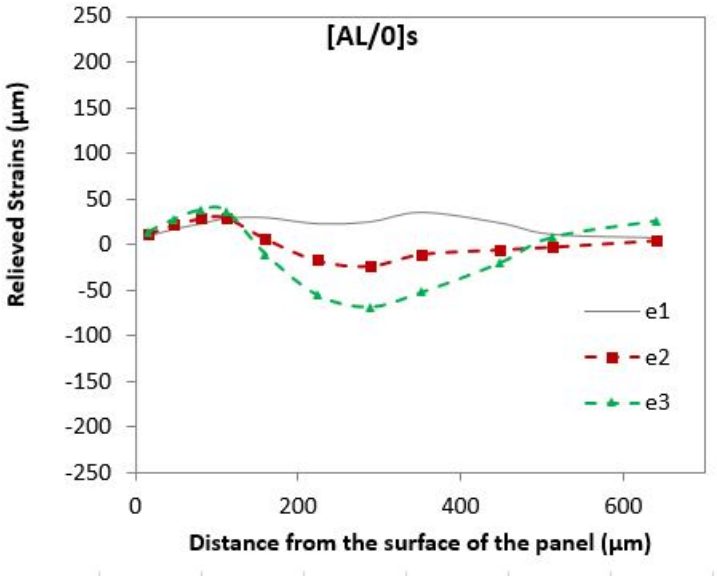

Figure B.1: Residual strains measured in the $[AL/0]_s$ layup by Coventry College.

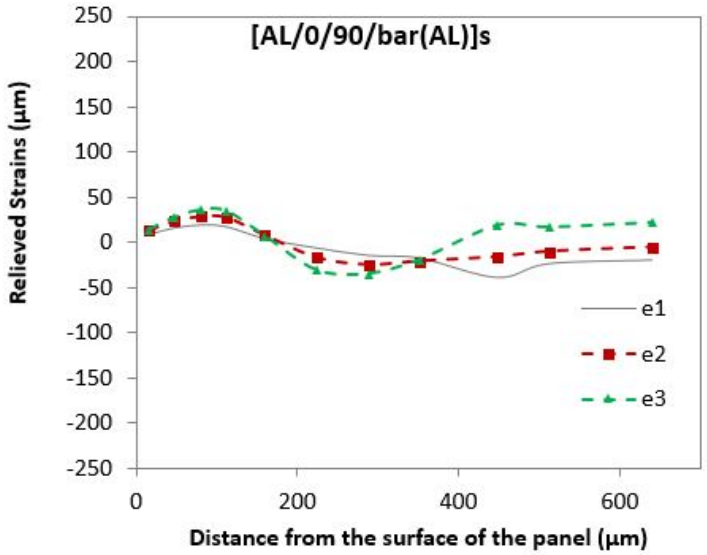

Figure B.2: Residual strains measured in the $[AL/0/90/\bar{(}AL)]_s$ layup by Coventry College.

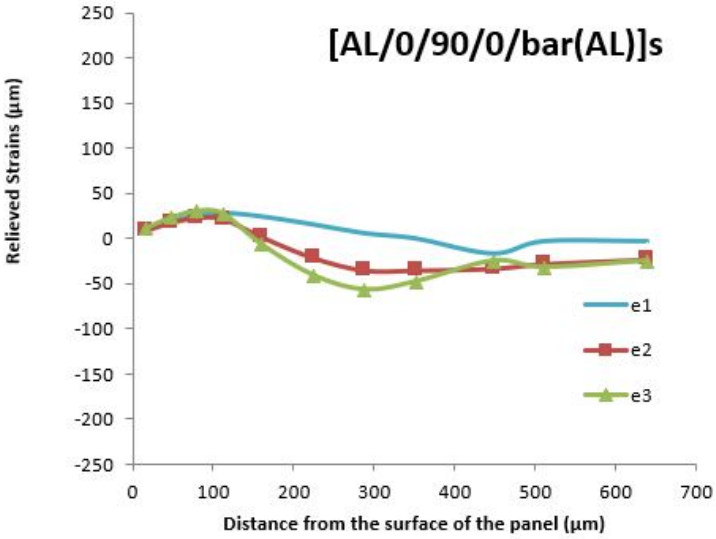

Figure B.3: Residual strains measured in the $[AL/0/90/0/\bar{(}AL)]_s$ layup by Coventry College.

C

Appendix - C. Numerical Model Inventory

Model Name	Purpose
2DSEB-Iso	**Uniform Stress Analysis**. Hole Drilling of 2D isotropic materials through applying Stress at Edge boundary.
2DSHB-Iso	**Uniform Stress Analysis**. Hole Drilling of 2D isotropic materials through applying Stress at Hole boundary.
2DSEB-Ortho	**Uniform Stress Analysis**. Hole Drilling of 2D orthotropic materials through applying Stress at Edge boundary.
3DSEB-Iso	**Uniform Stress Analysis**. Hole Drilling of 3D isotropic materials through applying Stress at Edge boundary.
3DIncreSEB-Iso	**Non-Uniform Stress Analysis**. Incremental Hole Drilling of 3D isotropic materials through applying Stress at Edge boundary.
3DIncreSHB-Iso	**Non-Uniform Stress Analysis**. Incremental Hole Drilling of 3D isotropic materials through applying Stress at Hole boundary.
3DIncre-FML	**Non-Uniform Stress Analysis**. Incremental Hole Drilling of 3D Fiber metal Laminates through applying Stress at edge boundary.

Bibliography

[1] Abouhamzeh, M. Distortions and residual stresses of glare induced by manufacturing. *Aerospace Structures and Materials.*, 2016.

[2] Abouhamzeh, M., Sinke, J., Benedictus, R., Jansen, K.M.B. Thermo-viscoelastic analysis of glare. *ELsevier LTD.*, 2016.

[3] Almen John, O., Black Paul, H. *Residual Stresses and Fatigue in Metals.* McGraw-Hill, New York, 1963.

[4] ASTM. Determining residual stresses by the hole drilling strain-gage method. standard test method e837-13. *American Society for Testing and Materials, West Conshohocken, PA*, 2008.

[5] National Transportation Safety Board. Highway accident report, collapse of u.s. 35 highway bridge. *U.S. Goverment Printing Office.*, 1967.

[6] Campbell, F.C. Manufacturing processes for advanced composites. *Elsevier Advanced Technology.*, 2004.

[7] Ghasemi, A. R., Mohammadi, M. M. Residual stress measurement of fiber metal laminates using incremental hole drilling technique in consideration of the integral method. *International Journal of Mechanical Science, 114, 246-256.*, 2016.

[8] Kassapoglou, C. Design and analysis of composite structures, with applications to aerospace structures. *Aerospace Structures and Materials.*, 2010.

[9] R.A. Kelsey. Measuring non-uniform residual stresses by the hole drilling method. *Proceedings SESA, 14.1, 181-194.*, 1956.

[10] Masubuchi, K., Blodgett, O. W., Matsui, S., Ruud, C. O., Tsai, C. C. . *Welding Handbook, Welding Science and Technology, Chapter 7.* American Welding Society, 2001.

[11] S.K. Mazumdar. *Composite Manufacturing, Materials, Product and Process Engineering.* CRC Press LLC, 2002.

[12] Mcllree, A.R., Ruud, C. O., Jacobs, M.E. . The residual stresses in stress corrosion performance of roller expanded inconel 600 stream generator tubing. *Proc. International Conference on Expanded and Rolled Joint Technology, Canadian Nuclear Society, Toronto, Canada.*, 1993.

[13] National Transportation Safety Board. Highway accident report. *U.S. Goverment Printing Office.*, 1970.

[14] National Transportation Safety Board. Aircraft accident report. *U.S. Goverment Printing Office.*, 1989.

[15] Rendler, N.J., Vigness, I. Hole drilling strain gauge method of measuring residual stresses. *Experimental Mechanics, 6.12, 577-586.*, 1966.

[16] G.S Schajer. Application of finite element calculations to residual stress measurements. *Journal of Engineering Materials and Technology*, 1981.

[17] G.S Schajer. *Practical Residual Stress Measurement Methods.* John Wiley & Sons, Ltd, 2013.

[18] G.S Schajer. Residual stress measurements in finite thickness materials by hole drilling. *Society for Experimental Mechanics*, 2014.

[19] Schajer, G.S. Measurement of non-uniform residual stresses using the hole drilling method part i & ii. *Journal of Engineering Materials and Technology.*, 1988.

[20] Schajer, G.S., Steinzig, M. Full-field calculation of hole drilling residual stresses from electronic speckle pattern interferometry data. *Society for Experimental Mechanics*, 2005.

[21] Schajer, G.S., Yang, L. Residual stress measurement in orthotropic materials using the hole drilling method. *Experimental Mechanics, 34.4, 324-333.*, 1994.

[22] Jaap Schijve. *Fatigue of Structures and Materials.* Springer Science+Business Media, B.V., 2009.

[23] Senthilmurugan, A., Arasu, K. Residual stress measurement using hole drilling method. *International Research Journal of Engineering and Technology (IRJET)*, 2016.

[24] Sinke, J. Manufacturing of glare parts and structures. *Applied Composite Materials.*, 2003.

[25] Soete, W., Vancrombrugge, R. An industrial method for the determination of residual stresses. *Proceedings SESA, 8.1, 17-28.*, 1950.

[26] Stresscraft. Hole Drilling. `http://www.stresscraft.co.uk/hole_drilling.htm`, 2018. [Online; accessed 30-June-2018].

[27] ANSYS Help System. Analysis guide and theory reference ver. 8. *SAS I, Inc.*